Advances in Hybrid Solar Cells: From Dye-Sensitised to Perovskite Solar Cells

Nakita K. Noel

Mansfield College

University of Oxford

A thesis submitted in fulfilment of the requirements for the degree of Doctor of Philosophy at the University of Oxford

July 2014

Declaration

This thesis is a result of my own work and includes nothing which is the result of collaboration except where explicitly stated in the text.

I declare that no part of this work has been submitted for a degree or any other qualification at this or any other university.

Nakita K. Noel, July 2014.

To my brother Mikhail, the inspiration for almost every useful thing I've ever done in my life

Advances in Hybrid Solar Cells: From Dye-Sensitised to Perovskite Solar Cells

Nakita K. Noel, Mansfield College, University of Oxford

Thesis submitted in fulfilment of the requirements for the degree of Doctor of Philosophy at the University of Oxford. Trinity Term, 2014

Abstract

This thesis presents a study of hybrid solar cells, specifically looking at various methods which can be employed in order to increase the power conversion efficiency of these devices. The experiments and results contained herein also present a very accurate picture of how rapidly the field of hybrid solar cells has progressed within the past three years. Chapters 1 and 2 present the background and motivation for the investigations undertaken, as well as the relevant theory underpinning solar cell operation. Chapter 2 also gives a brief review of the literature pertinent to the main types of devices investigated in this thesis; dye-sensitised solar cells, semiconductor sensitized solar cells and perovskite solar cells. Descriptions of the synthetic procedures, as well as the details of device fabrication and any measurement techniques used are outlined in Chapter 3.

The first set of experimental results is presented in Chapter 4. This chapter outlines the synthesis of mesoporous single crystals (MSCs) of anatase TiO_2 as well as an investigation of its electronic properties. Having shown that this material has superior electronic properties to the conventionally used nanoparticle films, they were then integrated into low temperature processed dye-sensitised solar cells and achieved power conversion efficiencies of > 3 %, exhibiting electron transport rates which were orders of magnitude higher than those obtained for the high temperature processed control films. Chapter 5 further investigates the use of MSCs in photovoltaic devices, this time utilising a more strongly absorbing inorganic sensitiser, Sb_2S_3. Utilising the

readily tunable pore size of MSCs, these Sb_2S_3 devices showed an increase in voltage and fill factor which can be attributed to a decrease in recombination within these devices. This chapter also presents the use of Sb_2S_3 in the meso-superstructured configuration. This device architecture showed consistently higher voltages suggesting that in this architecture, charge transport occurs through the absorber and not the mesoporous scaffold.

Chapters 6 and 7 focus on the use of hybrid organic-inorganic perovskites in photovoltaic devices. In Chapter 6 the mixed halide, lead-based perovskite, $CH_3NH_3PbI_{3-x}Cl_x$ is employed in a planar heterojunction device architecture. The effects of Lewis base passivation on this material are investigated by determining the photoluminescence (PL) lifetimes and quantum efficiencies of treated and untreated films. It is found that passivating films of this material using Lewis bases causes an increase in the PLQE at low fluences as well as increasing the PL lifetime. By globally fitting these results to a model the trap densities are extracted and it is found that using these surface treatments decreases the trap density of the perovskite films. Finally, these treatments are used in complete solar cells resulting in increased power conversion efficiencies and an improvement in the stabilised power output of the devices. Chapter 7 describes the materials synthesis and characterisation of the tin-based perovskite $CH_3NH_3SnI_3$ and presents the first operational, lead-free perovskite solar cell.

The work presented in this thesis describes significant advances in the field of hybrid solar cells, specifically with regards to improvements made to the nanostructured electrode, and the development and implementation of more highly absorbing sensitizers. The improvements discussed here will prove to be quite important in the drive towards exploiting solar power as a clean, affordable source of energy.

Acknowledgements

My deepest thanks go first to Almighty God for giving me life and strength and bringing me this far. Next to my supervisor Prof. Henry Snaith, for being amazingly supportive throughout this entire process and for always being excited about my work even at those times when I wasn't. You have given me an amazing opportunity and made science more fun than most people can imagine; I am eternally indebted to you. I will never fully be able to express how thankful I am to the members of the Snaith group both past and present. You have all made those very long and frustrating lab days into much better experiences than they would have been without you. I'll always reserve one of the most special places in my heart for a few of you that I have to mention by name; Tomas, Martina, James, Severin, Antonio, Giles and Agnese, what I would have done without you guys, Lord alone knows. If friends are the family you choose, I couldn't have chosen any better. Special thanks to Martina and Tomas for silently and steadfastly walking me through one of the hardest periods of my life and for being there no matter what…I love you guys immensely, you have no idea what your support has meant to me. To Dr. Ed Crossland and Dr. Sam Stranks (a.ka. The Stranksinator), there has never been, nor will there ever be better postdocs! Thanks for constantly shining the light on us dim PhD students, we would have died without you (Ed I am still bitter that you left us….just saying). Clare, our group would probably cease to function if it weren't for your amazing ability to organise us as well as Henry! We don't tell you how amazing you are nearly enough….thank you a gazillion times over.

Thanks wouldn't be thanks if I didn't say thanks to my little bits of Caribbean flavour that always spiced up the grey, dreary days with immense sassiness and bundles of laughs. Alecia, Yonique and Se-shauna the girls that always hold you down and chase the homesickness away with utter craziness and scandal. Love, love, looooooooove you guys.

To my family, my constant source of strength and support, you never let me feel like I was actually 4500 miles away. Mikhail, the big brother, my everlasting voice of reason, I have no idea who I would be without you (yea yea enough sap). Mom, you

still carry me even though I am grown, and Dad your never ending prayers may have worked after all. Mel and Niks, thank you for making me smile when I didn't want to. Tanya, thanks for checking up on me every day, and for knowing what was wrong when no one else did. Also for my daily pictures of the Shea-bug that warmed my heart on my most awful days. You're the best sister-in-law ever. To my friends at home: Christine, Mary, Chad, Marisha, Avynash, Tahirah, Neisha and Reignier, far apart yet always there. I love you guys, thanks for your consistent support.

Lastly, to everyone who I have had the opportunity to work with while I have been here, thank you so much for all the discussions that definitely broadened my horizons. Each one of you has shaped my experience here and who I am today. I will always be grateful. Special thanks to Dr. Amir Abbas Haghighirad who has become our group's crystallography guru. Please stop thinking of crazy materials for us to make! I'm actually kidding please don't☺. Also to Dr. Michael Johnston for giving me a couple precious weeks on the glove box evaporator that allowed me to make Sn perovskites that didn't instantly vanish, and to Prof. Laura Herz and Christian Wehrenfennig for THz measurements.

Contents

List of Figures xi

Abbreviations and Nomenclature xiii

1. Introduction

1.1 Context and Motivation 1

1.2 Objectives of the Present Thesis 5

1.3 References 8

2. Theory and Background

2.1 Metals, Insulators and Semiconductors 13

2.2 Operating Principles of Photovoltaics 19

2.2.1 Light Absorption and Charge Generation 19

2.2.2 Charge Separation 21

2.2.3 Charge Collection 23

2.3 Characterisation of Photovoltaic Devices 24

2.4 Operational Principles of Solid-State Sensitised Solar Cells 26

2.4.1 Charge Generation 29

2.4.2 Electron Transport through TiO_2 30

2.4.3 Hole Transport in the HTM 32

2.5 Alternative Sensitizers 33

2.6 Perovskite Solar Cells 36

2.7 References 39

3. Experimental Methods

3.1 Preparation of Solid-State Dye-Sensitised Solar Cells 51

3.1.1 Chemical Etching of FTO Substrates 52

3.1.2 Deposition of the TiO_2 Compact Layer 53

3.1.3 Deposition of the Mesoporous TiO_2 Layer 54

3.1.4 $TiCl_4$ Surface Treatment 56

3.1.5 Dyeing 56

3.1.6 Spin coating the HTM 57

3.1.7 Thermal Evaporation of Electrodes 58

3.2 Preparation of Sb_2S_3-Sensitized Solar Cells 58

3.2.1 Preparation of Mesoporous Alumina Scaffold 59

3.2.2 Chemical Bath Deposition of Sb_2S_3 59

3.2.3 Deposition of the HTM and Thermal Evaporation 60

3.3 Fabrication of Planar Heterojunction Perovskite Solar Cells 60

3.4 Fabrication of Lead-Free Perovskite-Sensitized Solar Cells 61

3.5 Fabrication of Spectroscopy Samples 62

3.6 Electrical Characterization 63

3.6.1 Solar Cell Characterization 63

3.6.2 Transient Photocurrent and Photovoltage Decays 63

3.7 Spectroscopy 66

3.7.1 Absorption Spectroscopy 66

3.7.2 Steady-State and Time-Resolved Photoluminescence Spectroscopy 67

3.7.3 Photoluminescence Quantum Efficiency 68

3.7.4 Photo-thermal Deflection Spectroscopy 69

3.7.5 Terahertz Time-Domain Spectroscopy 70

3.8 Scanning Electron Microscopy 70

3.9 References 71

4. Mesoporous Single Crystals: A Facile Route to Reduced Electronic Disorder and Efficient, Low Temperature Processed Dye-Sensitized Solar Cells

4.1 Broad Context 76
4.2 Introduction 77
4.3 Synthesis of MSCs 80
4.4 Electrical Characterisation 80
4.5 Device Fabrication 83
4.6 Transient Photovoltage and Photovoltage Decay Measurements 92
4.7 Summary and Outlook 96
4.8 References 97

5. Alternative Absorber Materials: Sb2S3 Sensitized Solar Cells

5.1 Broad Context 105
5.2 Introduction 106
5.3 Device Fabrication 109
5.4 Summary and Outlook 114
5.5 References 115

6. Enhanced Photoluminescence and Device Performance via Lewis Base Passivation in Organic-Inorganic Lead Halide Perovskite Solar Cells

6.1 Broad Context 121
6.2 Introduction 123
6.3 Photoluminescence Measurements 125
6.4 Device Performance 132
6.5 Summary and Outlook 135
6.6 References 136

7. Lead-Free Organic-Inorganic Tin Halide Perovskites for Photovoltaic Applications

7.1 Broad Context 144
7.2 Introduction 146
7.3 X-Ray Diffraction Measurements 147
7.4 Optical Characterisation 150
7.5 Terahertz Spectroscopy 153
7.6 Scanning Electron Microscopy 161
7.7 Device Performance 164
7.8 Summary and Outlook 170
7.9 References 171

8. Conclusions and Outlook

8.1 Salient Points of the Thesis 177
8.2 References 182

Appendix I: Hexahalogenated Stannates 185

Appendix II: Publications and Conferences 191

List of Figures

1.1 2011 Global Energy Supply by Power Source
1.2 Trends of Global Energy Consumption 2005-2015

2.1 Energy Band Diagrams of Metals, Insulators and Semiconductors
2.2 Dispersion relation of the Free Electron Model
2.3 Origin of the Band Gap- Nearly Free Electron Model
2.4 P-type and N-type Doping in Silicon
2.5 Solar Spectrum
2.6 Band Bending at a p-n Junction
2.7 Current-Voltage Characteristics of a Photovoltaic Cell
2.8 Operation Processes in the ssDSSC
2.9 Chemical Structure of spiro-OMeTAD

3.1 Electrode Pattern
3.2 Chemical Structure of D102
3.3 Transient Decay Curves
3.4 Time Resolved PL Setup

4.1 Nucleation and Growth of MSCs
4.2 SEM Images and TMS Measurement of MSCs
4.3 Top-view SEM Images of MSC films
4.4 Cross-sectional SEMs of MSC Devices
4.5 SEM Images of MSC “nuggets” and ss-DSSC
4.6 Transmission of Dyed Films and Film Photographs
4.7 Current-Voltage Characteristics and Performance Parameters

4.8 Absorbance of Dyed Films
4.9 Transport and Recombination Characteristics

5.1 Absorption Characteristics of Sb_2S_3 films
5.2 Current-Voltage Characteristics and Performance Parameters
5.3 Schematic of Electron Transport Mechanism in Sb_2S_3 Devices

6.1 Illustration of Trap Sites and Passivation Mechanism
6.2 Chemical Structure of Passivating Agents
6.3 Photoluminescence Decays
6.4 Photoluminescence Decays and Quantum Efficiencies
6.5 Model Fits to Photoluminescence Decays
6.6 Current-Voltage Characteristics and Stabilised Maximum Power Output

7.1 XRD Pattern and Crystal Structure of $CH_3NH_3SnI_3$
7.2 XRD Pattern of Degraded $CH_3NH_3SnI_3$ film
7.3 Absorption, Emission and PDS Spectra of $CH_3NH_3SnI_3$
7.4 Transient Terahertz Conductivity and L_D modelling of $CH_3NH_3SnI_3$
7.5 Top-view and Cross-sectional SEM Images of $CH_3NH_3SnI_3$ Films and Solar Cell
7.6 Cross-sectional SEM Image of a TiO_2-based $CH_3NH_3SnI_3$ device
7.7 Top-view SEM Images of $CH_3NH_3SnI_3$ Films
7.8 Current-Voltage Characteristics and Performance Parameters
7.9 Light and Dark Current-Voltage Characteristics
7.10 Current-Voltage Characteristics of Cells of Varying Performance
7.11 Photographs of Properly Sealed and Degraded $CH_3NH_3SnI_3$ Films

Abbreviations and Nomenclature

Abbreviations

AM 1.5	Air Mass 1.5
ALD	Atomic Layer Deposition
BIPV	Building Integrated photovoltaics
CB	Conduction Band
CBD	Chemical Bath Deposition
CIGS	Copper Indium Gallium Selenide
CZTS	Copper Zinc Tin Sulphide
DI	Deionised
DOS	Density of States
DSSC	Dye-sensitised Solar Cell
EPR	Electron Paramagnetic Resonance
ETA	Extremely thin absorber
F.F.	Fill Factor
FTO	Fluorine-doped Tin Oxide
HOMO	Highest Occupied Molecular Orbital
HTM	Hole transport material
IPFB	Iodopentafluorobenzene
J_{SC}	Short Circuit Current Density
Li-TFSI	bis(trifluoromethylsulfonyl)amine lithium
LTNP	Low Temperature Processed Nanoparticles

LUMO	Lowest Unoccupied Molecular Orbital
MAI	Methylammonium iodide
MSC	Mesoporous Single Crystal
MSSC	Meso-superstructured Solar Cell
MT	Multiple Trapping
NP	Nanoparticle
P_{MAX}	Maximum Power Point
P3HT	Poly (3-hexylthiophene)
PCBM	Phenyl- C61- butyric acid methyl ester
PCE	Power Conversion Efficiency
PCPDTBT	Poly[2,6-(4,4-bis-(2-ethylhexyl)-4*H*-cyclopenta [2,1-*b*;3,4-*b*′]dithiophene)-*alt*-4,7(2,1,3-benzothiadiazole)]
PDS	Photothermal Deflection Spectroscopy
PL	Photoluminescence
PLQE	Photoluminescence quantum efficiency
PMMA	Poly methyl methacrylate
PMT	Photomultiplier Tube
PTAA	Polytriaryl amine
QDSC	Quantum dot sensitised solar cell
SEM	Scanning electron microscope
SILAR	Successive ionic layer adsorption and reaction
ss-DSSC	Solid-state dye Sensitised solar cell
SSSC	Semiconductor sensitised solar cell
SSC	Sensitised solar cell
*t*BP	*tert*-butyl pyridine

TCSPC	Time-correlated single photon counting
TMS	Transient Mobility Spectroscopy
V_{OC}	Open circuit voltage
VB	Valence band

Nomenclature

α	Absorption coefficient, parameter describing the distribution of sub-band gap states
γ	Electron hole recombination rate constant
γp_0	Monomolecular decay rate constant
ΔQ	Generated charge
ΔS	Sheet conductivity
ΔT	Photoinduced change in THz electric field
ΔV	Voltage perturbation
ε	Molar extinction coefficient
η	Power conversion efficiency
η_c	Collection efficiency
φ	Photon-charge branching ratio
$\varphi\gamma$	Bimolecular recombination rate constant
$\varphi^{-1}p_0$	Hole doping density
μ	Mobility
τ_{rec}	Electron recombination lifetime
τ_{meas}	Measured transport lifetime
τ_{trans}	Electron transport lifetime

ψ	Solution to eigenstates
A_{eff}	Overlap area between optical pump and THz pulse
C	Capacitance
D	Diffusion constant
e	Elementary Charge
E_g	Band gap energy
E_c	Conduction band energy
E_{Fn}	Quasi- Fermi level of electrons
g (E_{Fn})	Density of states
h	Planck's constant
I	Transmitted light intensity
I_0	Incident light intensity
J_{MPP}	Stabilised current density
J_s	Reverse saturation current
k_B	Boltzmann's constant
L(n)	Charge diffusion length
n	Concentration of Photogenerated electrons
N_L	Number of states below conduction band
N_T	Trap density
N	Number of photoexcited charge carriers
p	Concentration of photogenerated holes
p_0	Doped hole density
p(0)	Initial photoexcited hole density
P_i	Incident power
q	charge

$R(n)$	Total carrier recombination rate
R_{pump}	Reflectivity of sample in THz excitation beam
T_{pump}	Light transmitted through sample
V_A	Voltage across diode at forward bias

Chapter 1

Introduction

1.1 Context and Motivation

The rapid increase in industrialisation coupled with an ever-growing population has resulted in the exponential growth of the world's energy demands. At present, fossil fuels are the cheapest, most exploited sources of energy. However, this has come with some difficulties, the first being that our supply of fossil fuels is dwindling, and the second being the negative environmental impact caused by the combustion of fossil fuels. Even if new deposits of fossil fuels were to be uncovered, the increase in anthropogenic greenhouse emissions have led to significant global warming, and rising sea levels from 1950 to the present day.[1] If we were to sustain our current rate of fossil fuel consumption, the environmental consequences would be dire. As such, there has been a concerted effort to find abundant clean, renewable, energy resources which can both support our industrial growth and decrease, even halt, our greenhouse emissions.

The most probable sources of renewable energy are wind, hydropower, geothermal energy, biofuels and solar power. The 2011 statistics on global energy consumption are summarised in **Figure 1.1**.[2] Of these potential alternative to fossil fuels, solar energy is one of the most abundant, promising sources of clean energy with low environmental impact. However, as it stands, renewable energy sources are grossly underused, accounting for only

4.7 % of the total global power supply.

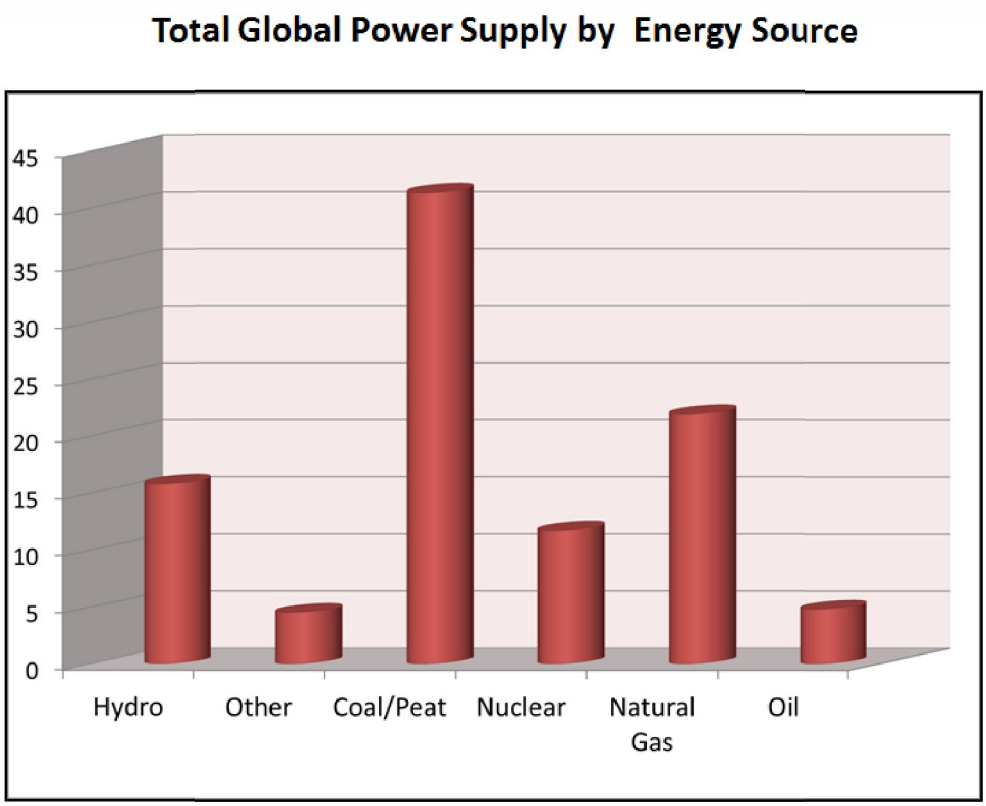

Figure 1.1: Bar graph of 2011 global power supply by energy source. Other sources include solar, wind and geothermal power.

One of the major problems with the implementation of renewable energy is the cost of the required materials and/or infrastructure. With respect to solar power, the industry is currently dominated by photovoltaics made of crystalline silicon or gallium arsenide (GaAs), reaching remarkable power conversion efficiencies of over 28 %.[3] One of the main disadvantages of devices such as these is the necessity of high quality, relatively defect-free

films of the semiconductor materials. This requirement greatly increases manufacturing costs and is the major culprit behind the high cost of such devices. While the price of silicon-based photovoltaics has decreased dramatically over the last 10 years, due to advancements in processing and the ability to use thinner wafers, the production and installation costs are still quite high, resulting in longer energy and financial payback times, thus decreasing the economic feasibility of use.[4]

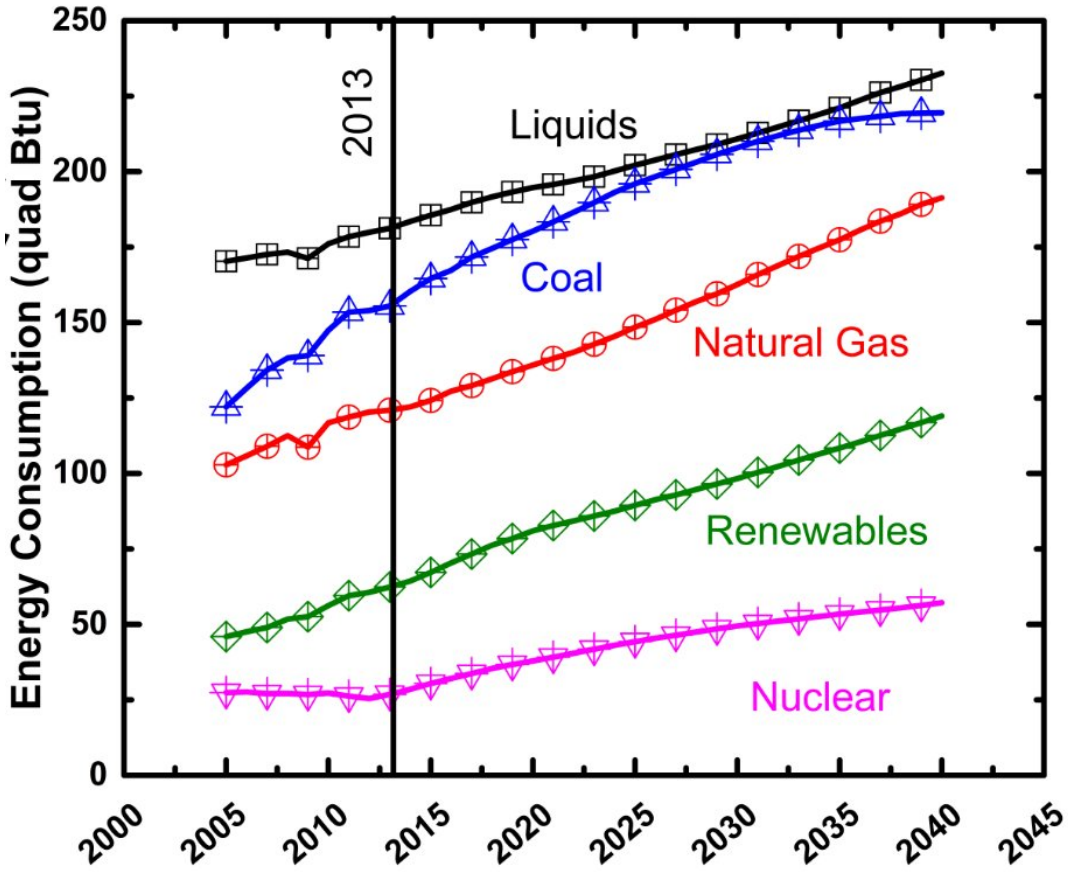

Figure 1.2: Trends of global energy consumption from 2005-2013, and projected usage up to 2040. Data obtained from the US Energy Information Administration (EIA).[5]

Figure 1.2 shows the trend in global energy consumption from 2005 to 2013, along with the projected trends up to 2040. While the usage of renewable energy is projected to continue to increase, it is still not expected to be comparable to the use of fossil fuels. In order for the use of renewable energy technologies to become compatible with that of fossil fuels, the cost must be considerably reduced. Over the last decade, a tremendous amount of research has been done on developing new, cheaper solar cell architectures. In particular, third generation solar cell concepts involving the use of solution processable semiconductor materials have been widely researched. Photovoltaic devices incorporating solution processable materials have the advantage of being comprised of easily accessible, cheap and tunable materials, in addition to being compatible with facile, low cost, large scale, production methods such as reel-to-reel printing. This reduction in the cost of the starting materials, in addition to the simplification of the manufacturing process, is a major step towards making solar energy more widely accessible, as this drastically reduces the energy and financial payback times, which is the major hindrance to widespread use of conventional inorganic semiconductor based photovoltaics.

One of the emerging solar cell concepts which has been widely investigated is the dye-sensitised solar cell (DSSC). Unlike conventional semiconductor based photovoltaics, in the DSSC, the fundamental processes involved in conversion of solar to electrical energy are carried out in different components of the device. The current embodiment of this device was first reported by O'Regan and Gratzel in 1991.[6] This pivotal work introduced the concept of using mesoporous TiO_2 as the n-type collection layer, thus increasing the surface area for dye adsorption and resulting in greatly improved device performance as compared to previous devices based on flat films. While devices based on this architecture have now reached efficiencies of over 12%,[7,8] the corrosive nature of the liquid electrolyte has cast a shadow of doubt on the long-term stability of such devices. In an effort to rectify

this problem, a solid-state hole transporting material 2,2,2′,7,7′-tetrakis(N,N′-di-p-methoxyphenylamine)-9,9′-spirobifluorene (spiro-OMeTAD), was employed.[9] This gave rise to the second incarnation of the DSSC, referred to as the solid-state dye sensitised solar cell (ssDSSC). This embodiment of the DSSC opened pathways to utilising various absorber materials which would otherwise be unstable in the presence of the corrosive liquid electrolyte. One such class of materials is the hybrid organic-inorganic metal halide perovskites which have recently taken the research community by storm, rapidly surpassing the efficiencies of conventional sensitised solar cells to achieve remarkable power conversion efficiencies of up to 17.9 % under simulated full sunlight.[10]

1.2 Objectives of the Present Thesis

While the ssDSSC is more attractive than the liquid electrolyte DSSC with respect to potential long-term stability, the performance of these devices has consistently fallen short of their maximum potential.[11] One of the primary reasons for this is the inability to fabricate ssDSSCs such that they are thick enough to absorb a significant portion of the incident light.[12,13] In a liquid electrolyte DSSC, the typical thickness of the mesoporous TiO_2 electrode is $\geq$ 10 μm, whereas in a ssDSSC, the typical thickness is between 2 μm - 3μm, thus decreasing the surface area available for dye adsorption, and consequently, less current is produced from these devices. The operating principles of the ssDSSC are discussed in Chapter 2.

Many attempts at increasing the efficiency of ssDSSCs have been made, and many reasons suggested for their inability to hit efficiency targets. One area which has been exhaustively studied is improving the architecture of the TiO_2 electrode. The random nanoparticle network formed by sintering the TiO_2 layer suffers from poor charge transport properties and a high density of sub-band gap states, which results in a high level of electronic disorder in the TiO_2. This high level of electronic disorder then reduces the maximum attainable open circuit voltage under illumination at any given light intensity. The electron mobility of anatase TiO_2 has been shown to decrease by several orders of magnitude from single crystal domains ($\mu = 10\ cm^2\ V^{-1}\ s^{-1}$) to nanoparticle films ($\mu = 10^{-1}\text{-}10^{-5}\ cm^2\ V^{-1}\ s^{-1}$), as a result of increased disorder in nanoparticle films. Attempts to increase the rate of charge transport in the TiO_2 electrode resulted in the use of single crystalline nanowires as opposed to nanoparticles however; there was little improvement in the power conversion efficiency of these devices as a result of a decrease in surface area, and consequently, a decrease in the dye loading.

It follows then that if one could combine the high surface area of a nanoparticle film, with the faster charge transport of single crystals, an increase in the power conversion efficiency should ensue. This forms the basis for the first practical investigation in this thesis. Chapter 4 presents the development of mesoporous single crystals of anatase TiO_2, a structure which combines fast charge transport and high surface area, resulting in improved performance of conventional ssDSSCs. I also show that the superior electronic properties of this form of TiO_2 negates the need for sintering the TiO_2 film resulting in a facile route to completely low temperature processed ssDSSCs which rival the performance of high-temperature sintered devices.

Another plausible route to overcoming the thickness limitations of the ssDSSC is to use a more highly absorbing sensitizer. Chapters 5, 6 and 7 explore the use of solution processable inorganic and hybrid organic-inorganic semiconductor materials in photovoltaics. When dye is used as a sensitizer, the performance of the photovoltaic device is optimal when a monolayer of dye is adsorbed onto a high surface area metal oxide electrode. While a thicker device would increase the surface area for adsorption, if a more strongly absorbing sensitizer with a higher molar extinction coefficient were to be used, the need for a thicker mesoporous layer would be eliminated. To this end, many inorganic absorber materials have been investigated as replacements for dyes in what is known as the semiconductor sensitized solar cell (SSSC). Of this class of materials, PbS and Sb_2S_3 are quite promising.[14-16] An investigation into the performance of Sb_2S_3 in SSSCs with various mesoporous electrodes forms the basis of Chapter 5.

Recently, a family of hybrid organic-inorganic lead halide perovskite materials have taken the photovoltaic research community by storm. These materials have been used as highly absorbing sensitizers in traditional TiO_2 based SSSCs,[17] as well as a combination of sensitizer and charge transport material in meso-superstructured solar cells (MSSCs)[18-20] and planar-heterojunction devices.[21-25] While the properties of these materials are relatively underexplored, recent modelling studies have suggested the presence of trap states in the material.[26] It has been postulated that one major source of these trap states is the presence of undercoordinated Pb atoms within the crystal structure. Chapter 6 presents a study on the passivation of trap states within the mixed halide perovskite material $CH_3NH_3PbI_{3-x}Cl_x$. In Chapter 7, I introduce a Pb-free perovskite absorber $CH_3NH_3SnI_3$ and its use in SSSCs, demonstrating its potential to achieve or even surpass the power conversion efficiencies of its Pb-based counterpart. Unfortunately, the instability of this material under ambient conditions may prove to be a barrier to commercialisation. While attempts to stabilise it

have been made, they have been largely unsuccessful and as such, this is an area of ongoing research.

This thesis therefore, represents advancements made in the field of solid state hybrid solar cells, specifically with regards to the development and implementation of new materials, as well as improvements on existing knowledge.

1.3 References

[1] Stocker, T. F. et al. Climate Change 2013. The Physical Science Basis. Working Group I Contribution to the Fifth Assessment Report of the Intergovernmental Panel on Climate Change-Abstract for decision-makers. (Groupe d'experts intergouvernemental sur l'evolution du climat/Intergovernmental Panel on Climate Change-IPCC, C/O World Meteorological Organization, 7bis Avenue de la Paix, CP 2300 CH-1211 Geneva 2 (Switzerland), 2013).

[2] Agency, I. E. Key World Energy Statistics. 1-82 (2013).

[3] Contreras, M. A. et al. SHORT COMMUNICATION: ACCELERATED PUBLICATION: Diode characteristics in state-of-the-art ZnO/CdS/Cu(In1−xGax)Se2 solar cells. Progress in Photovoltaics: Research and Applications 13, 209-216, doi:10.1002/pip.626 (2005).

[4] Chu, S. & Majumdar, A. Opportunities and challenges for a sustainable energy future. Nature 488, 294-303 (2012).

[5] Administration, U. S. E. I. Annual Energy Outlook 2014 Early Release Overview. (2013).

[6] O'Regan, B. & Gratzel, M. A low-cost, high-efficiency solar cell based on dye-sensitized colloidal TiO2 films. Nature 353, 737-740 (1991).

[7] Mathew, S. et al. Dye-sensitized solar cells with 13% efficiency achieved through the molecular engineering of porphyrin sensitizers. Nature chemistry (2014).

[8] Yella, A. et al. Porphyrin-Sensitized Solar Cells with Cobalt (II/III)–Based Redox Electrolyte Exceed 12 Percent Efficiency. Science 334, 629-634, doi:10.1126/science.1209688 (2011).

[9] Bach, U. et al. Solid-state dye-sensitized mesoporous TiO2 solar cells with high photon-to-electron conversion efficiencies. Nature 395, 583-585 (1998).

[10] (NREL), N. R. E. L. NREL, www.nrel.gov/ncpv/images/efficiency_chart.jpg (2014).

[11] Snaith, H. J., Petrozza, A., Ito, S., Miura, H. & Grätzel, M. Charge Generation and Photovoltaic Operation of Solid-State Dye-Sensitized Solar Cells Incorporating a High Extinction Coefficient Indolene-Based Sensitizer. Advanced Functional Materials 19, 1810-1818, doi:10.1002/adfm.200801751 (2009).

[12] Docampo, P. et al. Lessons Learned: From Dye-Sensitized Solar Cells to All-Solid-State Hybrid Devices. Advanced Materials 26, 4013–4030, doi:10.1002/adma.201400486 (2014).

[13] Snaith, H. J. & Schmidt-Mende, L. Advances in Liquid-Electrolyte and Solid-State Dye-Sensitized Solar Cells. Advanced Materials 19, 3187-3200, doi:10.1002/adma.200602903 (2007).

[14] Ip, A. H. et al. Hybrid passivated colloidal quantum dot solids. Nat Nano 7, 577-582,doi:http://www.nature.com/nnano/journal/v7/n9/abs/nnano.2012.127.html#supplementary-information (2012).

[15] Chang, J. A. et al. Panchromatic Photon-Harvesting by Hole-Conducting Materials in Inorganic–Organic Heterojunction Sensitized-Solar Cell through the Formation of Nanostructured Electron Channels. Nano Letters 12, 1863-1867, doi:10.1021/nl204224v (2012).

[16] Chang, J. A. et al. High-Performance Nanostructured Inorganic−Organic Heterojunction Solar Cells. Nano Letters 10, 2609-2612, doi:10.1021/nl101322h (2010).

[17] Kim, H.-S. et al. Lead Iodide Perovskite Sensitized All-Solid-State Submicron Thin Film Mesoscopic Solar Cell with Efficiency Exceeding 9%. Sci. Rep. 2, doi:http://www.nature.com/srep/2012/120821/srep00591/abs/srep00591.html#supplementary-information (2012).

[18] Lee, M. M., Teuscher, J., Miyasaka, T., Murakami, T. N. & Snaith, H. J. Efficient Hybrid Solar Cells Based on Meso-Superstructured Organometal Halide Perovskites. Science 338, 643-647, doi:10.1126/science.1228604 (2012).

[19] Ball, J. M., Lee, M. M., Hey, A. & Snaith, H. Low-Temperature Processed Mesosuperstructured to Thin-Film Perovskite Solar Cells. Energy & Environmental Science (2013).

[20] Bi, D. et al. Using two-step deposition technique to prepare perovskite (CH3NH3PbI3) for thin film solar cells based on ZrO2 and TiO2 mesostructures. RSC Advances, doi:10.1039/C3RA43228A (2013).

[21] Liu, M., Johnston, M. B. & Snaith, H. J. Efficient planar heterojunction perovskite solar cells by vapour deposition. Nature 501, 395-398, doi:10.1038/nature12509 (2013).

[22] Liu, D. & Kelly, T. L. Perovskite solar cells with a planar heterojunction structure prepared using room-temperature solution processing techniques. Nat Photon 8, 133-138, doi:10.1038/nphoton.2013.342.

http://www.nature.com/nphoton/journal/v8/n2/abs/nphoton.2013.342.html#supplementary-information (2014).

[23] Eperon, G. E., Burlakov, V. M., Docampo, P., Goriely, A. & Snaith, H. J. Morphological Control for High Performance, Solution-Processed Planar Heterojunction Perovskite Solar Cells. Advanced Functional Materials 24, 151-157, doi:10.1002/adfm.201302090 (2014).

[24] Eperon, G. E. et al. Formamidinium lead trihalide: a broadly tunable perovskite for efficient planar heterojunction solar cells. Energy & Environmental Science 7, 982-988, doi:10.1039/C3EE43822H (2014).

[25] Stranks, S. D. et al. Electron-Hole Diffusion Lengths Exceeding 1 Micrometer in an Organometal Trihalide Perovskite Absorber. Science 342, 341-344, doi:10.1126/science.1243982 (2013).

[26] Kim, J., Lee, S.-H., Lee, J. H. & Hong, K.-H. The Role of Intrinsic Defects in Methylammonium Lead Iodide Perovskite. The Journal of Physical Chemistry Letters 5, 1312-1317, doi:10.1021/jz500370k (2014).

Chapter 2

Theory and Background*

*This chapter provides the basic building blocks related to semiconductor and device physics. For a more in depth description please refer to: Hook et al.,[1] Rosenberg et al.,[2] Nelson et al.,[3] and Würfel et al.[4]

2.1 Metals, Insulators and Semiconductors

Materials and compounds can generally be placed into one of three major categories: metals, insulators or semiconductors. While there are more complicated classes and sub-classes, such as semi-metals, I will limit the discussion to these general three. These classes of materials have very different properties which can be explained by their energy band structures depicted in Figure 2.1. Both insulators and semiconductors possess a band gap, E_g, which is given as the difference in energy between the filled valence and empty conduction bands of the material. In both cases, the Fermi level, denoted E_F, lies in the centre of the band gap. The Fermi level can be defined as the chemical potential of electrons at temperatures of absolute zero. The salient difference between insulators and semiconductors is the relative size of the band gap. Insulators are classed as materials which have large band gaps (generally > 3 eV), whereas in a semiconductor the band gap is relatively small (0.5 eV – 3 eV), such that electrons can be thermally excited across E_g and into the conduction band. [1,2]

Contrastingly, metals do not possess a band gap. Here, there is an overlap of the valence and conduction bands such that the Fermi level is found in the centre of an avalanche of electronic states. Whereas in the case of a semiconductor an electron from the filled valence band can be thermally excited into the conduction band, in a metal electrons are free to move throughout the valence and conduction bands without the application of a thermal stimulus.

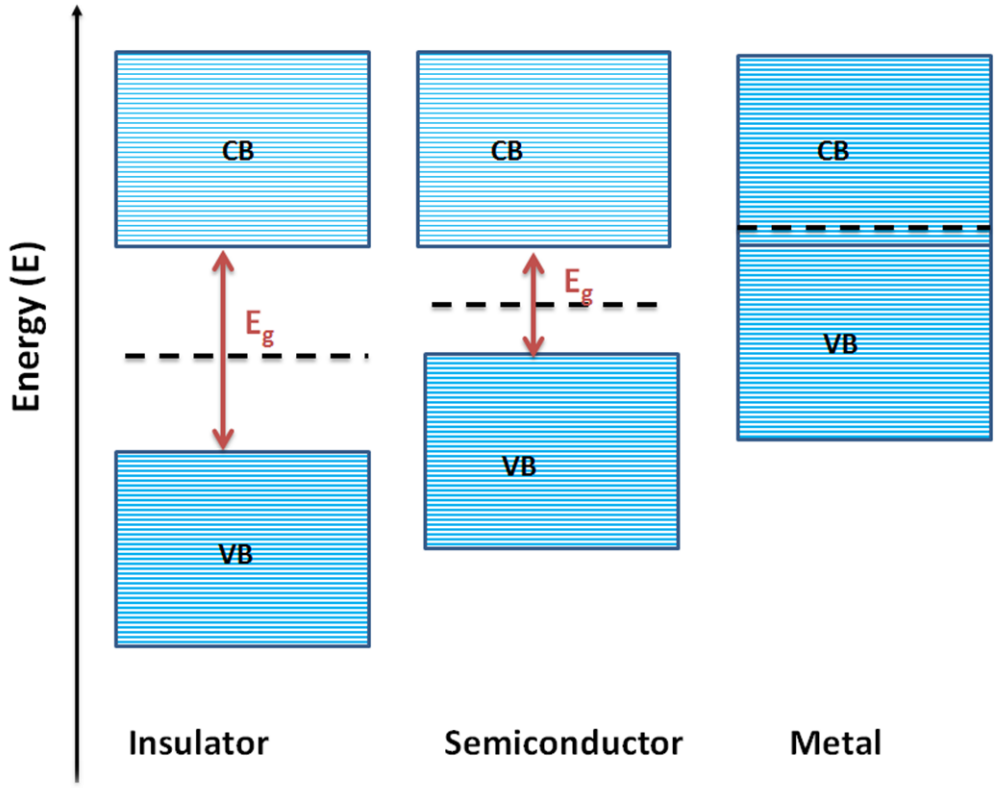

Figure 2.1: Energy band diagrams of insulators, semiconductors and metals. The Fermi level (E_F) is depicted by the black dashed lines, while the energy difference between the valence band (VB) and the conduction band (CB) or the band gap (E_g), is denoted with a red arrow. Filled states are depicted with darker blue shading, while empty states are illustrated with lighter blue shading.

When considering the origin of the band gap it is helpful to start from the Free Electron Model. In this particular case it is assumed that the electrons neither interact with each other, nor do they interact with the crystal lattice. The energy, E, of such an electron can then be described by **Equation 2.1**

$$E\,(k) = \frac{\hbar^2 k^2}{2m} \tag{2.1}$$

where k is the wavevector. The dispersion relation for such a system can then be depicted graphically as shown below in **Figure 2.2**, wherein the electron can have any value of k.

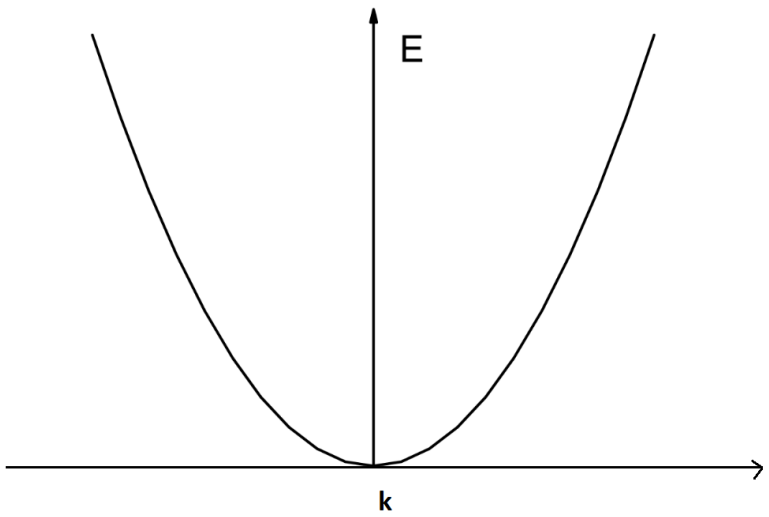

Figure 2.2: Dispersion relation of the free electron model, where a particle can have any wavevector, k.

Now in the case of the electron moving within a periodic crystal such that the lattice constant is a, the electron is no longer considered to be "free", but interacts with other electrons as well as the crystal lattice. This gives rise to the Nearly Free Electron Model which takes into consideration these interactions. In this case, boundary conditions must be imposed on the Brillouin zone. These conditions are defined in **Equation 2.2**. For simplicity, the 1D case is considered.

$$k' = k = \pm\frac{\pi}{a} \tag{2.2}$$

The respective wavefunctions can then be described by the following equations:

$$|k\rangle = e^{ikx} = e^{ix\pi/a} \tag{2.3}$$

$$|k'\rangle = e^{-ik'x} = e^{-ix\pi/a} \tag{2.4}$$

These travelling waves can then interact and will yield standing wave solutions for 2 possible eigenstates ψ_+ and ψ_-. These solutions are presented in **Equations 2.5** and **2.6**.

$$\psi_+ = |k\rangle + |k'\rangle = e^{ikx} + e^{-ik'x} = 2\cos(\pi x/a) \tag{2.5}$$

$$\psi_- = |k\rangle - |k'\rangle = e^{ikx} - e^{-ik'x} = 2\,\mathrm{i}\sin(\pi x/a) \tag{2.6}$$

As such, for any given k value, there are 2 allowed energy bands; one of a higher energy, which is known as the conduction band (CB) and one which possesses a lower energy, which is referred to as the valence band (VB). The energy band which exists between the VB and CB is a forbidden region, and is known as the band gap, E_g, of the material. This is illustrated in **Figure 2.3**.

As mentioned before, the main difference between semiconductors and insulators is then just the relative size of the energy gap. At low temperature, or in the absence of any external stimulus, an intrinsic semiconductor behaves exactly like an insulator. However, when a stimulus such as heat, light, or an electric field is applied, it provides enough energy to excite the electron from the valence band, across the band gap, to the conduction band. The presence of electrons in the conduction band results in an equal number of positive charges in the valence band. These positive charges are referred to as holes. If selective contacts are then placed on the material, such that electrons and holes are collected at opposite ends, this results in the generation of current.

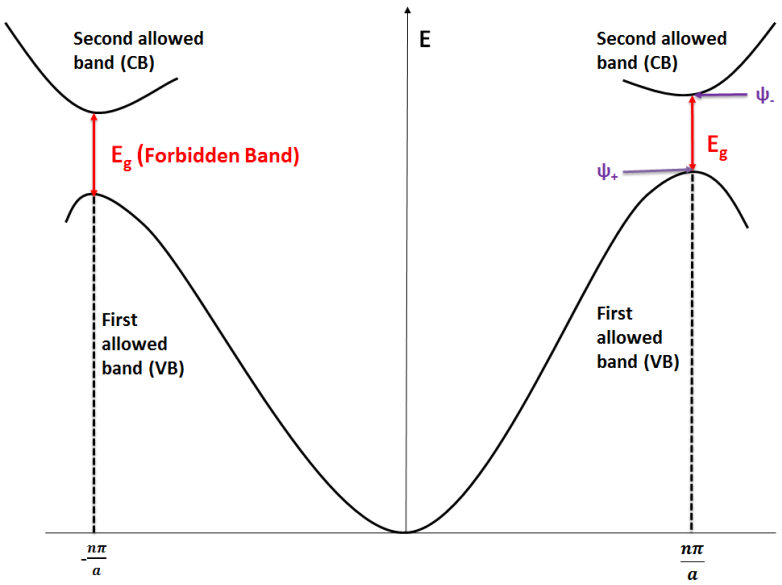

Figure 2.3: Origin of the band gap depicted using the nearly free electron model, imposing boundary conditions on the Brillouin zone. For simplicity, the 1D case is considered.

Semiconducting materials are found at the crux of electronic and optoelectronic devices, and form the basis of photovoltaic operation. As one would imagine, intrinsic, or pure semiconductors are not particularly useful in electronic devices due to the fact that they are generally insulating in the absence of an external stimulus. However,

semiconductors can be chemically doped such that there is an excess of delocalised or mobile electrons (n-type) or holes (p-type) within the material. Such is the case of silicon, the mostly widely used conventional semiconductor material. Silicon can be made p-type by doping with group III elements, e.g. boron, which cause the material to be electron deficient, and n-type when doped with group V elements, e.g. phosphorus, which cause the material to become electron rich.[5] Through doping, a concentration of mobile charge carriers is introduced causing the material to become conductive. This is illustrated in **Figure 2.4**.

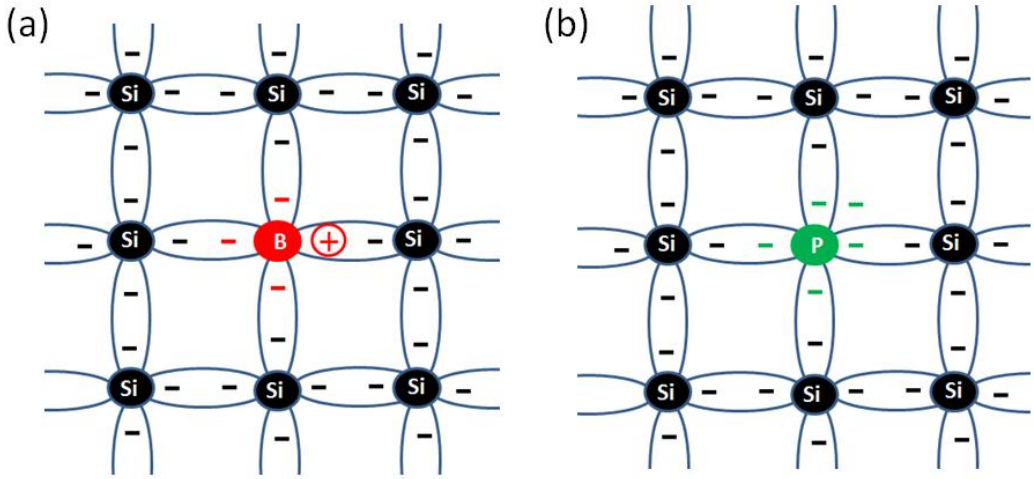

Figure 2.4: (a) Illustration of the bonding in p-type silicon, where the dopant atom is the group III element boron, B. The boron atom sits in the site of a silicon atom, but having only 3 valence electrons, creates an electron vacancy or hole. This hole is then a mobile charge carrier. (b) Bonding in n-type silicon. Here the dopant atom is the group V element phosphorus, P, which having 5 valence electrons, creates an electron rich material where the mobile charge carriers are electrons. The valence electrons of P are shown in green, while the valence electrons on B are shown in red.

2.2 Operating Principles of Photovoltaics

The operating principles of photovoltaic devices can be separated into 3 main categories:

1. Light absorption and exciton generation
2. Exciton separation
3. Charge collection

2.2.1 Light Absorption and Charge Generation

The amount of light absorbed by a material is determined by its band gap. The only photons which are absorbed by a material are those which possess an energy which is equal to or greater than the band gap. This absorption of light then results in the photoexcitation of an electron from the valence band (ground state) to the conduction band (excited state). For photons which possess energy higher than the band gap of a material, the excess energy is lost as heat, whereas photons with energy less than the band gap are either reflected or transmitted through the material. The absorption onset of a material then occurs at the wavelength which corresponds to its band gap. The Air Mass 1.5 (AM 1.5) solar spectrum which is incident on the earth's surface is shown in **Figure 2.5**.

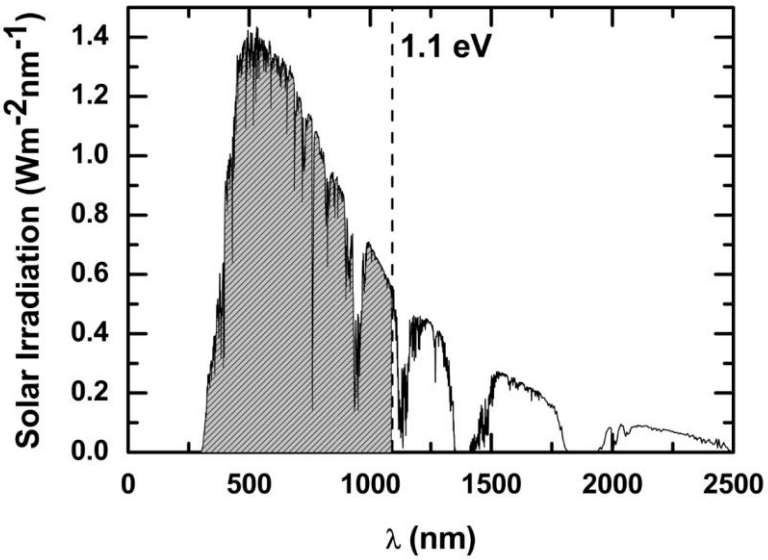

Figure 2.5: Solar irradiance vs. wavelength (λ) for the AM 1.5 solar spectrum incident on the earth's surface. The absorption spectrum of crystalline silicon (E_g = 1.1 eV) is shaded in grey.[6]

In 1961, a theoretical study by Shockley and Queisser showed the ideal band gap of a photoactive material to be 1.1 eV(assuming black body emission at 6000 K), corresponding to a maximum theoretical efficiency of approximately 30 %, assuming that all electron-hole recombination is radiative.[7] One such material is crystalline silicon which has a band gap of 1.1 eV, corresponding to an absorption onset of 1127 nm. Photovoltaic devices based on crystalline silicon have achieved power conversion efficiencies of over 25 %.The proportion of the solar spectrum absorbed by crystalline silicon is shown in Figure 2.5.

2.2.2 Charge Separation

When photoexcited charges are generated, the electron and its corresponding hole are still bound via Coulombic attraction. An electron-hole pair such as this is referred to an exciton. The strength and range of this Coulombic attraction, or binding energy, is heavily dependent on the specific material under investigation. For a given compound, the dielectric constant governs the binding energy of any excitons generated. For example, in a material with a high dielectric constant such as crystalline inorganic semiconductors, e.g. Si and Ge, the Coulombic attraction holding the exciton is effectively screened by the material. This results in the dominant charged species being free electrons and holes as opposed to excitons, at room temperature. Most organic semiconductors have low dielectric constants, and as such, at room temperature the reverse is true with the dominant charged species being excitons, which can then be separated by using a donor-acceptor type system.[3,8]

A conventional Si solar cell is a sandwich of p-doped and n-doped material, typically referred to as a p-n junction. In such a structure, holes in the p-doped material diffuse towards the n-doped material and vice versa. This results in the formation of a depletion region which acts as an intrinsic electric field, causing electrons to be pushed to the n-doped side of the junction and holes to be pushed to the p-type side of the junction, effectively causing separation of the charges. This is shown in the band diagram presented in **Figure 2.6**.

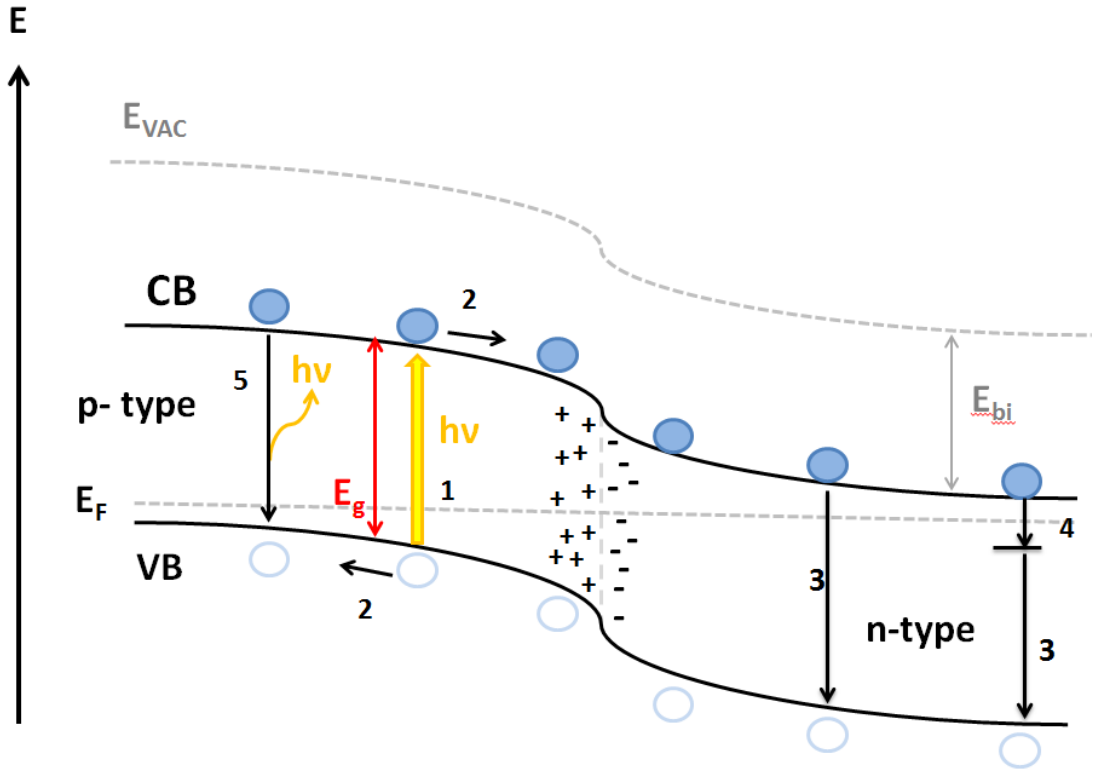

Figure 2.6: Formation of a depletion region at a p-n junction, along with electronic processes occurring in a photovoltaic device. This depletion region forms a built-in electric field which forces electrons to the n-doped side of the bilayer, and holes to the p-doped side. (1) Photoexcitation of an electron from the VB to the CB. (2) Movement of electron and hole to the corresponding p-type and n-type material. (3) Non-radiative recombination of a CB electron with a VB hole. (4) Trapping of a CB electron in a shallow trap, a process typically followed by (3). (5) Radiative recombination of an electron-hole pair.

2.2.3 Charge Collection

In order for charges to be efficiently extracted from a photovoltaic device, electron and hole selective contacts must be placed on the n-type and p-type sides of the p-n junction. This is essential to ensuring that only electrons can be collected at the anode and vice versa. The band diagram shown in Figure 2.6 depicts the electronic processes which typically occur in a conventional Si solar cell. Upon light absorption and generation of additional free charge within the device (1), the built in electric field aids in rapidly causing electrons to be swept to the n-type layer and holes to the p-type layer. This happens through a superposition of drift currents and diffusion currents which can be expressed by the following equation:[3]

$$J = q\left(n\mu_n + n\mu_p\right)E + q\left(D_n\,\Delta n - D_p\,\Delta p\right) \qquad (2.7)$$

Where J is the photocurrent generated, E is the electric field, D is the diffusion constant and p and n are the concentrations of photogenerated holes and electrons respectively.

The photocurrent which is extracted from a photovoltaic device is limited by a number of different electronic processes which are likely to occur. The leading cause of a reduction in photocurrent is recombination. This can occur in a variety of different ways, and at different parts of the device. Recombination can occur at the contacts, within the absorber layer or at the interface between the p-type and n-type materials. The most prevalent form of recombination occurs between an electron in the CB and a hole in the VB, a process which is typically associated with the loss of energy through heat or light, as the electron returns to its ground state energy.

In the case of materials which do not possess exceptional purity, as is the case with most solution processed materials, poor crystallization and inadequate film formation often lead to the formation of defect sites within the material. These defects can take the form of under-coordinated atoms within the crystal structure, grain boundaries between crystals, or interface defects which form at a junction between two materials. These structural defects can act as localised, low energy trap states within a material, and can exist as either hole or electron traps. In the case of shallow or low energy trap sites, it is possible for trapped charge carriers to be thermally excited enough to be de-trapped; however, for deep or high energy trap sites, this is no longer possible and as such those carriers are effectively immobilised, thus reducing the photocurrent of the device. Even in the case of shallow trap sites, the time taken for the trapping and de-trapping of charge carriers decreases the rate of charge extraction and thus the maximum photocurrent which can be acquired from the device. This charge trapping process can easily be followed by recombination. This is depicted in (4) and (3) of Figure 2.6.

2.3 Characterisation of Photovoltaic Devices

In a complete photovoltaic device, a photocurrent is generated under illumination. When there is no external voltage applied, i.e., no load, the device is said to be under short circuit conditions, and the current extracted is known as the short circuit current (J_{SC}). If a voltage is applied such that is opposite and equal to the built in electric field of the device, this causes the flow of current to cease. This condition is known as open circuit voltage (V_{OC}). The maximum V_{OC} which can be garnered from a device is defined as the difference in the potential of the quasi-Fermi level for electrons and holes. If the bias applied to the device is reversed, the charge carriers are forced in the opposite direction, which then has

the effect of increasing the size of the depletion region until the flow of majority carriers is effectively reduced to zero. Current extracted from a photovoltaic device under these conditions is known as the reverse saturation, or dark current. The current density in any semiconducting p-n junction or diode, can be described by Shockley's equation which is otherwise known as the ideal diode equation, and is given in **Equation 2.8**.

$$J = J_s \left(e^{qV_A/kT} - 1\right) \tag{2.8}$$

where V_A is the voltage applied across the diode under forward bias conditions, and J_s is the reverse saturation current which being closely related to the recombination dynamics of the system, varies from case to case.

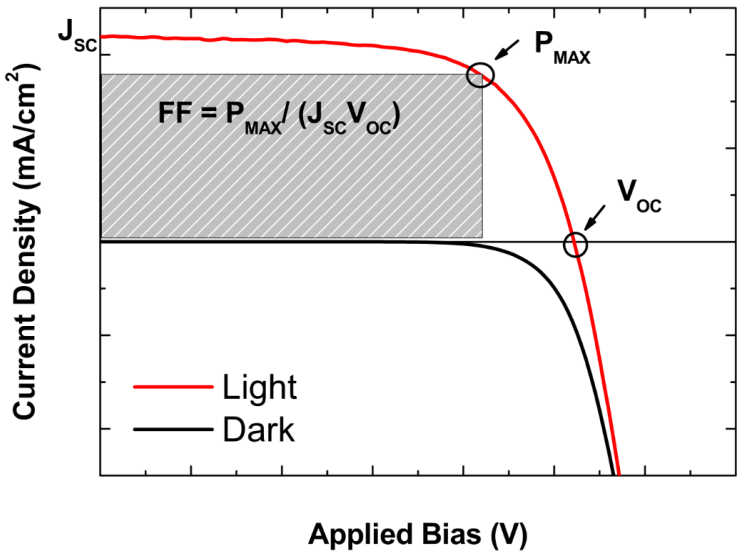

Figure 2.7: Typical current density-voltage characteristics of an operational solar cell. The dark current is shown with a black line, while the response of the device under illumination is shown in red. Important performance metrics such as the J_{SC}, *F.F.*, V_{OC}, and P_{MAX} are also illustrated on the light JV curve.

The operation of a solar cell is frequently characterised by the investigation of its current-voltage (J-V) curves. An example of such a curve is given in **Figure 2.7**. The noteworthy parameters which can be obtained from this curve are the J_{SC}, V_{OC}, the fill factor (*FF*) and the power conversion efficiency (η). The maximum power point (P_{MAX}) is the point at which the product of the current density, *J*, and the voltage, *V*, reaches its maximum value. The FF is essentially a measure of the "squareness" of a JV curve, or how close the performance of the device is to ideal. Some of factors which can influence the FF of a device are the recombination dynamics of the material itself and high series or shunt resistances. The power conversion efficiency (PCE) of a photovoltaic device is defined by **Equation 2.10**

$$FF = \frac{P_{MAX}}{J_{sc}V_{oc}} \tag{2.9}$$

$$\eta = \frac{J_{SC}V_{OC}FF}{P_i} \tag{2.10}$$

where P_i is defined as the incident power.

2.4 Operational Principles of Solid-State Sensitized Solar Cells

While the idea of the sensitized solar cell (SSC) had been around since 1887,[9] it gained extreme popularity in 1991 when Grätzel and O'Regan presented a low cost, dye-sensitized solar cell (DSSC) with a power conversion efficiency (PCE) > 7%.[10] The major breakthrough in this technology was the introduction of a mesoporous layer of TiO_2 which

greatly increased the surface area for the adsorption to dye molecules. While the PCEs of these devices have now exceeded 12 %,[11] the major hindrance to commercialisation is the presence of the liquid electrolyte. This presents issues of leakage and corrosion which are undesirable when attempting to produce a device which possesses long term stability. In order to combat this problem the solid-state sensitized solar cell (ss-SSC) was birthed.[12] The ss-SSC replaces the corrosive liquid electrolyte with solid-state molecular or polymeric hole transporting materials (HTM) such as 2,2′,7,7′-tetrakis(N,N′-di-p-methoxyphenylamine)-9,9′-spirobifluorene (spiro-OMeTAD) or regioregular poly(3-hexylthiophene) respectively.[12,13] Replacing the liquid electrolyte with a solid state HTM also opened up avenues to using solution processable absorber materials other than organic dyes, as the corrosive nature of this redox couple often resulted in the dissolution of the absorber layers.[14] For these reasons, this thesis focuses solely on solar cells incorporating solid state HTMs.

A pictoral representation of a typical SSC is shown in **Figure 2.8**. In a conventional p-n junction type solar cell such as Si; light absorption, charge generation, charge separation and charge extraction all take place within the semiconductor layer. One of the salient differences between conventional photovoltaic devices and the SSC is that in the SSC, all these processes occur in different materials, which have been specially engineered to carry out these tasks. Here, light absorption takes place in the absorber material, which can be either an organic dye such as the ruthenium-based dye N719, the indoline dye D102, or a solution processable, inorganic absorber material such as Sb_2S_3 (both of these materials will be discussed in further detail in Chapters 4 and 5). An electron from the absorber material is then promoted to the excited state, leaving a hole behind in the absorber material. This is illustrated as process 1 in Fig. 2.8. At the interface between the electron conducting (TiO_2) and hole conducting materials charge separation occurs. This is shown as processes 3 and 4 in Fig.2.8. Here, the electron is injected into the conduction band of the TiO_2 and the hole is transported through the HTM.[12] These processes take place

on femtosecond and nanosecond timescales respectively.[15,16] Electron transport through the TiO_2 takes place through a multiple trapping and detrapping mechanism,[17-19] while holes are transported to the HTM via a hole hopping mechanism.[20] As in the operation of a conventional Si cell, recombination mechanisms do occur and will be discussed in further detail.

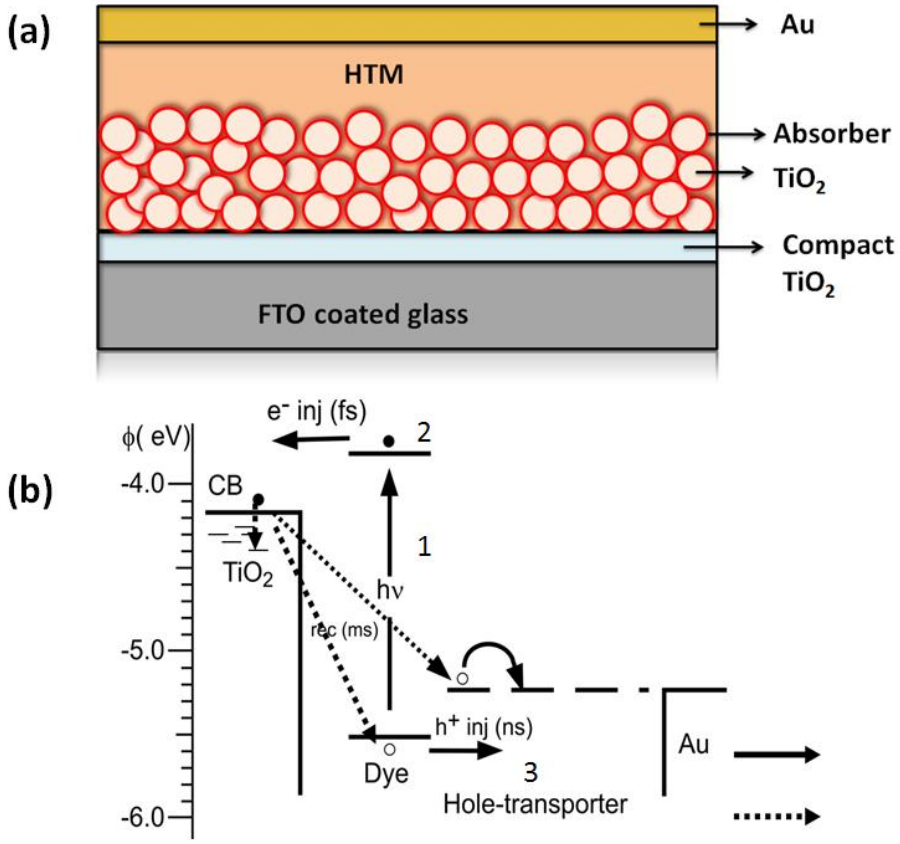

Figure 2.8: (a) Schematic of a typical solid state sensitized solar cell (ss-SSC). The compact layer of TiO_2 is usually approximately 100 nm thick, while the mesoporous layer formed by nanoparticles of TiO_2 often ranges in thickness from 0.5 μm to 3 μm. The capping layer of the hole transport material (HTM) is typically 200 nm thick, while the gold electrodes range anywhere from 50 nm to 200 nm in thickness. It is important to note that in this structure, the HTM infiltrates the pores of the TiO_2 such that it (b) Electronic processes occurring in a ss-SSC, where (1) is the

photoexcitation of an electron from the dye into an excited state, (2) followed by the injection of the electron into the conduction band of the TiO_2 and (3) and the hole into the hole transporter, where the charges can then be transported to the respective electrodes. This is discussed in further detail in the main text. Figure 2.8b has been reproduced with permission from EPFL Press.[21]

2.3.1 Charge Generation

As previously mentioned, when light is absorbed by the dye or inorganic absorber material used in an ss-SSC, it provides enough energy to promote an electron to the excited state of the absorber, resulting in the formation of a hole in the absorber. At this point, the electron can either be injected into the CB of the TiO_2, or it can recombine with the hole in the absorber. However, as electron injection into the TiO_2 occurs on quite a fast timescale (fs),[15] recombination is negligible at this stage. The absorber is now positively charged, and is regenerated by hole transfer to the HTM, a process which occurs on the picosecond timescale.[16] This process occurs so efficiently as a result of careful engineering of the energy offsets between the CB of the TiO_2 and the CB or LUMO of the absorber, as well as between the HOMO and the oxidation potential of the HTM. These energetic cascades are designed to allow efficient separation of charge carriers and reduce recombination. One downside to this is that the loss in potential which occurs when electrons are injected into the TiO_2 significantly decreases the maximum voltage which can be achieved by the device, usually by 200-300 meV. This is also illustrated in Fig. 2.8b.

2.3.2 Electron Transport through TiO_2

As discussed above, in conventional inorganic semiconductor based photovoltaics, such as Si and GaAs, the magnitude of the built-in potential within these devices causes charges to drift to their appropriate contacts. Therefore, in such a case charge transport is largely dominated by drift currents. In the case of the ss-SSC however, charge transport is primarily governed by the diffusion of charges to selective contacts.[20] Under illumination, charges are constantly injected into the TiO_2 resulting in the build-up of a high concentration of electrons at the TiO_2/dye interface, and a low concentration of electrons at the selective electrode where charge extraction occurs. This essentially establishes a concentration gradient which aids the diffusion of charges and allows charge collection.[22]

Electron transport through TiO_2 has been described by a multiple trapping model.[17-19] One of the strongest pieces of experimental evidence which support this model is the large difference in the charge mobilities of single crystalline and nanocrystalline TiO_2, where the mobility of nanocrystalline TiO_2 is several orders of magnitude less than that of its single crystalline counterpart ($\mu = 10$ cm^2 V^{-1} s^{-1} vs. $\mu = 10^{-1} - 10^{-5}$ cm^2 V^{-1} s^{-1}).[23-26] The sintering together of TiO_2 nanoparticles to form a mesoporous network has certain drawbacks, chief of which is the introduction of a high density of sub-band gap states, which results in a large degree of electronic disorder within the material.[20] This is likely to arise from surface defects within the film, such as deviations from stoichiometry, grain boundaries and inadequate electronic contact between individual nanoparticles.[27-29] Electrons then move through the randomly oriented TiO_2 network via a series of trapping and de-trapping events, where they can be trapped in these sub-band gap states and then thermally excited out of the traps back into the conduction band of the TiO_2. The distribution and the energy of the trap states (whether they are deep traps or shallow traps)

governs the length of time that the electron remains trapped and the overall mobility of charges in the film, explaining the large decrease in mobility which is observed for nanocrystalline films of TiO_2 as opposed to single crystal anatase.

Charge transport in ss-DSSCs has recently been shown to be electron limited under operating conditions,[24,30] suggesting that the operation of such devices is limited by the electron transport rate through TiO_2. It is then no surprise that improving the architecture of the mesoporous electrode, with specific emphasis placed on improving the charge transport in such devices, has been a burgeoning area of research. One approach has been to employ structures such as nanorods, nanowires and nanotubes, and while these structures have shown improvements in the transport rate, devices fabricated via this route typically suffer from a large reduction in the surface area which is available for dye adsorption.[31]

Given that the main advantage of the nanoparticulate layer is its high surface area, and nanowires and single crystalline TiO_2 seem to exhibit faster electron transport properties, it stands to reason that the fabrication of a single crystal of TiO_2 which exhibits internal porosity may then be the ultimate solution to the problems of electrode architecture and transport. This has resulted in the fabrication of mesoporous single crystals of TiO_2 which have been found to exhibit enhanced electronic performance in ss-DSSCs. These results will be discussed in Chapter 4.

2.3.3 Hole Transport in the Hole Transport Material

The most commonly used HTM in ss-SSCs is a small, triphenylamine based molecule 2,2′,7,7′-tetrakis(N,N′-di-p-methoxyphenylamine)-9,9′-spirobifluorene, which is commonly referred to as spiro-OMeTAD. Introduced by Bach and Grätzel in 1998, this material is still used in most of the best performing ss-SSCs, and indeed is the HTM of choice throughout the majority of this thesis. The chemical structure of the material is given in **Figure 2.9**. The mechanism of charge transport in solid-state HTMs also takes place via a charge diffusion method, through what may best be described as a hole hopping process.[32]

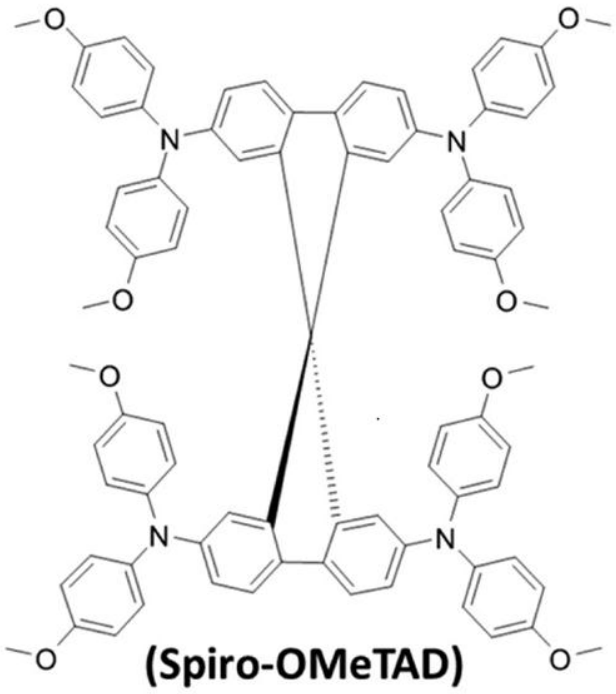

Figure 2.9: Chemical structure of spiro-OMeTAD.

When photoexcited electrons are generated, their corresponding holes remain at the interface between the dye and the HTM. The holes are then transported through the HTM via diffusion, and are collected at the cathode. The mobility of neat or undoped spiro-OMeTAD has been determined to be on the order of 10^{-4} cm^2 V^{-1} s^{-1}.[33] In a typical ss-SSC, spiro-OMeTAD is doped with the ionic additive, bis(trifluoromethylsulfonyl)amine lithium salt, more commonly known as Li-TFSI. Doping with this additive has been shown to increase the conductivity of the HTM by up to 100 times, with the hole mobility increasing by an order of magnitude, up to approximately 10^{-3} cm^2 V^{-1} s^{-1}.[20]

2.5 Alternative Sensitizers

One of the main disadvantages of using dyes as light absorbers in ss-SSCs, is that optimal performance is achieved when a monolayer of dye is adsorbed onto the surface of the mesoporous oxide,[34,35] making it quite challenging to achieve high enough surface area for dye loading while operating in the optimal thickness regime of 1 μm- 3 μm.[20,36] The solid state semiconductor-sensitized solar cell (ss-SSSC) is an example of a device which seeks to enhance light absorption in this particular configuration, and can be subdivided into two major classes: the extremely thin absorber (ETA) solar cell and the quantum dot sensitised solar cell (QDSC). These types of solar cells typically utilise inorganic semiconducting materials as the light absorber layer. Inorganic materials have many attractive features such as having higher molar extinction coefficients than their organometallic or organic counterparts,[37] high intrinsic carrier mobilities,[38] large intrinsic dipole moments and also present the opportunity to tune the band gap of the absorber by exploiting quantum size effects.[39,40] Additionally, inorganic absorbers have increased

thermodynamic and optical stability than organic or metal-organic dyes. Indeed, for equivalent device configurations, a ss-SSSC can exhibit absorption which is five times greater than that of its organic counterpart[41] which has made light absorbing semiconductors prime candidates for incorporation into the SSCs.

Given the advantages of replacing organic dyes with inorganic semiconductors, it is no surprise that the sensitization of mesoporous oxides by such materials has been widely studied.[39,42-45] The SSSC has in fact achieved most of its success in the solid state configuration, owing to the fact that the liquid electrolyte tends to corrode the absorber, thus having detrimental effects on device performance.[41,43,46,47] Inorganic semiconductors have been deposited onto the mesoporous metal oxide in a variety of ways. In the case of ETA cells, it has been grown directly onto the wide band gap metal oxide using chemical bath deposition (CBD)[46,48-51] or successive ionic layer adsorption and reaction (SILAR).[52-54] Conversely, as is often done in the case of QDSCs, it can be attached to its surface of the oxide either directly, or through a functionalized molecular linker.[55,56]

Two important considerations in the fabrication of ss-SSSCs have been the extent of the surface coverage of the mesoporous oxide and the thickness of the absorber layer which is deposited as these factors have been shown to have an effect on the degree of recombination and the quantum efficiency of the solar cell. For example, while methods like CBD and SILAR impart a high degree of surface coverage, devices prepared by this method also exhibit increased levels of internal recombination [57] while depositing too thick an absorber layer has been shown to decrease the quantum efficiency of the device.[39,58,59] In the case where a thick absorber layer is deposited onto the mesoporous oxide, there will be a decrease in the rate of electron transfer into the oxide thus increasing the possibility of geminate recombination. Conversely, a method which may not necessarily impart high

surface coverage also increases the possibility of direct contact between the electron conducting and the hole conducting layers, also resulting in increased recombination. One method of combating this type of recombination is to incorporate a buffer layer. The presence of this additional layer of material has the ability to act as a blocking layer between the electron conducting and hole conducting materials and is almost essential in the majority of ETA cells.[41]

While many inorganic absorbers have been incorporated into SSSC device structures using the methods mentioned above, the most promising absorbers have been the lead and antimony chalcogenides. QDSCs using PbS as a sensitizer have achieved efficiencies of 1.3% using spiro-OMeTAD.[60] However, Sargent et al., have achieved 7% efficient solar cells through a robust, and novel method of passivating surface traps in these nanocrystals, attaining a new record for PbS solar cells. [61] Sb_2S_3 is an inorganic absorber which has been incorporated into many novel devices, but has achieved optimal performance in solid state devices. This material has been used in SSSCs with various HTMs such as spiro-OMeTAD,[62] copper thiocyanate (CuSCN)[63] and poly-(3-hexylthiophene) (P3HT),[48] yielding power conversion efficiencies of 3.1%, 3.37% and 5.13% respectively. The highest reported efficiency for an Sb_2S_3 photovoltaic device is 6.3%, obtained using a blend of PCPDTBT and PCBM as both a hole transporter as well as a light absorber.[49] The use of Sb_2S_3 as an absorber material is investigated in Chapter 5 of this thesis.

2.6 Perovskite Solar Cells

One of the main advantages of third generation solar cells, such as the DSSCs and SSSCs discussed here has been the greatly reduced production cost. However, over the last 12 years, marginal increases in the efficiency of these devices have not allowed this technology to become a large scale competitor for Si based photovoltaics. Recently, a family of semiconducting, organometallic halide absorbers has emerged and attracted immense research interest. These hybrid materials constitute a part of the perovskite family, having the calcium titanate crystal structure, ABX_3 and have, in a short space of time, outperformed both DSSCs and SSSCs. This family of materials has been shown to operate efficiently not only as sensitizers,[14,64-68] but also as charge transport materials,[64,68-70] and with further research, is poised to deliver the elusive goal of a low cost, high efficiency photovoltaic device.

The first notable report of a perovskite-based solar cell came in 2009 when Miyasaka and co-workers described the use of the methylammonium triiodide and methlyammonium tribromide plumbates ($CH_3NH_3PbI_3$ and $CH_3NH_3PbBr_3$ respectively) as the sensitizers in the liquid electrolyte SSSC configuration.[65] In this study, the triiodide perovskite achieved a power conversion efficiency of 3.81%. Shortly thereafter, Park et al. improved on Miyasaka's work by optimising device processing conditions and presented a 6.5% liquid electrolyte SSSC, using $CH_3NH_3PbI_3$ as the sensitizer.[14] The main problem with this liquid electrolyte embodiment of this device, as with most other SSSCs, is that the perovskite is quickly corroded by the liquid electrolyte. [14,65] Decreasing the thickness of the titania layer, along with a switch to the solid-state hole conductor, spiro-OMeTAD, greatly increased the conversion efficiency of the $CH_3NH_3PbI_3$ sensitized device, increasing it to over 9%.[66]

While these absorbers are made from earth abundant materials, perhaps one of the most attractive prospects is their solution processability. While traditional perovskite synthesis is typically solid-state and involves annealing at temperatures ≥ 1100 ˚C,[71] these organometallic hybrids can be formed from either drying a solution of precursor salts, or grinding the salts together, thus promoting an interface reaction.[65] This method of synthesis makes it relatively facile to manipulate the chemical composition of this class of perovskites. The mixed halide perovskite $CH_3NH_3PbI_{3-x}Cl_x$ was first reported by Lee et al. in 2012, yielding a power conversion efficiency of almost 8% in a sensitized configuration.[64] Interestingly, this material achieved an efficiency of 10.9% using Al_2O_3 as the mesoporous layer. This mixed halide perovskite was shown to not only absorb strongly over a very broad spectral range, but also to transport electrons. The use of this insulating oxide presented a deviation from the classical sensitized configuration and gave rise to a new technology termed the meso-superstructured solar cell (MSSC).[64]

The band gap of the $CH_3NH_3PbI_3$ can easily be tuned by either completely replacing the iodine with another halogen, or by changing the ratio of the halogens in a mixed halide configuration. Through tuning the band gap by varying the I to Br ratio in the $CH_3NH_3Pb(I_{1-x}Br_x)_3$, Noh and co-workers produced perovskites of a broad range of colours, and using polytriarylamine (PTAA) as a hole conductor, achieved 12.3% in the sensitized configuration.[72]

In another stride towards a low cost, high efficiency, perovskite solar cell, a recent publication by Ball et al. showed a reduction in both the thickness and the processing temperature of the alumina scaffold in MSSCs, resulting in the efficiency of the optimised device being 12.3%.[73] The reduction of the processing temperature of the inorganic scaffold from ≥ 500˚C to ≤ 150˚C widens the choice of substrate to relatively inexpensive plastics and metal foils and opens the door to multi-junction device architectures, greatly

extending the potential utility of these devices, while reducing the thickness of the scaffold causes yet another paradigm shift; this time away from the MSSC configuration and towards a thin film architecture. A further potential reduction in cost has been achieved employing $CH_3NH_3PbI_{3-x}Cl_x$ in a conventional thin film architecture by completely removing the insulating scaffold, and still retaining the high conversion efficiency of 11.4%.[74]

The performance of perovskite devices has been shown to depend strongly on the crystallization of the perovskite and to what degree it covers the substrate. Until fairly recently, the main method used to deposit the perovskite, was to spin coat a precursor solution and evaporate the solvent, thus forming perovskite crystals on the substrate. Recent studies have presented alternative ways of perovskite deposition such as evaporation[75,76] and sequentially depositing the metal halide and methylammonium salt onto the mesoporous layer.[67,68] Currently, the highest certified efficiency of a perovskite based solar cell rests at 17.9 %. [77] Chapter 6 of this thesis explores passivation as a means to increase the efficiency of lead-based perovskite solar cells.

Still, one of the potential drawbacks of this technology is the presence of lead in the perovskite material. While the amount of lead which is used is fairly small, the use of lead may still prove to be a barrier to large scale commercialisation. To this end lead-free perovskites have been investigated. Chapters 7 and 8 present tin-based, lead-free perovskite materials as potential alternatives for these highly efficient lead based materials.

2.6 References

[1] Hook, J. R. & Hall, H. E. *Solid State Physics*. (Wiley, 2013).

[2] Rosenberg, H. M. *The Solid State: An Introduction to the Physics of Solid*. (Oxford University Press, 1995).

[3] Nelson, J. *The Physics of Solar Cells*. (Imperial College Press, 2003).

[4] Würfel, P. *Physics of Solar Cells: From Principles to New Concepts*. (Wiley, 2008).

[5] Boylestad, R. N., L. *Electronic Devices and Circuit Theory*. (Pearson Education, 2000).

[6] N.R.E.L. *Astm g173-03 tables: Extraterrestrial spectrum, terrestrial global 37 deg south facing tilt and direct normal + circumsolar*, <http://rredc.nrel.gov/solar/spectra/am1.5/> (1999).

[7] Shockley, W. & Queisser, H. J. Detailed Balance Limit of Efficiency of p-n Junction Solar Cells. *Journal of Applied Physics* **32**, 510-519, doi:doi:http://dx.doi.org/10.1063/1.1736034 (1961).

[8] Brabec, C., Scherf, U. & Dyakonov, V. *Organic Photovoltaics: Materials, Device Physics, and Manufacturing Technologies*. (Wiley, 2014).

[9] Moser, J. Notiz über Verstärkung photoelektrischer Ströme durch optische Sensibilisirung. *Monatshefte für Chemie* **8**, 373-373, doi:10.1007/BF01510059 (1887).

[10] O'Regan, B. & Gratzel, M. A low-cost, high-efficiency solar cell based on dye-sensitized colloidal TiO2 films. *Nature* **353**, 737-740 (1991).

[11] Yella, A. *et al.* Porphyrin-Sensitized Solar Cells with Cobalt (II/III)–Based Redox Electrolyte Exceed 12 Percent Efficiency. *Science* **334**, 629-634, doi:10.1126/science.1209688 (2011).

[12] Bach, U. *et al.* Solid-state dye-sensitized mesoporous TiO2 solar cells with high photon-to-electron conversion efficiencies. *Nature* **395**, 583-585 (1998).

[13] Abrusci, A. *et al.* Influence of Ion Induced Local Coulomb Field and Polarity on Charge Generation and Efficiency in Poly(3-Hexylthiophene)-Based Solid-State Dye-Sensitized Solar Cells. *Advanced Functional Materials* **21**, 2571-2579, doi:10.1002/adfm.201100048 (2011).

[14] Im, J.-H., Lee, C.-R., Lee, J.-W., Park, S.-W. & Park, N.-G. 6.5% efficient perovskite quantum-dot-sensitized solar cell. *Nanoscale* **3**, 4088-4093, doi:10.1039/C1NR10867K (2011).

[15] Tachibana, Y., Moser, J. E., Grätzel, M., Klug, D. R. & Durrant, J. R. Subpicosecond interfacial charge separation in dye-sensitized nanocrystalline titanium dioxide films. *The Journal of Physical Chemistry* **100**, 20056-20062 (1996).

[16] Bach, U. *et al.* Charge separation in solid-state dye-sensitized heterojunction solar cells. *Journal of the American Chemical Society* **121**, 7445-7446 (1999).

[17] Benkstein, K. D., Kopidakis, N., van de Lagemaat, J. & Frank, A. J. Influence of the Percolation Network Geometry on Electron Transport in Dye-Sensitized Titanium Dioxide Solar Cells. *The Journal of Physical Chemistry B* **107**, 7759-7767, doi:10.1021/jp022681l (2003).

[18] O'Regan, B. C. & Durrant, J. R. Kinetic and Energetic Paradigms for Dye-Sensitized Solar Cells: Moving from the Ideal to the Real. *Accounts of Chemical Research* **42**, 1799-1808, doi:10.1021/ar900145z (2009).

[19] Bisquert, J. Chemical Diffusion Coefficient of Electrons in Nanostructured Semiconductor Electrodes and Dye-Sensitized Solar Cells. *The Journal of Physical Chemistry B* **108**, 2323-2332, doi:10.1021/jp035397i (2004).

[20] Snaith, H. J. & Schmidt-Mende, L. Advances in Liquid-Electrolyte and Solid-State Dye-Sensitized Solar Cells. *Advanced Materials* **19**, 3187-3200, doi:10.1002/adma.200602903 (2007).

[21] Kalyanasundaram, K. *Dye-sensitized Solar Cells*. (EFPL Press, 2010).

[22] Peter, L. M. Dye-sensitized nanocrystalline solar cells. *Physical Chemistry Chemical Physics* **9**, 2630-2642, doi:10.1039/B617073K (2007).

[23] Tang, H., Prasad, K., Sanjinès, R., Schmid, P. E. & Lévy, F. Electrical and optical properties of TiO2 anatase thin films. *Journal of Applied Physics* **75**, 2042-2047, doi:doi:http://dx.doi.org/10.1063/1.356306 (1994).

[24] Leijtens, T., Lim, J., Teuscher, J., Park, T. & Snaith, H. J. Charge Density Dependent Mobility of Organic Hole-Transporters and Mesoporous TiO2 Determined by Transient Mobility Spectroscopy: Implications to Dye-Sensitized and Organic Solar Cells. *Advanced Materials* **25**, 3227-3233, doi:10.1002/adma.201300947 (2013).

[25] Tiwana, P., Parkinson, P., Johnston, M. B., Snaith, H. J. & Herz, L. M. Ultrafast Terahertz Conductivity Dynamics in Mesoporous TiO2: Influence of Dye Sensitization and Surface Treatment in Solid-State Dye-Sensitized Solar Cells. *The Journal of Physical Chemistry C* **114**, 1365-1371, doi:10.1021/jp908760r (2009).

[26] Tiwana, P., Docampo, P., Johnston, M. B., Snaith, H. J. & Herz, L. M. Electron Mobility and Injection Dynamics in Mesoporous ZnO, SnO2, and TiO2 Films Used in Dye-Sensitized Solar Cells. *ACS Nano* **5**, 5158-5166, doi:10.1021/nn201243y (2011).

[27] Hagfeldt, A., Boschloo, G., Sun, L., Kloo, L. & Pettersson, H. Dye-Sensitized Solar Cells. *Chemical Reviews* **110**, 6595-6663, doi:10.1021/cr900356p (2010).

[28] van de Lagemaat, J. & Frank, A. J. Nonthermalized Electron Transport in Dye-Sensitized Nanocrystalline TiO2 Films: Transient Photocurrent and Random-Walk Modeling Studies. *The Journal of Physical Chemistry B* **105**, 11194-11205, doi:10.1021/jp0118468 (2001).

[29] Bisquert, J. Hopping Transport of Electrons in Dye-Sensitized Solar Cells. *The Journal of Physical Chemistry C* **111**, 17163-17168, doi:10.1021/jp077419x (2007).

[30] Snaith, H. J. & Grätzel, M. Electron and Hole Transport through Mesoporous TiO2 Infiltrated with Spiro-MeOTAD. *Advanced Materials* **19**, 3643-3647, doi:10.1002/adma.200602085 (2007).

[31] Tetreault, N. & Gratzel, M. Novel nanostructures for next generation dye-sensitized solar cells. *Energy & Environmental Science* **5**, 8506-8516, doi:10.1039/C2EE03242B (2012).

[32] Poplavskyy, D. & Nelson, J. Nondispersive hole transport in amorphous films of methoxy-spirofluorene-arylamine organic compound. *Journal of Applied Physics* **93**, 341-346, doi:doi:http://dx.doi.org/10.1063/1.1525866 (2003).

[33] Hao, F. *et al.* Recent advances in alternative cathode materials for iodine-free dye-sensitized solar cells. *Energy & Environmental Science* **6**, 2003-2019, doi:10.1039/C3EE40296G (2013).

[34] Khazraji, A. C., Hotchandani, S., Das, S. & Kamat, P. V. Controlling Dye (Merocyanine-540) Aggregation on Nanostructured TiO2 Films. An Organized Assembly Approach for Enhancing the Efficiency of Photosensitization. *The Journal of Physical Chemistry B* **103**, 4693-4700, doi:10.1021/jp9903110 (1999).

[35] Yum, J.-H., Chen, P., Grätzel, M. & Nazeeruddin, M. K. Recent Developments in Solid-State Dye-Sensitized Solar Cells. *ChemSusChem* **1**, 699-707, doi:10.1002/cssc.200800084 (2008).

[36] Snaith, H. J. *et al.* Charge collection and pore filling in solid-state dye-sensitized solar cells. *Nanotechnology* **19**, doi:10.1088/0957-4484/19/42/424003 (2008).

[37] Yu, W. W., Qu, L., Guo, W. & Peng, X. Experimental Determination of the Extinction Coefficient of CdTe, CdSe, and CdS Nanocrystals. *Chemistry of Materials* **15**, 2854-2860, doi:10.1021/cm034081k (2003).

[38] Huynh, W. U., Dittmer, J. J. & Alivisatos, A. P. Hybrid Nanorod-Polymer Solar Cells. *Science* **295**, 2425-2427, doi:10.1126/science.1069156 (2002).

[39] Vogel, R., Pohl, K. & Weller, H. Sensitization of highly porous, polycrystalline TiO2 electrodes by quantum sized CdS. *Chemical Physics Letters* **174**, 241-246, doi:http://dx.doi.org/10.1016/0009-2614(90)85339-E (1990).

[40] Alivisatos, A. P. Semiconductor Clusters, Nanocrystals, and Quantum Dots. *Science* **271**, 933-937, doi:10.1126/science.271.5251.933 (1996).

[41] Hodes, G. Comparison of Dye- and Semiconductor-Sensitized Porous Nanocrystalline Liquid Junction Solar Cells. *The Journal of Physical Chemistry C* **112**, 17778-17787, doi:10.1021/jp803310s (2008).

[42] Vogel, R., Hoyer, P. & Weller, H. Quantum-Sized PbS, CdS, Ag2S, Sb2S3, and Bi2S3 Particles as Sensitizers for Various Nanoporous Wide-Bandgap Semiconductors. *The Journal of Physical Chemistry* **98**, 3183-3188, doi:10.1021/j100063a022 (1994).

[43] Zaban, A., Mićić, O. I., Gregg, B. A. & Nozik, A. J. Photosensitization of Nanoporous TiO2 Electrodes with InP Quantum Dots. *Langmuir* **14**, 3153-3156, doi:10.1021/la9713863 (1998).

[44] Hotchandani, S. & Kamat, P. V. Charge-transfer processes in coupled semiconductor systems. Photochemistry and photoelectrochemistry of the colloidal cadmium sulfide-zinc oxide system. *The Journal of Physical Chemistry* **96**, 6834-6839, doi:10.1021/j100195a056 (1992).

[45] Schaller, R. D. & Klimov, V. I. High Efficiency Carrier Multiplication in PbSe Nanocrystals: Implications for Solar Energy Conversion. *Physical Review Letters* **92**, 186601 (2004).

[46] Shalom, M., Dor, S., Rühle, S., Grinis, L. & Zaban, A. Core/CdS Quantum Dot/Shell Mesoporous Solar Cells with Improved Stability and Efficiency Using an Amorphous TiO2 Coating. *The Journal of Physical Chemistry C* **113**, 3895-3898, doi:10.1021/jp8108682 (2009).

[47] Mora-Seró, I. & Bisquert, J. Breakthroughs in the Development of Semiconductor-Sensitized Solar Cells. *The Journal of Physical Chemistry Letters* **1**, 3046-3052, doi:10.1021/jz100863b (2010).

[48] Chang, J. A. *et al.* High-Performance Nanostructured Inorganic−Organic Heterojunction Solar Cells. *Nano Letters* **10**, 2609-2612, doi:10.1021/nl101322h (2010).

[49] Chang, J. A. *et al.* Panchromatic Photon-Harvesting by Hole-Conducting Materials in Inorganic–Organic Heterojunction Sensitized-Solar Cell through the Formation of Nanostructured Electron Channels. *Nano Letters* **12**, 1863-1867, doi:10.1021/nl204224v (2012).

[50] Diguna, L. J., Shen, Q., Kobayashi, J. & Toyoda, T. High efficiency of CdSe quantum-dot-sensitized TiO[sub 2] inverse opal solar cells. *Applied Physics Letters* **91**, 023116-023113 (2007).

[51] Niitsoo, O. *et al.* Chemical bath deposited CdS/CdSe-sensitized porous TiO2 solar cells. *Journal of Photochemistry and Photobiology A: Chemistry* **181**, 306-313, doi:http://dx.doi.org/10.1016/j.jphotochem.2005.12.012 (2006).

[52] Lee, H. *et al.* Efficient CdSe Quantum Dot-Sensitized Solar Cells Prepared by an Improved Successive Ionic Layer Adsorption and Reaction Process. *Nano Letters* **9**, 4221-4227, doi:10.1021/nl902438d (2009).

[53] Lee, H. J., Bang, J., Park, J., Kim, S. & Park, S.-M. Multilayered Semiconductor (CdS/CdSe/ZnS)-Sensitized TiO2 Mesoporous Solar Cells: All Prepared by Successive Ionic Layer Adsorption and Reaction Processes. *Chemistry of Materials* **22**, 5636-5643, doi:10.1021/cm102024s (2010).

[54] O'Mahony, F. T. F., Lutz, T., Guijarro, N., Gomez, R. & Haque, S. A. Electron and hole transfer at metal oxide/Sb2S3/spiro-OMeTAD heterojunctions. *Energy & Environmental Science* **5**, 9760-9764, doi:10.1039/C2EE23037B (2012).

[55] Etgar, L. *et al.* Light Energy Conversion by Mesoscopic PbS Quantum Dots/TiO2 Heterojunction Solar Cells. *ACS Nano* **6**, 3092-3099, doi:10.1021/nn2048153 (2012).

[56] Pan, Z. *et al.* Highly Efficient Inverted Type-I CdS/CdSe Core/Shell Structure QD-Sensitized Solar Cells. *ACS Nano* **6**, 3982-3991, doi:10.1021/nn300278z (2012).

[57] Mora-Seró, I. n. *et al.* Recombination in Quantum Dot Sensitized Solar Cells. *Accounts of Chemical Research* **42**, 1848-1857, doi:10.1021/ar900134d (2009).

[58] Weller, H. Quantum Sized Semiconductor Particles in Solution and in Modified Layers. *Berichte der Bunsengesellschaft für physikalische Chemie* **95**, 1361-1365, doi:10.1002/bbpc.19910951108 (1991).

[59] Fang, J. H., Lu, X. M., Zhang, X. F., Fu, D. G. & Lu, Z. H. CdSe/TiO2 nanocrystalline solar cells. *Supramolecular Science* **5**, 709-711, doi:http://dx.doi.org/10.1016/S0968-5677(98)00109-6 (1998).

[60] Lee, H. *et al.* PbS and CdS Quantum Dot-Sensitized Solid-State Solar Cells: "Old Concepts, New Results". *Advanced Functional Materials* **19**, 2735-2742, doi:10.1002/adfm.200900081 (2009).

[61] Ip, A. H. *et al.* Hybrid passivated colloidal quantum dot solids. *Nat Nano* **7**, 577-582, doi:http://www.nature.com/nnano/journal/v7/n9/abs/nnano.2012.127.html#supplementary-information (2012).

[62] Moon, S.-J. *et al.* Sb2S3-Based Mesoscopic Solar Cell using an Organic Hole Conductor. *The Journal of Physical Chemistry Letters* **1**, 1524-1527, doi:10.1021/jz100308q (2010).

[63] Itzhaik, Y., Niitsoo, O., Page, M. & Hodes, G. Sb2S3-Sensitized Nanoporous TiO2 Solar Cells. *The Journal of Physical Chemistry C* **113**, 4254-4256, doi:10.1021/jp900302b (2009).

[64] Lee, M. M., Teuscher, J., Miyasaka, T., Murakami, T. N. & Snaith, H. J. Efficient Hybrid Solar Cells Based on Meso-Superstructured Organometal Halide Perovskites. *Science* **338**, 643-647, doi:10.1126/science.1228604 (2012).

[65] Kojima, A., Teshima, K., Shirai, Y. & Miyasaka, T. Organometal Halide Perovskites as Visible-Light Sensitizers for Photovoltaic Cells. *Journal of the American Chemical Society* **131**, 6050-6051, doi:10.1021/ja809598r (2009).

[66] Kim, H.-S. *et al.* Lead Iodide Perovskite Sensitized All-Solid-State Submicron Thin Film Mesoscopic Solar Cell with Efficiency Exceeding 9%. *Sci. Rep.* **2**, doi:http://www.nature.com/srep/2012/120821/srep00591/abs/srep00591.html#supplementary-information (2012).

[67] Burschka, J. *et al.* Sequential deposition as a route to high-performance perovskite-sensitized solar cells. *Nature* **499**, 316-319, doi:10.1038/nature12340

http://www.nature.com/nature/journal/v499/n7458/abs/nature12340.html#supplementary-information (2013).

[68] Bi, D. *et al.* Using two-step deposition technique to prepare perovskite (CH3NH3PbI3) for thin film solar cells based on ZrO2 and TiO2 mesostructures. *RSC Advances*, doi:10.1039/C3RA43228A (2013).

[69] Chung, I., Lee, B., He, J., Chang, R. P. H. & Kanatzidis, M. G. All-solid-state dye-sensitized solar cells with high efficiency. *Nature* **485**, 486-489, doi:http://www.nature.com/nature/journal/v485/n7399/abs/nature11067.html#supplementary-information (2012).

[70] Abrusci, A. *et al.* High-Performance Perovskite-Polymer Hybrid Solar Cells via Electronic Coupling with Fullerene Monolayers. *Nano Letters* **13**, 3124-3128, doi:10.1021/nl401044q (2013).

[71] Xu, X., Randorn, C., Efstathiou, P. & Irvine, J. T. S. A red metallic oxide photocatalyst. *Nat Mater* **11**, 595-598, doi:http://www.nature.com/nmat/journal/v11/n7/abs/nmat3312.html#supplementary-information (2012).

[72] Noh, J. H., Im, S. H., Heo, J. H., Mandal, T. N. & Seok, S. I. Chemical Management for Colorful, Efficient, and Stable Inorganic–Organic Hybrid Nanostructured Solar Cells. *Nano Letters* **13**, 1764-1769, doi:10.1021/nl400349b (2013).

[73] Ball, J. M., Lee, M. M., Hey, A. & Snaith, H. Low-Temperature Processed Mesosuperstructured to Thin-Film Perovskite Solar Cells. *Energy & Environmental Science* (2013).

[74] Eperon, G. E., Burlakov, V. M., Docampo, P., Goriely, A. & Snaith, H. J. Morphological Control for High Performance, Solution-Processed Planar Heterojunction Perovskite Solar Cells. *Advanced Functional Materials* **24**, 151-157, doi:10.1002/adfm.201302090 (2014).

[75] Liu, M., Johnston, M. B. & Snaith, H. J. Efficient planar heterojunction perovskite solar cells by vapour deposition. *Nature* **501**, 395-398, doi:10.1038/nature12509 (2013).

[76] Malinkiewicz, O. *et al.* Perovskite solar cells employing organic charge-transport layers. *Nat Photon* **8**, 128-132, doi:10.1038/nphoton.2013.341

http://www.nature.com/nphoton/journal/v8/n2/abs/nphoton.2013.341.html#supplementary-information (2014).

[77] (NREL), N. R. E. L. *NREL*, <www.nrel.gov/ncpv/images/efficiency_chart.jpg> (2014).

Chapter 3

Experimental Methods

3.1 Preparation of Solid-State Dye-Sensitized Solar Cells

The preparation of solid-state dye-sensitized solar cells was carried out in accordance with standard procedures,[1,2] and involved the following processes:

1. Chemical etching of the fluorine-doped tin oxide (FTO) substrates
2. Deposition of the TiO_2 compact layer
3. Deposition of the mesoporous TiO_2 layer
4. $TiCl_4$ chemical bath treatment
5. Dyeing
6. Spin coating the HTM
7. Thermal evaporation of electrodes

3.1.1 Chemical Etching of FTO Substrates

11.2 cm x 11.2 cm sheets of FTO-coated glass were used as received (7 Ω cm^{-1}, Pilkington glass). The required electrode pattern was obtained by masking off the desired areas of FTO with transparent adhesive tape. The unmasked areas were then selectively etched away using a combination of Zn powder and a 3 M solution of HCl. Subsequent to this, the substrate was rinsed with deionised (DI) water and the scotch tape removed. This was followed by vigorous scrubbing with Hellmanex (2 % solution in DI water) and rinsing with DI water. The substrate was then dried, and subjected to further rinsing in acetone then ethanol, after which it was dried again. After this final cleaning, the substrate was then subjected to oxygen plasma etching for 10 minutes. This final etching step serves to remove any organic residues which may remain on the substrate. A schematic of the electrode pattern used is given in **Figure 3.1**.

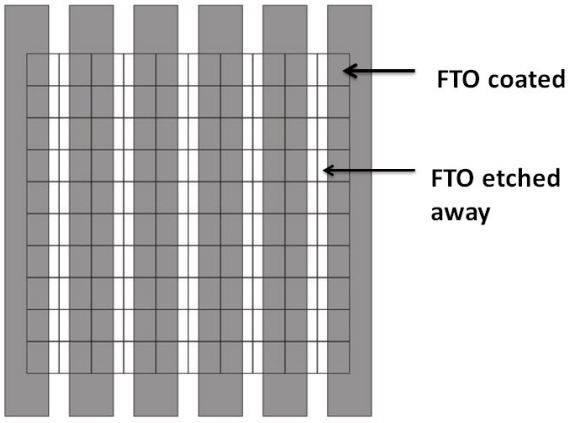

Figure 3.1: Electrode pattern used for etching FTO-coated substrates.

3.1.2 Deposition of the TiO_2 Compact Layer

The TiO_2 compact layers used in this thesis were deposited either by spray pyrolysis or by spin coating. The Ti precursor used for deposition via spray pyrolysis was titanium diisopropoxide bis(acetylacetonate), hereafter referred to as $Ti(acac)_2$. 5 ml Ti $(acac)_2$ (Sigma Aldrich, 75 %) was diluted in anhydrous ethanol in a 1:10 volume ratio. The substrate was then heated to 300 ˚C, and under O_2 flow, the precursor solution was manually sprayed onto it. After the spraying was completed, the substrate was heated for a further 30 minutes before being left to cool to room temperature under ambient conditions. The inclusion of this "hole-blocking" layer is essential to reducing recombination between the electrons in the FTO and holes in the HTM.[3]

For the deposition of the spin coated TiO_2 compact layer the Ti precursor used was titanium (IV) isopropoxide, hereafter referred to as Ti-iso. The precursor solution was formulated as follows:

- 1.25 ml of anhydrous ethanol was placed into each of 2 vials, A and B
- 17.5 µl of a 2M ethanolic solution of HCl was added to vial A
- 175 µl of Ti-iso was added to vial B
- The contents of vial A were added to B dropwise with vigorous stirring, resulting in a clear, colourless solution

After mixing the precursor solution, it was spin coated onto the substrate at 2000 rpm. For the low temperature processed compact layer, the substrate was then heated to 150 ˚C for 1 hour and for the high temperature processed compact layer, it was heated

to 500 ˚C for 45 minutes before being allowed to cool to room temperature naturally. The particular type of compact layer used is specified in each chapter.

3.1.3 Deposition of the Mesoporous TiO_2 layer

After the deposition of the compact layer, the TiO_2 mesoporous layer was deposited via doctor blading or spin coating depending on the desired thickness.

3.1.3.1 Commercial TiO_2 Paste

Commercially available TiO_2 paste (Dyesol 18NR-T) was used as a standard throughout this body of work. For doctor blading, the paste was diluted in ethanol in a 1:1.5 weight ratio. The resulting mixture was then agitated overnight using an automatic shaker until a homogeneous dispersion was obtained. The dispersion was then filtered through a 1 μm glass fibre filter in order to remove any large agglomerates. Following this, the paste was then deposited onto the compact layer coated substrate, using scotch tape to mask off areas which were not to be coated. The thickness of the resultant film was approximately 1 μm. The exact thicknesses used are quoted in each experiment.

For spin coating, the Dyesol paste was diluted in ethanol in a 1:3 weight ratio. As with the paste prepared for doctor blading, the mixture was agitated overnight and the dispersion obtained, filtered. The paste was then spin coated onto the compact layer substrates at a speed appropriate to yield the desired film thickness, which is quoted in each experimental chapter. After deposition of the TiO_2 paste, the substrates were then

sintered to 500 ˚C for 45 minutes, after which they were cooled to 80 ˚C before further processing.

3.1.3.2 In-house TiO_2 Paste

20 nm TiO_2 particles were synthesised according to the following method. 11.72 g of Ti-iso was added to 2.4 g of acetic acid at room temperature, and stirred vigorously for 15 minutes before adding 58 ml of DI water. The mixture was left stirring for a further 60 minutes. After stirring, 0.8 ml of HNO_3 was added dropwise, and the solution was stirred for an additional 2 hours. Subsequent to stirring, 75 ml of DI water was added, and the solution was transferred into an autoclave, and heated for 14 hours at 250 ˚C. After heating, the solution was allowed to cool to room temperature naturally and 0.48 ml of HNO_3 was added. The dispersion was then centrifuged at 7000 rpm and rinsed with water 3 times before being rinsed and subsequently dispersed in ethanol at a concentration of 100 mg/ml. In this case, the paste was doctor bladed onto the substrate to obtain a thickness of 1 μm, after which it was dried for 1 hour at 150 ˚C.

3.1.3.3 Mesoporous Single Crystal Paste

Mesoporous single crystals (MSCs) of TiO_2 were fabricated using literature methods.[4] Briefly, a close-packed sphere of 20 nm silica beads was synthesised, and seeded by immersion in a 1.5 x 10^{-2} M aqueous solution of titanium (IV) tetrachloride ($TiCl_4$) for 1 hour at 70˚C. The silica beads were subsequently sintered to 500 ˚C for 30 minutes. TiO_2 was then synthesised in the template from the hydrothermal reaction of a dilute solution of a titanium oxysulfate precursor at 100 ˚C. The silica beads were then removed from the product during a selective etching process, carried out in 2 M sodium

hydroxide (NaOH) at 80 ˚C for 1 hour, resulting in mesoporous TiO_2. The MSCs were then washed in water and ethanol and collected via centrifugation. The final product was dispersed in ethanol to form a dispersion which was 10% by mass.A binder-free paste was then formulated by adding 111 mg of terpineol per mL of MSC dispersion. Titanium diisopropoxide bisacetylacetonate, Ti $(acac)_2$ was then added to this dispersion in a 0.15 molar ratio (TiO_2/Ti$(acac)_2$). The paste was then deposited onto the substrate by spin-coating at various speeds to obtain the required film thicknesses, after which the substrate was heated to 150 ˚C for 1 hour.

3.1.4 $TiCl_4$ Surface Treatment

A stock solution of 2M $TiCl_4$ was diluted down with DI water to a concentration of 15 mM. The TiO_2 substrates were submerged in this solution and kept at 70 ˚C for 1 hour. After the completion of this incubation period the substrates were dried using compressed air, and then resintered to 500 ˚C for 45 minutes, after which they were left to be naturally cooled to 70 ˚C. This surface treatment has previously been found to improve the performance of ss-DSSCs, however the mechanism behind this improvement remains somewhat of a mystery. It has been proposed that it increases surface roughness, therefore increasing available surface area, and thus current generation. Another theory however, is that it somehow reduces the degree of recombination within the device. [5]

3.1.5 Dyeing

The dye used in the work presented in this thesis is the indoline dye termed D102. The chemical structure of this dye is shown in **Figure 3.2**. The dye solution was

prepared by mixing *tert*-butanol (Sigma Aldrich) and anhydrous acetonitrile (Sigma Aldrich) in a 1:1 volume ratio. To this solution the D102 powder was added such that 1 mg of dye was used per 20 ml of solvent. The dye solution was agitated on an automatic shaker until it was completely dissolved. The substrates which were kept at 70 ˚C were then immersed in the dye solution for 1 hour, immediately after being removed from the hotplate.

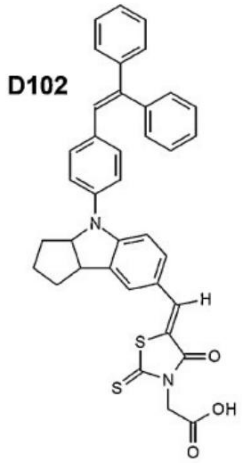

Figure 3.2: Chemical structure of the indolene dye termed D102.

3.1.6 Spin coating the HTM

Spiro-OMeTAD was used as obtained from Lum Tech or Borun Chemicals without any further purification. The spiro-OMeTAD was dissolved in chlorobenzene at 13 vol%, and then heated to 100˚C until it was completely dissolved. After complete dissolution, 4-tert-butyl pyridine (*t*BP) was added to the spiro-OMeTAD solution at a concentration of 80 mol. % with respect to the number of moles of spiro-OMeTAD in solution. Lithium bis(trifluoromethylsulfonyl)imide (Li-TFSI) was dissolved in acetonitrile at a concentration of 170 mgmL^{-1} to form a stock solution. This solution was then added to the and added to the hole transporter solution at 30 mol. % with

respect to the number of moles of spiro-OMeTAD. The dyed films were rinsed in acetonitrile and dried using a nitrogen gun. The HTM was then spin coated on the substrate at 1000 rpm for 45 seconds. The devices were then left overnight in the dark under ambient conditions before deposition of the metal electrodes. This step is to allow for complete oxidation of the HTM layer.

3.1.7 Thermal Evaporation of the Electrodes

Metal contacts were evaporated onto the completed devices using a thermal evaporator (Lesker Nano36). 200 nm thick silver electrodes or 50 nm thick gold electrodes were deposited under high vacuum (10^{-6} bar) through a shadow mask.

3.2 Preparation of Sb_2S_3-Sensitized Solar Cells

The steps taken to prepare Sb_2S_3 sensitized solar cells are very similar to those taken in the preparation of ss-DSSCs. Steps 1-4 are identical and have been described previously. In Chapter 5 of this thesis, the deposition of Sb_2S_3 is also done on an insulating alumina scaffold. The synthesis of this alumina paste and its deposition is described below.

3.2.1 Preparation of Mesoporous Alumina Scaffold

A 20 % by weight dispersion of 50 nm Al_2O_3 particles in ethanol was used as obtained from Alfa Aesar. 25.9 ml of this dispersion was added dropwise with stirring to 55.6 ml of butoxyethanol (Sigma Aldrich). The water in the solution was then evaporated using a rotary evaporator. When the dry mixture was obtained, it was diluted by ethanol in a 2:1 ratio of Al_2O_3 to ethanol.

A solution of hydroxypropyl cellulose was prepared by adding 2 g of cellulose (Sigma Aldrich) to 25.35 ml of ethanol with vigorous stirring. The alumina mixture was then added slowly with stirring. When a homogenous mixture was obtained, excess ethanol was removed using rotary evaporation, resulting in the paste beginning to gel. This paste was then diluted with ethanol until the appropriate consistency was achieved. The paste was then doctor bladed onto a compact layer coated substrate, such that a thickness of 1 μm was obtained. As in the case of the TiO_2 paste, the substrate was then calcined at 500 ˚C for 45 minutes to ensure the removal of the organic binders, as well as to facilitate inter-particle necking.

3.2.2 Chemical Bath Deposition of Sb_2S_3

The chemical bath used for the deposition of Sb_2S_3 was done in accordance with literature procedures.[6,7] Briefly 0.625 g of $SbCl_3$ was dissolved in 2.5 ml of acetone. 25 ml of a 1 M $Na_2S_2O_3$ was added slowly with stirring, resulting in a clear, colourless solution.

The volume of the solution was then made up to 100 ml with cold DI water. The substrates were then immersed in the bath, which was kept at 10 ˚C for the desired incubation time. Specific times are noted in Chapter 5. The substrates were then rinsed in DI water and dried with a nitrogen gun. They were then heated to 300 ˚C under nitrogen atmosphere for 30 minutes. This step is necessary for the conversion of the as-deposited, amorphous Sb_2S_3 to the crystalline, semiconducting form.

3.2.3 Deposition of the HTM and Thermal Evaporation

In the case of the Sb_2S_3 solar cells fabricated for this thesis, the HTM of choice was regioregular poly (3-hexylthiophene), hereafter known as P3HT. This polymer was used as obtained from Rieke Metals Inc. without further purification. The polymer was dissolved in chlorobenzene at a concentration of 20 mg per mL, and heated to 100 ˚C until it was completely dissolved. The solution was then spin coated on top of the Sb_2S_3 substrates at 2000 rpm for 45 seconds, after which it was annealed in ambient atmosphere for 10 minutes. Thermal evaporation took place as described in Section 3.1.7 and was used for the deposition of 50 nm thick gold electrodes.

3.3 Fabrication of Planar Heterojunction Perovskite Solar Cells

The fabrication of planar heterojunction perovskite solar cells was carried out according to literature methods.[8] Steps 1 and 2 were carried out as outlined in Sections 3.11

and 3.1.2. The synthesis of the perovskite precursor solution was carried out according to literature methods.[9] The $CH_3NH_3PbI_{3-x}Cl_x$ precursor solution (40 wt % in DMF, 3:1 molar ratio of methylammonium iodide to lead chloride) was spin coated onto the compact layer substrates at 2000 rpm in a nitrogen-filled glove box. The substrates were then left to dry under nitrogen for 30 minutes. They were then heated to 90 ˚C for 2.5 hours in order to complete the perovskite crystallisation. After crystallisation, an 8.5 weight % solution of spiro-OMeTAD (30 mol % Li-TFSI and 80 mol % *t*BP as additives) was spin coated onto the perovskite substrates at 2000 rpm. The devices were then taken out of the glove box and stored in a desiccator overnight before the thermal evaporation of 50 nm gold electrodes.

3.4 Fabrication of Lead-Free Perovskite-Sensitized Solar Cells

Steps 1, 2 and 3 were carried out as outlined in Sections 3.1.1, 3.1.2 and 3.1.3. In this specific case, a 400 nm thick layer of mesoporous TiO_2 (Dyesol 18NR-T) was deposited via spincoating a 3:1 dilution of paste in ethanol, at 2000 rpm for 1 minute. The substrate was then sintered to 500 ˚C for 45 minutes before being allowed to naturally cool down to room temperature. The $CH_3NH_3SnI_3$ precursor solution was made under inert atmosphere by dissolving equimolar quantities of methylammonium iodide (MAI) and SnI_2 in N, N-dimethylformamide (DMF) at a concentration of 40 wt %. After the substrates were allowed to cool, they were transferred into a nitrogen filled glove box. The perovskite precursor solution was then deposited onto the substrates via spin coating at 2000 rpm, and the perovskite crystallised upon spin coating. After formation of the perovskite layer, the HTM, spiro-OMeTAD, was dissolved in (concentration 80 mM) with addition of additives at a concentration of 10 mM hydrogen bis (trifluoromethanesulfonyl) imide, (H-TFSI), and

80 mM tert-butylpyridine (tBP).[10] 50 nm thick gold electrodes were then evaporated using a thermal evaporator within the glove box. After evaporation the cells were sealed under inert atmosphere using a meltable polymer and an epoxy resin.

3.5 Fabrication of Spectroscopy Samples

A sheet of glass was cut into 2.8 cm x 2.8 cm squares. These samples were vigorous scrubbed with Hellmanex (2 % solution in DI water) and then rinsed with DI water. The substrate was then dried, and subjected to further rinsing in acetone then ethanol, after which it was dried again. Subsequent to this final cleaning, the substrate was then subjected to oxygen plasma etching for 10 minutes, after which it was immediately transferred into a nitrogen filled glovebox. The $CH_3NH_3PbI_{3-x}Cl_x$ perovskite precursor was then spin coated and annealed in the same fashion as for the planar heterojunction solar cells. After annealing, a 1% solution of polymethyl methacrylate (PMMA) in chlorobenzene was spin coated on top of the samples to slow degradation. The spectroscopy samples for the $CH_3NH_3SnI_3$ perovskite were fabricated in the same manner, but were sealed in nitrogen atmosphere using a meltable polymer and an epoxy resin before being brought out into ambient conditions.

3.5 Electrical Characterization

3.5.1 Solar Cell Characterization

Solar cell performance parameters were measured under simulated AM 1.5 illumination provided by an ABET solar simulator. The solar simulator irradiance was calibrated using a KG5 filtered Si reference cell (NREL) to yield 100 $mWcm^{-2}$ output. A sourcemeter (Keithley 2400, USA) was used to record the current-voltage characteristics. All solar cells were masked with a metal aperture which was used to define the active area of the devices, which in this case was 0.0625 cm^2. This masking is essential to eliminating any possible edge effects which may contribute to the measured current densities. [11]

3.5.2 Transient Photocurrent and Photovoltage Decays

Performing transient photocurrent and photovoltage decay measurements allows for the extraction of the charge transport and recombination lifetimes in an SSC. These parameters are very helpful in determining which factors may or may not be limiting the efficiency of a particular photovoltaic system. In this experiment, originally introduced by O'Regan and co-workers,[12] a properly functioning device is held at steady state conditions under white light, background illumination. In the case of the TiO_2-based solar cells, this background illumination results in the occupation of a certain proportion of the sub-band

gap trap states which were discussed in Chapter 2. The cell is then subjected to a short pulse of light, which in this case is provided by a red LED, and the response (time taken to decay back to steady state) can be recorded using an oscilloscope. This measurement is often repeated at different intensities of background illumination which correspond to different charge densities within the solar cell. **Figure 3.3** shows a schematic of a typical photovoltage decay curve.

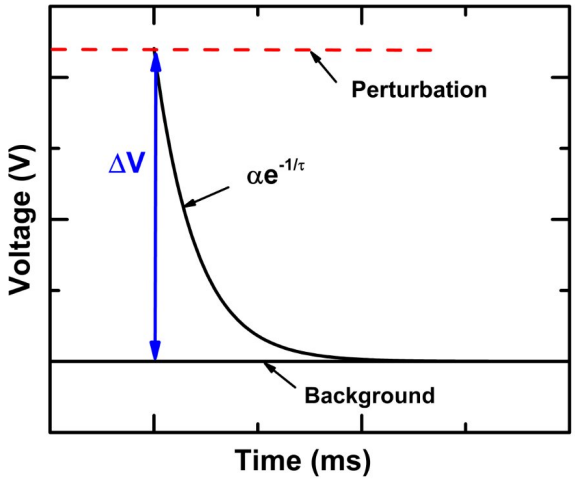

Figure 3.3: Schematic of a typical photovoltage decay curve obtained using the transient photovoltage technique.

These measurements can be performed under two distinct conditions; fixed current or fixed potential. Under fixed current conditions, otherwise known as galvanostatic mode, the current flowing through the device is kept constant via a sourcemeter. When the device is exposed to a pulse of light from the LED, the extra current cannot be extracted, and as such, the response which is measured by the oscilloscope is due solely to the recombination kinetics occurring within the device. Fitting the device response to an exponential gives the recombination lifetime of the device (τ_{rec}). Under fixed potential conditions, otherwise known as potentiostatic mode, the device is held under short circuit conditions and is

subjected to a small light perturbation. The response of the device is then recorded on an oscilloscope, and similarly to the measurement taken under fixed current conditions, the decay is fit to an exponential function, from which a lifetime can be extracted (τ_{meas}).In potentiostatic mode however, because current can be extracted from the device, the lifetime obtained from fitting the decay curve will involve both transport and recombination characteristics. In order to disentangle the two and obtain only the charge transport lifetime, the relation given in **Equation 3.2** must be used.

$$\frac{1}{\tau_{meas}} = \frac{1}{\tau_{trans}} + \frac{1}{\tau_{rec}} \tag{3.1}$$

$$\tau_{trans} = \frac{1}{\left(\frac{1}{\tau_{meas}} - \frac{1}{\tau_{rec}}\right)} \tag{3.2}$$

From these measurements the charge collection efficiency of solar cells can also be estimated. This estimation has been proven to be valid only for efficiencies of ≥ 70 % and is given by the following equation:

$$\eta_c = \frac{{}^{1}/_{\tau_{trans}}}{\frac{1}{\tau_{meas}} + \frac{1}{\tau_{rec}}} \tag{3.3}$$

If the cell is held under open circuit conditions, this measurement can give information about the density of states (DOS) of the mesoporous TiO_2 layer. This technique utilizes the same type of light perturbation while holding the solar cell at open circuit. In this case, the light pulse creates a voltage perturbation (ΔV) which is recorded by the oscilloscope. Immediately after, under the same conditions, the device is short-circuited and the current extracted can be integrated in order to yield an estimate of the amount of

charge which is generated by the pulse (ΔQ). From these values, the capacitance of the system can be determined.

$$C = \frac{\Delta Q}{\Delta V} \tag{3.4}$$

3.6 Spectroscopy

3.6.1 Absorption Spectroscopy

UV-Vis-NIR absorption spectroscopy is a very useful tool or probing the optical propertied of materials, either in dilute solutions, or as in the case of this thesis, thin solid films. This measurement is governed by the Beer-Lambert law, which relates the absorbance, or optical density of a solution or film, to the transmission of light through the sample, the path length that the light travels, and to an absorption or molar extinction coefficient.[13] This relationship is given below in **Equation 3.5**.

$$A = -log_{10}\left(\frac{I}{I_0}\right) = \frac{\alpha l}{ln10} = \varepsilon c l \tag{3.5}$$

where A is absorbance, I is the transmitted light intensity, I_0 is the incident light intensity, α is the absorption coefficient, l is the path length, c the concentration of a dilute solution and ε is the molar extinction coefficient. The absorbance of a material is dependent on the wavelength being investigated and as such these measurements are taken across a range of different wavelengths.

3.6.2 Steady-State and Time-Resolved Photoluminescence Spectroscopy

Steady-state photoluminescence (PL) measurements involve the photoexcitation of a species with a wavelength of light (usually in the visible region), after which there is a relaxation to the band edge and subsequent emission of light. For the mixed halide, lead-based perovskite $CH_3NH_3PbI_{3-x}Cl_x$, the perovskite is excited at a wavelength of 510 nm, pulsed at a frequency of 10 MHz, and emission is observed at 780 nm. For both steady state and time-resolved PL measurements a time-correlated single photon counting (TCSPC) setup (FluoTime 300, PicoQuant GmbH) was used. A diagram of the setup is shown in **Figure 3.4**.

The laser fires a pulse which is attenuated by a neutral density filter. This attenuated pulse is then used to excite the sample. The cut-off filter is then used to filter out any light which is scattered by the sample. The attenuator then allows a single photon emitted by the sample to pass through. This single photon then hits the photomultiplier tube (PMT) and thus creates a short electron pulse. The timing electronics can then record the time at which the signal id received. These signals are summed up over many repetitions, at many laser pulses, thus creating a photoluminescence histogram which depicts the decay of the photoluminescence with time.

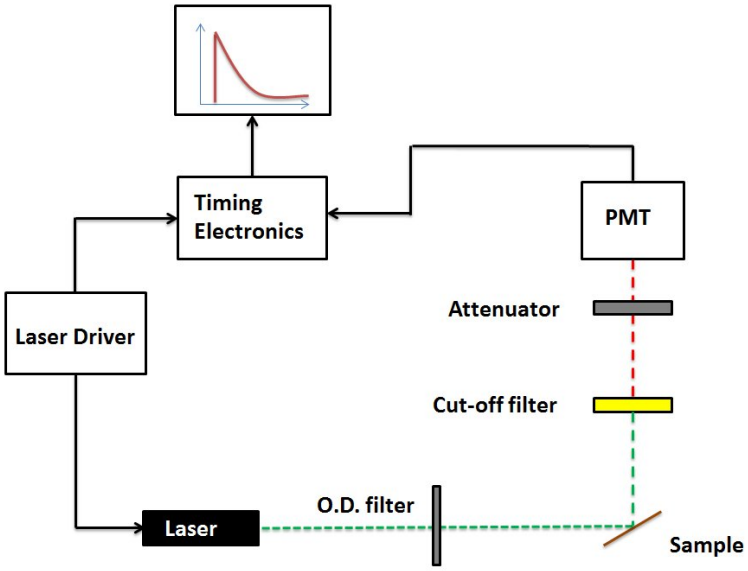

Figure 3.4: Schematic of the FluoTime 300, PicoQuant GmbH setup which was used for recording steady state and time-resolved photoluminescence spectra.

3.6.3 Photoluminescence Quantum Efficiency

The radiative quantum efficiency of a material is given by the following relation:

$$\eta = \frac{\#\ of\ photons\ emitted}{\#\ of\ photons\ absorbed} \tag{3.6}$$

The photoluminescence quantum efficiency (PLQE) of perovskite samples were measured using an integrating sphere to isotropically redistribute light emitted from the sample.

These measurements were done as described by Friend and co-workers.[14] The samples were excited using a 532 nm diode laser through a small hole in the integrating sphere. These measurements were done in triplicate; with the laser illuminating an empty sphere, once when it is incident on the sample, and one where the sample is in the sphere, but not being directly hit by the laser beam. Additionally, a measurement of the background (with the laser beam off) was taken. These measurements result in peaks at both the wavelength of the laser and the wavelength of the emission. By integrating the area under these respective peaks the PLQE of the samples can be determined.

3.6.4 Photo-thermal Deflection Spectroscopy

$CH_3NH_3SnI_3$ perovskite samples for photo-thermal deflection spectroscopy (PDS) were prepared identically to those described in Section 3.5, except that they were made on quartz substrates. A full description of the experimental setup and conditions is given by Kronemeijer *et al.*[15] PDS is a very delicate spectroscopic technique which is capable of detecting subtle absorptions in the band gap. In this measurement, the sample is immersed in an inert liquid, most usually Fluorinert FC-72 (3M Co.) and photoexcited using monochromated light. Heat is then produced in the surrounding medium as a result of non-radiative relaxation processes within the material. This causes a change in the refractive index of the inert liquid, which can then be correlated to the light absorbed in the sample.

3.6.5 Terahertz Time-Domain Spectroscopy

In Chapter 7, time-resolved pump-probe terahertz (THz) spectroscopy is used to investigate the photophysical characteristics of films of $CH_3NH_3SnI_3$ perovskite. This measurement, which takes place in vacuum, provides a contact-free way of probing the conductivity of films at a resolution of picoseconds. This has proven to be quite important for films of tin perovskite as they rapidly degrade in ambient conditions. In this measurement, a 40 fs laser pulse is used to photoexcite the sample at a wavelength of 550 nm, and a repetition rate of 1.1 KHz. After a given time delay, a single THz pulse is used to excite the sample. The transient conductivity of the sample can then be extracted by modelling the photoinduced change in the THz transmission. These measurements have also been used to extract the charge carrier mobility. Details of the model are given Chapter 7.

3.8 Scanning Electron Microscopy

Scanning electron microscopy (SEM) was performed using a Hitachi S-4300 system. This technique was used to capture images of microstructured and nanostructured materials. Where cross-sectional device images were required, the device was scored using a diamond scribe, in order to efficiently cleave it into 2 parts. SEM images could then be obtained at the ends of the score marks. 3 nm of platinum was sputter-coated onto all samples before imaging, in order to reduce charge accumulation under the electron beam.

3.9 References

[1] Bach, U. *et al.* Solid-state dye-sensitized mesoporous TiO2 solar cells with high photon-to-electron conversion efficiencies. *Nature* **395**, 583-585 (1998).

[2] Docampo, P. *et al.* Pore Filling of Spiro-OMeTAD in Solid-State Dye-Sensitized Solar Cells Determined Via Optical Reflectometry. *Advanced Functional Materials* **22**, 5010-5019, doi:10.1002/adfm.201201223 (2012).

[3] Snaith, H. J. & Grätzel, M. Electron and Hole Transport through Mesoporous TiO2 Infiltrated with Spiro-MeOTAD. *Advanced Materials* **19**, 3643-3647, doi:10.1002/adma.200602085 (2007).

[4] Crossland, E. J. W. *et al.* Mesoporous TiO2 single crystals delivering enhanced mobility and optoelectronic device performance. *Nature* **495**, 215-219, doi:http://www.nature.com/nature/journal/v495/n7440/abs/nature11936.html#supplementary-information (2013).

[5] O'Regan, B. C., Durrant, J. R., Sommeling, P. M. & Bakker, N. J. Influence of the TiCl4 Treatment on Nanocrystalline TiO2 Films in Dye-Sensitized Solar Cells. 2. Charge Density, Band Edge Shifts, and Quantification of Recombination Losses at Short Circuit. *The Journal of Physical Chemistry C* **111**, 14001-14010, doi:10.1021/jp073056p (2007).

[6] Messina, S., Nair, M. T. S. & Nair, P. K. Antimony sulfide thin films in chemically deposited thin film photovoltaic cells. *Thin Solid Films* **515**, 5777-5782, doi:http://dx.doi.org/10.1016/j.tsf.2006.12.155 (2007).

[7] Chang, J. A. *et al.* High-Performance Nanostructured Inorganic−Organic Heterojunction Solar Cells. *Nano Letters* **10**, 2609-2612, doi:10.1021/nl101322h (2010).

[8] Eperon, G. E., Burlakov, V. M., Docampo, P., Goriely, A. & Snaith, H. J. Morphological Control for High Performance, Solution-Processed Planar Heterojunction Perovskite Solar Cells. *Advanced Functional Materials* **24**, 151-157, doi:10.1002/adfm.201302090 (2014).

[9] Lee, M. M., Teuscher, J., Miyasaka, T., Murakami, T. N. & Snaith, H. J. Efficient Hybrid Solar Cells Based on Meso-Superstructured Organometal Halide Perovskites. *Science* **338**, 643-647, doi:10.1126/science.1228604 (2012).

[10] Abate, A. *et al.* Protic Ionic Liquids as p-Dopant for Organic Hole Transporting Materials and Their Application in High Efficiency Hybrid Solar Cells. *Journal of the American Chemical Society* **135**, 13538-13548, doi:10.1021/ja406230f (2013).

[11] Snaith, H. J. How should you measure your excitonic solar cells? *Energy & Environmental Science* **5**, 6513-6520, doi:10.1039/C2EE03429H (2012).

[12] O'Regan, B. C.; Bakker, K.; Kroeze, J.; Smit, H.; Sommeling, P.; Durrant, J. R. Measuring Charge Transport from Transient Photovoltage Rise Times. A New Tool To Investigate Electron Transport in Nanoparticle Films. The Journal of Physical Chemistry B 2006, 110, 17155-17160

[13] Fox, M. *Optical Properties of Solids*. (OUP Oxford, 2010).

[14] de Mello, J. C., Wittmann, H. F. & Friend, R. H. An improved experimental determination of external photoluminescence quantum efficiency. *Advanced Materials* **9**, 230-232, doi:10.1002/adma.19970090308 (1997).

[15] Kronemeijer, A. J. *et al.* Two-Dimensional Carrier Distribution in Top-Gate Polymer Field-Effect Transistors: Correlation between Width of Density of Localized States and Urbach Energy. *Advanced Materials* **26**, 728-733, doi:10.1002/adma.201303060 (2014).

Chapter 3: References

Chapter 4

Mesoporous Single Crystals: A Facile Route to Reduced Electronic Disorder and Efficient, Low Temperature Processed Dye-Sensitized Solar Cells

The results presented in this chapter have been reported in:

1) Crossland, E. J. W.; Noel, N.; Sivaram, V.; Leijtens, T.; Alexander-Webber, J. A.; Snaith, H. J. Mesoporous TiO_2 single crystals delivering enhanced mobility and optoelectronic device performance. Nature 2013, 495, (7440), 215-219.

2) Noel, N.K.; Crossland, E.J.W.; Leijtens, T.; Nunzi, F.; Sivaram, V.; De Angelis, F.; Snaith, H.J. Mesoporous Single Crystals: A Facile Route to Reduced Electronic Disorder and Efficient, Low Temperature Processed Dye-Sensitized Solar Cells. Submitted to Advanced Energy Materials, 2014.

4.1 Broad Context

In a standard ss-DSSC, the mesoporous layer consists of TiO_2 nanoparticles which have been sintered together to form a sponge-like network. However, there are distinct disadvantages to utilising this method, one of which is that it introduces electronic disorder within the layer, mainly at the many grain boundaries in the film.[1] The cause of this broad electronic disorder is likely due to deviations from stoichiometry, which would then present itself as trap states within the material. Charge transport in DSSCs can be described by a multiple trapping (MT) model,[2-4] and as such, the density of trap states within the mesoporous layer greatly affects charge transport within the device.

The rate of charge transport in DSSCs has been shown to be limited by the electron transport rate within TiO_2.[5,6] As a result of this, much research has gone into improving the electrode architecture in these devices. One of the most popular avenues investigated has been 1D architectures such as nanowires and nanotubes which appear to exhibit faster charge transport rates. However, this is at the expense of having a large surface area available for dye adsorption. It follows then, that the perfect electrode architecture would be such that it is able to combine the high surface area of a nanoparticulate layer, with the fast transport of single crystalline structures. In this chapter, I present the development of mesoporous single crystals (MSCs) of TiO_2, single crystalline structures with intrinsic porosity. These MSCs exhibit superior electronic properties, and interestingly negate the need for sintering, resulting in the fabrication of completely low-temperature processed ss-DSSCs which rival the performance of their high-temperature processed, nanoparticle counterparts.

4.2 Introduction

Dye-sensitised solar cells (DSSC) are considered to be a promising alternative to conventional silicon-based photovoltaics. The initial, ground breaking report of a 7% efficient liquid electrolyte DSSC, by Gratzel and O'Regan in 1991, generated significant research effort towards creating low cost efficient solar cells.[7] Since then, the efficiencies of these devices have been rising steadily, to the current record efficiency of 13%.[8] While the DSSC is not yet as efficient as competing thin film technologies such as CIGS and CdTe, it has the advantage of having a cheaper manufacturing process, devoid of more costly vacuum deposition techniques and annealing at very high temperatures (>500˚C). It also has extensive tunability with respect to colour and transparency, making it an ideal system for building integrated photovoltaics (BIPV). However, two factors have coincided, bringing the prospects for DSSCs into question; i) the continued drop in the prices of silicon PV necessitates a highly efficient solar technology to compete in the largest market of ground mount utility PV, and ii) the recent realisation of extremely efficient solar cells based on organic inorganic metal halide perovskite absorbers, which have rapidly surpassed the DSSCs and other emerging PV concepts in performance.[9-12] Not only do these perovskite devices have the advantage of the active component costing practically nothing, but they are also fully solid-state, which should enable much more facile scale up to production. An additional advantage is that they can now be processed at low temperatures.[10,13,14]

In their favour however, DSSCs, alongside organic PV offer the widest range of color,[15-18] and can specifically deliver green and blue semi-transparent solar cells. This is a desired product for building integrated photovoltaics (BIPV) and as yet, cannot be delivered by perovskite or other thin film solar technologies. Notably, for BIPV and semi-transparent applications the films must be non-scattering; otherwise the main unique selling point of clarity is lost. Additionally, applications where form factor is

important, such as flexible, lightweight solar cells, DSSCs could be ideal, opening up previously inaccessible markets such as power supplies for portable electronic devices and indoor power applications. However, processing on many flexible substrates, such as plastic foil and a broad range of metal substrates without deformation, requires reduction of the processing temperature to between 100 to 250 °C depending on substrate (current processing of the highest efficiency DSSCs occurs at 500 °C).[19-22]

With respect to efficiency, the efficiency of DSSCs has only increased marginally over the last ten years. This has been due to fundamental losses in what is considered the most common embodiment; mesoporous TiO_2, ruthenium complex dye sensitizer and the iodide/triiodide redox electrolyte. Voltage losses exist primarily due to the high level of electronic disorder in the TiO_2, and also to the over-potential required between the electrolyte redox couple and the dye ground state to regenerate the dye.[7] A switch to a cobalt based single electron outer sphere redox couple has reduced the over potential required and increased the efficiency,[8] but poses an even greater challenge for solidification due to the necessity for long range diffusion of bulky redox molecules.

Moving to a solid-state hole-conductor, such spiro-OMeTAD, should equally enhance the open-circuit voltage; however, currently solid-state DSSCs are uncompetitive for a number of reasons which also require addressing.[1] Voltage losses could be reduced further by either improving the dye or the mesoporous TiO_2. Dyes which sustain extremely long lived photoexcited states would enable the conduction band of the TiO_2 to be shifted to much lower levels (closer to vacuum), whilst still enabling the photo-excited dye to transfer electrons into the low density tail of the conduction band states. This is probably one reason why porphyrin sensitizers can deliver higher open-circuit voltages than other organic dyes when incorporated into

DSSCs.[8,23-25] Concerning the mesoporous TiO_2, a high level of electronic disorder in the TiO_2 reduces the maximum attainable open circuit voltage under any given light intensity, unless these defect sites can become completely filled with electrons. The open-circuit voltage is set by the splitting of the quasi Fermi level for electrons (E_{Fn}^*) in the TiO_2 and holes in the redox couple or hole-transporter (E_{Fp}^*). The larger the density of sub band gap states, the further from the conduction band E_{Fn}^* will remain for any given electron concentration. Hence, any fundamentally highly efficient solar cell requires the absorber region to be highly crystalline, and as such, possess an extremely low level of electronic disorder. Interestingly, if the mesoporous TiO_2 could be effectively n-type doped in a controlled manner, and the ensuing recombination of electrons with holes in the hole-transporter suppressed, then again an effectively reduced electronic disorder and much increased voltages could be obtained. Here we focus our attention on the mesoporous TiO_2 photoanode, with the aim of both reducing the processing temperature, as well as the degree of electronic disorder.

Mesoporous semiconductors are at the heart of many low cost energy solutions,[26] and while mesoporosity provides the large surface area needed for many applications, sintered nanoparticle films do not lend the structural coherence and long-range electronic connectivity which may be required.[27] As previously discussed in Chapter 2, electron mobilities in single crystalline TiO_2 have been shown to be orders of magnitude higher than those obtained from nanoparticle films. In this chapter, I present the synthesis of mesoporous single crystals (MSCs) of TiO_2 and their use in low temperature processed DSSCs. MSCs are an interesting class of material as they combine the high surface area of a nanoparticle system with large crystalline domains (150 nm- 1μm), endowing greatly increased electron mobility and higher conductivities than their nanoparticulate counterpart.[28] This makes this material a prime candidate for incorporation into a low temperature DSSC. The intrinsic porosity of the MSC obviates the need for the incorporation of a polymer binder to increase available surface area,

while its superior electronic properties allude to the redundancy of high temperature sintering, as effective electronic contact already exists within a film of the material. Here, I demonstrate a general method for the fabrication of all low temperature solid-state DSSCs, and by reducing the MSC domain size, obtain non-scattering "transparent" films.Upon probing the electronic properties of these devices, we show a reduced density of sub band gap states, very close to what is expected for a perfect single crystal, and enhanced charge transport rates through the MSC films.

.

4.3 Synthesis of MSCs

Figure 4.1 shows a schematic of the synthesis of micron sized MSCs of anatase TiO_2 along with SEM images of synthesised crystals. Depending on the desired pore size of the MSCs, appropriately sized silica beads were selected for the template. The pore size of the MSCs presented in this chapter is 20 nm. A close packed template was formed by sintering the silica beads together in an oven at 500 ˚C. This template was then placed in a 15 mM aqueous solution of $TiCl_4$ for 1 hour at 70 ˚C. The template was then rinsed in DI water.

For the synthesis of crystals with a large domain size (1μm), a titanium tetrafluoride (TiF_4) precursor was used. TiF_4 was dissolved in acidic DI water (pH 2.1) at a concentration of 120 mM and 180 mM of the ionic liquid 1-methylimidazolium tetra-fluoroborate was added. 650 mg of the pre-seeded silica template was placed into a Teflon-lined autoclave, and 50 ml of the TiF_4 solution was added. The autoclave was then placed in an oven at 120 ˚C for 12 hours before being left to cool to room temperature naturally. For smaller crystals (150 nm- 300 nm) a titanium oxysulfate ($TiO(SO_4)$) precursor was used. The same procedure was used, where the ($TiO(SO_4)$)

was dissolved at a concentration of 100 mM, and the hydrothermal growth was done at 100 ˚C for a 12 hour period. After the autoclaves were cooled to room temperature, the product was collected and sintered to 500 ˚C. After sintering, the powder was placed into a 2M solution of NaOH and stirred vigorously with heating (80 ˚C) for 2 hours. This process caused the selective etching away of the silica template, resulting in intrinsically porous TiO_2 crystals. The MSCs were then collected by centrifugation and rinsed with water and ethanol, and finally redispersed in ethanol at a concentration of 10 weight %.

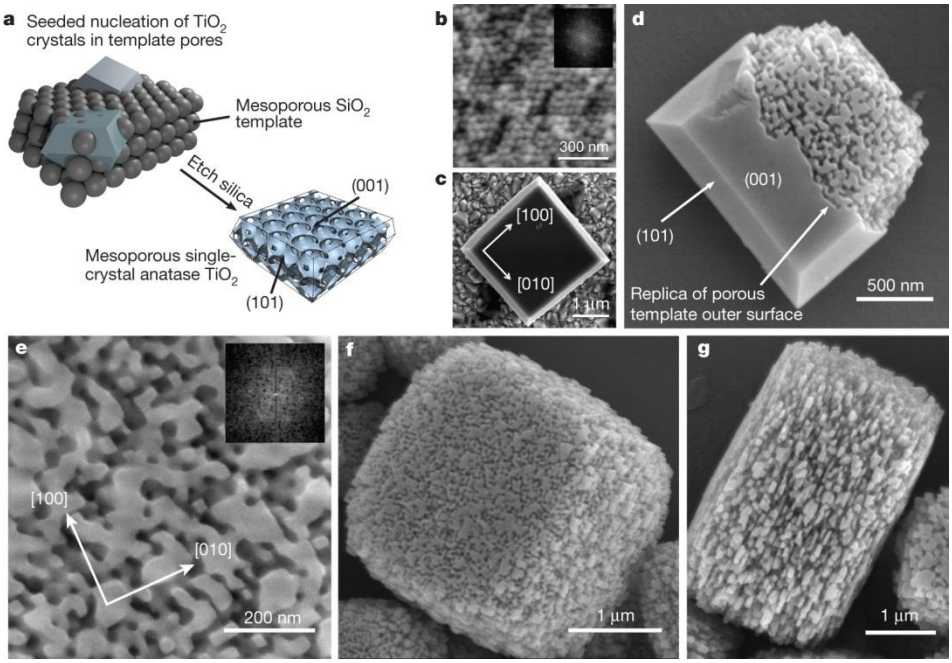

Figure 4.1: (a) Schematic of the nucleation and growth of TiO_2 single crystals, followed by selective etching of the silica template to give a mesoporous single crystal (MSC). (b) SEM image of close packed silica template, fast fourier transform (FFT) is shown in the inset. (c) SEM image of a non-porous single crystal of TiO_2. (d) SEM image of a partially porous TiO_2 single crystal. (e) Close up image of the pore structure of and MSC. (f) and (g) Close up SEM images of completely mesoporous TiO_2 crystals. MSC synthesis and figure done by Dr. Edward J.W. Crossland of the Department of Physics, University of Oxford.

4.4 Electrical Characterization

One of the simplest ways to test whether or not MSCs do indeed possess superior electronic properties as compared to nanoparticles is to investigate the conductivity and electron mobilities of these particles. In order to determine the conductivity of a single crystal, two probe conductivity measurements were taken. Here, micron sized MSCs were dropped across gold electrodes and using a two probe contact the conductivity of a single MSC was measured. The conductivity of a single MSC which had not been through the 500 ˚C sintering step before etching was found to be 4.9 x 10^{-6} Scm^{-1}. For MSCs which had been through the 500 ˚C sintering step however, the conductivity was found to increase by an order of magnitude to 1.5 x 10^{-5} Scm^{-1}. This measurement was also done on films of unsintered and sintered TiO_2 nanoparticles and a similar increase in conductivity occurred after the nanoparticles had been sintered, from 8.4 x 10^{-9} Scm^{-1} to 2.2 x 10^{-7} Scm^{-1}. The mobility of dyed films of both MSCs and nanoparticles can also be extracted using a technique called Transient Mobility Spectroscopy (TMS).[5] This technique combines transient absorption spectroscopy with photoconductivity measurements, allowing for the simultaneous investigation of the charge carrier density in the film, as well as the conductivity. From this, the mobility of the film can then be extracted. **Figure 4.2** shows the mobility of sintered MSC and nanoparticle films as a function of photoinduced charge density. It can be seen here that for any given charge density, the mobility of MSC films is over an order of magnitude higher than that of the nanoparticle films. The increased conductivity and mobility of MSCs as compared to nanoparticle films is indicative of the fact that these MSCs do indeed possess superior electronic properties.

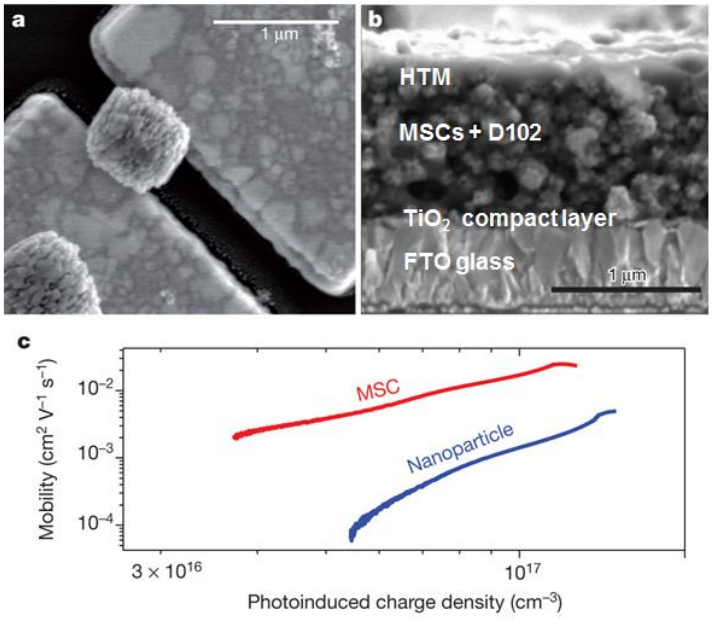

Figure 4.2: (a) SEM image of a single MSC spanning 2 gold electrodes on a substrate used for conductivity measurements. (b) Cross-sectional SEM image of an ss-DSSC fabricated using MSCs of TiO_2. (c) Mobility of MSC and nanoparticle films as a function of photoinduced charge density. Conductivity measurements were taken by Dr. Jack Alexander-Webber and mobility measurements were taken by Tomas Leijtens, both of the Department of Physics, University of Oxford.

4.5 Device Fabrication

Having confirmed that MSCs do indeed have superior electronic properties to nanoparticle films, their performance in ss-DSSCs can now be investigated. Devices were fabricated as discussed in Chapter 3; however, due to the large size of MSCs, depositing a smooth layer was very difficult. **Figures 4.5** and **4.6** shows a top view of a

doctor bladed layer of micron sized MSCs and cross-sectional views of devices fabricated with increasing concentrations of spiro-OMeTAD, respectively.

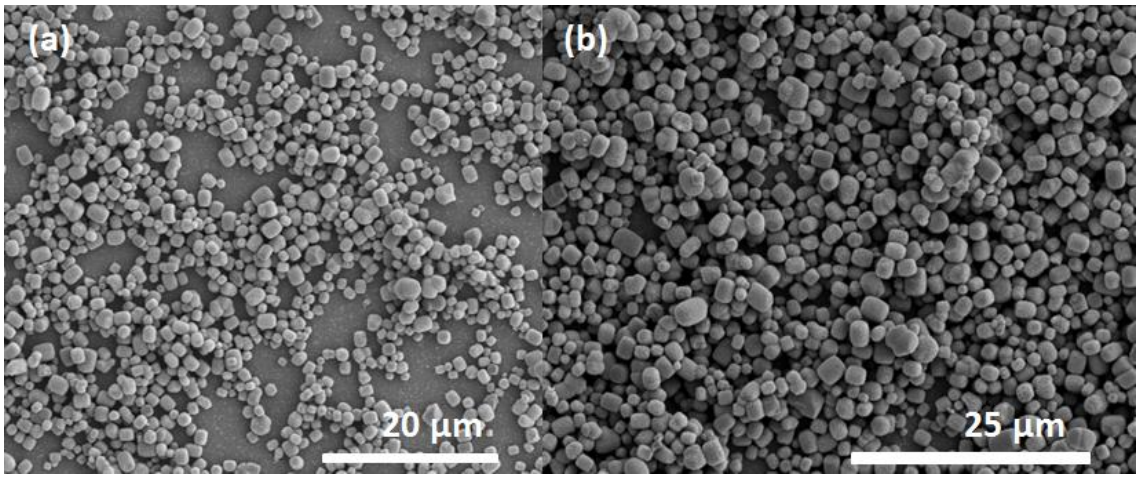

Figure 4.5: (a) and (b) Top view SEM images of doctor bladed films of MSCs.

It can be seen from Figures 4.5 (a) and (b) that the surface coverage of the doctor bladed films is highly discontinuous and far from ideal. Additionally, the MSCs pile on top of each other forming mountains of TiO_2, which in a device act as shorting pathways. This is seen more clearly in Figure 4.6 which shows the cross-sectional images of complete devices.

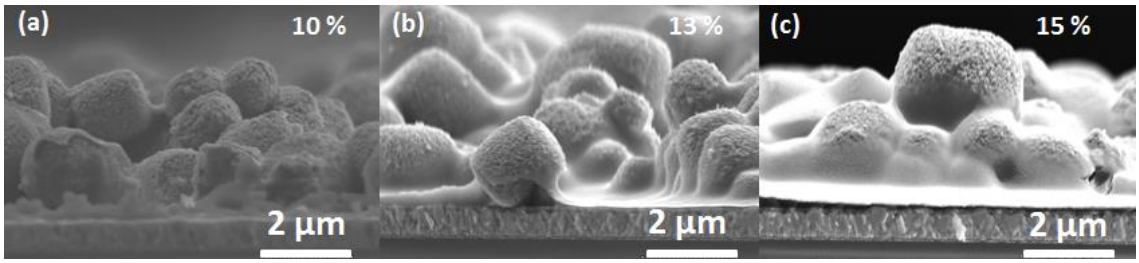

Figure 4.6: Cross-sectional SEM images of DSSCs fabricated using MSCs of TiO_2 as the photoanode with increasing concentrations of the HTM, where (a) shows a 10 % concentration of spiro-OMeTAD, (b) 13 % and (c) 15 %. SEM images were taken by Varun Sivaram of the Department of Physics, University of Oxford.

4.5.1 Low Temperature Processing of MSC Devices

In this section, I will discuss the fabrication of low temperature processed MSC-based devices. In order to achieve a smooth, continuous layer of TiO_2 the domain size of the MSCs was decreased. The MSCs used in this part of the investigation have a domain and pore size of 150 nm and 20 nm respectively. This decrease in the domain size of these particles also results in the first "transparent" films of this material, a prospect which is very exciting for BIPV. The MSC paste consists of a dispersion of MSC particles in ethanol (10 % by mass). This dispersion is spin-coated onto an FTO-coated glass substrate, with a pre-deposited 100 nm thick compact layer of TiO_2.

Deposition of the neat dispersion results in a visibly rough layer with poor adhesion to the substrate, assessed by the film being easily wiped away with a tissue. The performance of DSSCs fabricated with such films is relatively poor and irreproducible. However, if 15 mol% of titanium diisopropoxide bis(acetylacetonate) $Ti(acac)_2$ is added to this dispersion, it results in much improved adhesion of the film, with removal only possible by scratching with a scalpel or hard implement. It is possible that the inclusion of this $Ti(acac)_2$ results in the formation of very small nanoparticles of TiO_2 when the film is heated to 150 ˚C, and that these tiny nanoparticles not only help to bind the MSCs to the substrate, but also improve interparticle connections between individual mesoporous crystals. Subsequently, we added a small amount of terpineol to the dispersion, which produced smoother, more uniform films.

Figure 4.7 shows scanning electron microscope (SEM) images of the MSCs used in this investigation, as well as a cross sectional image of the final device

architecture, while **Figure 4.8** shows the percentage total, and diffuse transmission as a function of wavelength, through the different mesoporous TiO_2 films investigated here. Though there is still some diffuse transmission through the MSC films, they are predominantly non-scattering. Photographs of complete dye-sensitised device substrates (devoid of metal electrodes) are shown in Figure 4.8b to aid the visualisation of the degree of transparency.

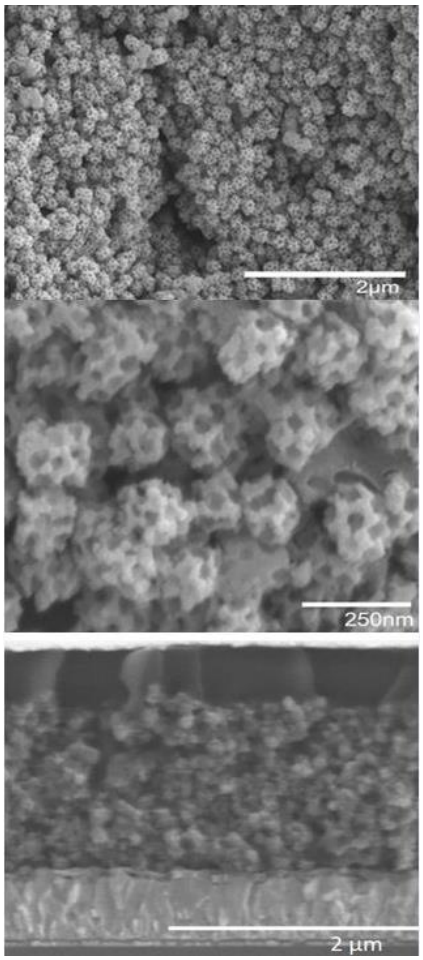

Figure 4.7: (a) Mesoporous single crystals (MSCs) of TiO_2 drop casted onto a substrate. (b) A close up view of drop casted MSCs. (c) Cross section of a working low temperature processed dye sensitized solar cell. The active layer of this device consists of a layer of MSCs sensitized with D102, and infiltrated with spiro-OMeTAD. MSCs synthesized by Dr. Edward J.W. Crossland of the Department of Physics, University of Oxford.

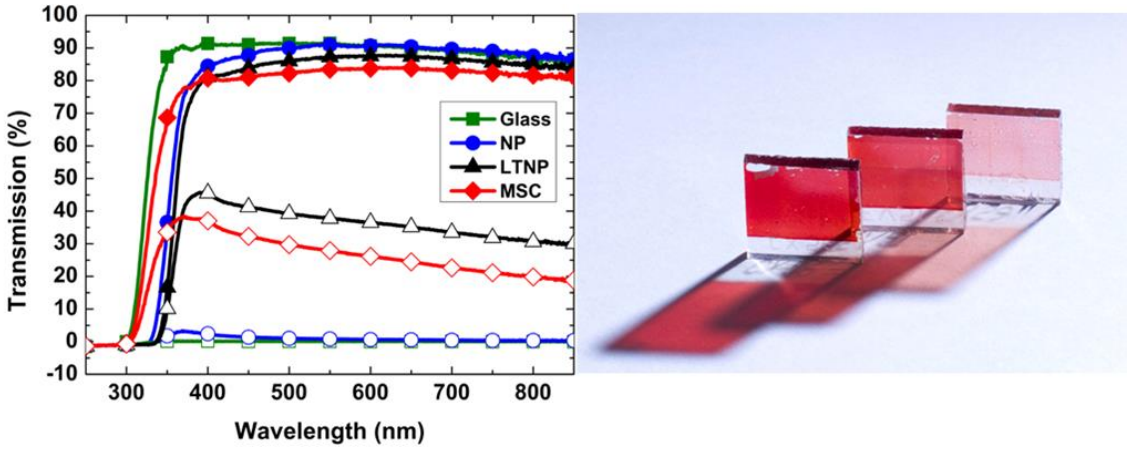

Figure 4.8: (a) Graph showing the percentage total and diffuse transmission vs. wavelength, for dyed films of sintered nanoparticles (NP), low temperature processed nanoparticles (LTNP) and low temperature processed mesocrystals (MSC). The solid points represent the total transmission, while the hollow points represent diffuse transmission; (b) Photograph illustrating the transparency of MSC films as compared to a nanoparticle film. From back to front; an 800 nm thick film of low temperature processed MSCs, a 2 µm thick film of low temperature processed MSCs, a 2 µm thick film of sintered nanoparticle paste.

In **Figure 4.9** we show the current-voltage characteristics and the solar cell performance parameters of devices made from the optimised MSC paste formulation, compared to nanoparticle control devices processed at both high temperature (employing commercial Dyesol 18 NRT) and low temperature (homemade 20 nm anatase TiO_2 nanoparticle solution). All DSSCs were fabricated using the organic indoline dye, termed D102, as a sensitizer.[29] For the first time, the efficiencies of the low temperature MSC devices match the efficiencies of the conventional, high temperature sintered, nanoparticle controls. In fact, efficiencies of over 3.7% have been obtained for the low temperature MSC devices, to date, the highest reported efficiency for a fully low temperature processed, solid state DSSC. It is also worth noting that these low temperature devices have not undergone the usual treatment with titanium tetrachloride ($TiCl_4$), a highly corrosive acid treatment, which is crucial to attaining

optimum performance in DSSCs using conventional TiO_2 materials, and is indeed employed here with the control devices.

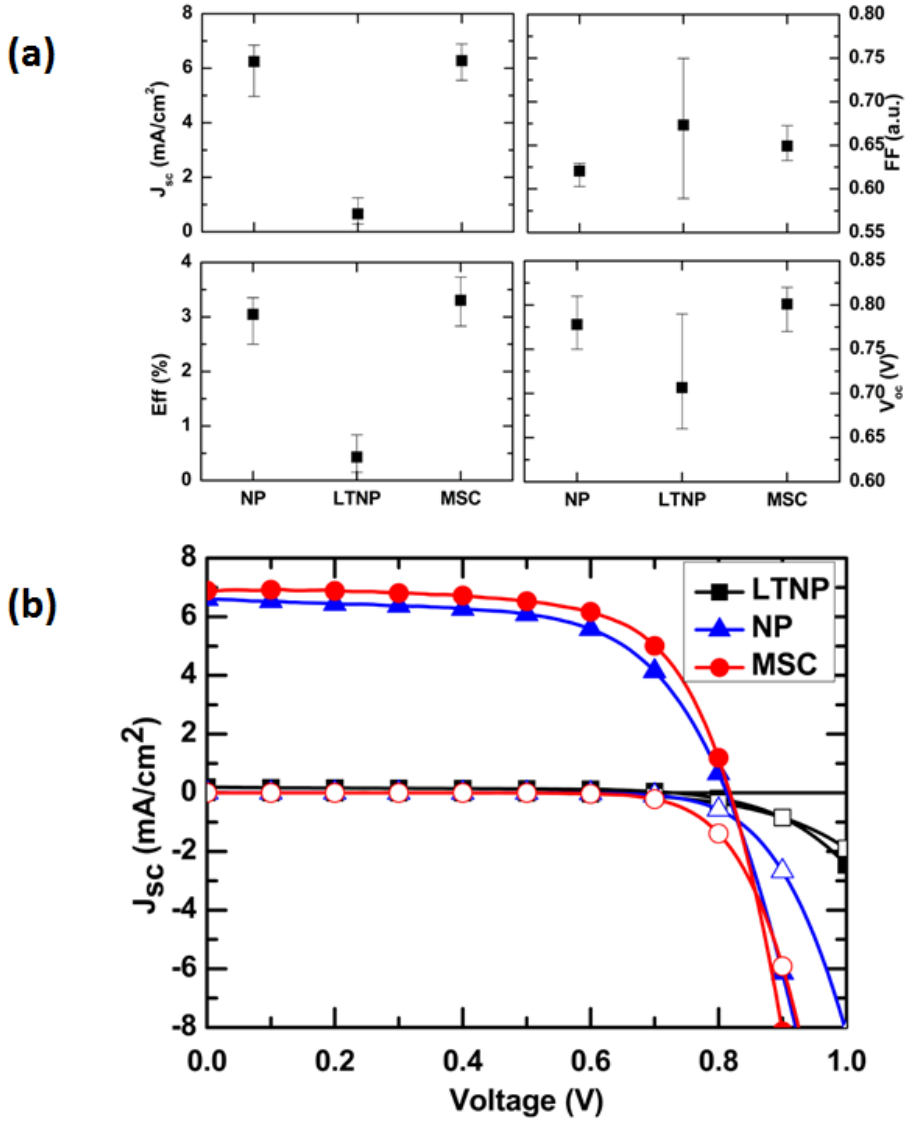

1

Figure 4.9: Current-Voltage Characteristics and Performance parameters. (a) Distribution of the performance metrics of a given batch of devices; (b) Current-voltage characteristics of the best performing solar cells for each parameter investigated: low temperature processed nanoparticles (LTNP), low temperature processed mesoporous single crystals (MSC), and the control device, high temperature sintered nanoparticles (NP). Performance parameters are given in Table 1.

	η (%)	J_{SC} (mA/cm^2)	V_{OC} (V)	F.F. (a.u.)
LTNP	0.10	0.20	0.73	0.51
MSC	3.73	6.89	0.82	0.66
NP	3.35	6.61	0.80	0.62

Table 4.1: Performance parameters of the best performing devices of all variables investigated.

The elimination of this $TiCl_4$ treatment effectively removes the second sintering step in the device fabrication process. While the successful exclusion of all processes which require high temperature sintering both simplifies and accelerates the manufacturing process, the removal of the $TiCl_4$ treatment excludes an acidic processing step which is problematic for metallic substrates; a very attractive prospect for large scale production of these devices. Not surprisingly, the low temperature, binder free nanoparticle analogues yielded efficiencies of << 1%. The current extracted from these devices was extremely low, suggesting inadequate electronic contact between individual particles, leading to very poor charge collection efficiencies. It must be noted that the coloration, and hence dye uptake of the binder free nanoparticle films was good as is shown by the absorbance of the dyed films which is shown in **Figure 4.10**.

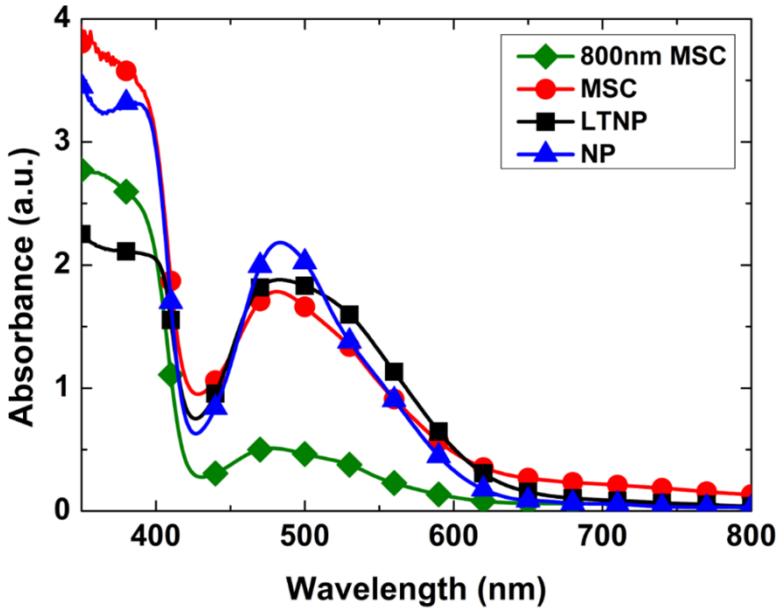

Figure 4.10: Absorbance of 800 nm and 2 μm thick MSC films, along with 2 μm thick low temperature processed and high temperature processed nanoparticle films dyed with D102.

An alternative explanation for these very low currents is that without the incorporation of the polymer binder and high temperature sintering, the resultant porosity of the film is on too small a scale to allow the infiltration of the hole transporting material (HTM). When polymer binders such as cellulose are added to these nanoparticle pastes, they allow for a very stable dispersion of the nanoparticles. Upon heating films of this dispersion the binder is burnt out of the film allowing for the formation of fairly large (20 nm) pores, which then facilitates facile infiltration of the HTM. In the absence of this binder there is a much larger degree of particle aggregation which results in the formation of smaller pores, hence making the HTM infiltration a much more difficult, and less effective process. In addition, when the low temperature nanoparticle paste was prepared in the same fashion as the MSC paste, the resulting film was far less robust, and susceptible to peeling off the substrate when immersed in the dye solution. This is also a factor which may have attributed to the poor performance of these devices.

It is worth noting that on average, MSC devices gave better results than the optimised control devices in all performance parameters with the exception of the short circuit current. This is likely to be due to a small decrease in the available surface area of the MSC layer as compared to the nanoparticle layer, something which has been previously observed in MSC films.[28] This decrease in surface area is as a result of the increased porosity of these films, stemming from the "dual porosity" that arises with the imperfect packing of already porous particles. It follows then, that the solution to this problem would be to fabricate devices with a thicker mesoporous layer. The devices shown in this study were 2 microns thick. We found that thicker films did not exhibit enhanced performance, as has been seen repeatedly observed for standard solid-state DSSCs.[30-32] This is likely to be due to combined factors of reduced pore filling of the hole-conductor reducing hole-transfer yield and enhancing recombination losses.[30,33,34]

The parasitic absorption in the p-doped hole conductor competing with light absorption in the dye-sensitizer, especially in the red to near infra-red region where the dye absorbs relatively weakly could also be a major limiting factor governing device thickness.[35,36] The latter issue of parasitic absorption in the HTM implies that very high photocurrents will only be possible in solid-state DSSCs with extremely strongly absorbing dyes, and/or higher surface area photoanodes in thinner films, so that light absorption in the dye competes more favourably.

4.6 Transient Photovoltage and Photocurrent Decay Measurements

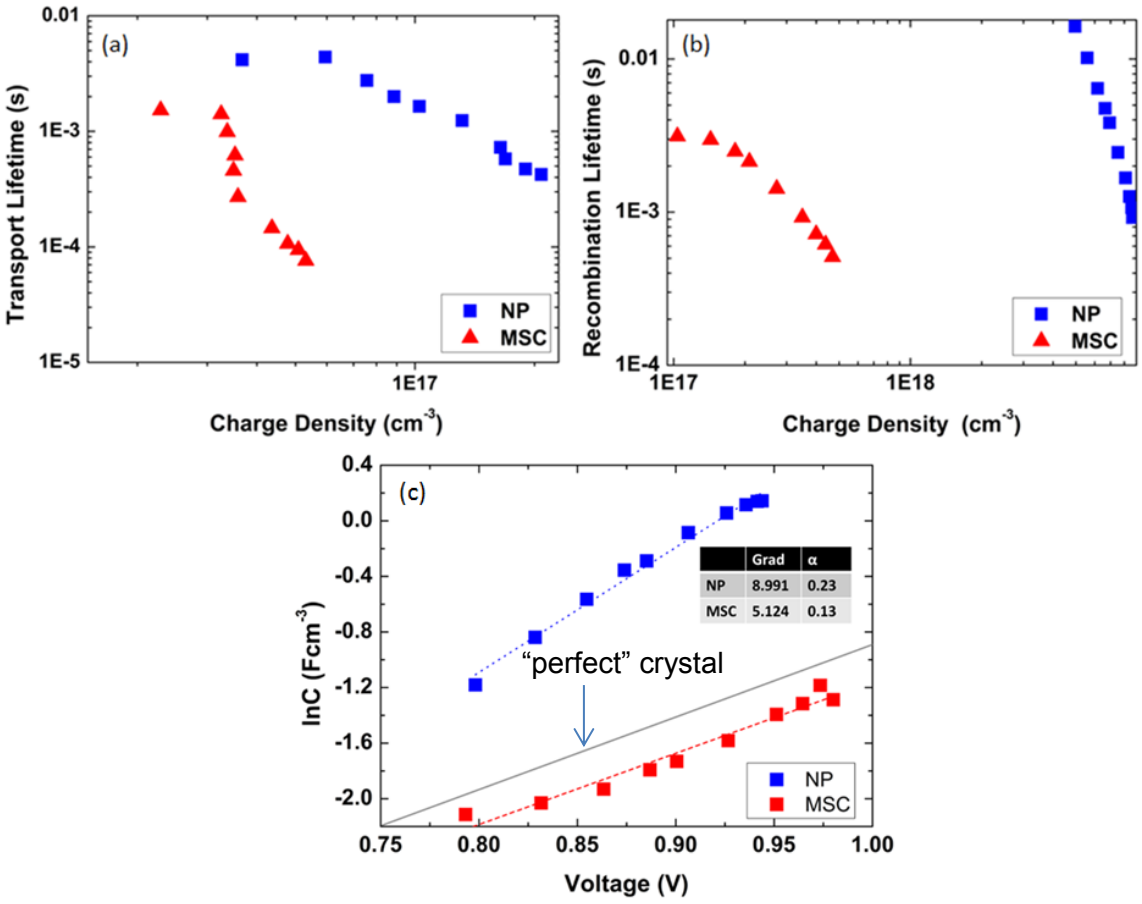

Figure 4.11: Transport and Recombination Characteristics. (a) Electron lifetime at short circuit (transport lifetime) vs. the charge density at short circuit for all low temperature processed MSC devices (red) and the high temperature sintered, nanoparticle control (blue); (b) Electron recombination lifetime vs. the charge density at open circuit for the same devices; (c). Capacitance-Voltage plots for both high temperature sintered nanoparticle (blue) and low temperature processed MSC devices (red). The linear fits of the data are shown by the dashed lines, and the slope of a theoretical TiO_2 nanocrystal, of perfect stoichiometry and crystallinity is shown on the solid grey line (offset for clarity). Transport and recombination characteristics measured in collaboration with Tomas Leijtens. Capacitance-voltage plot of a theoretically

perfect nanocrystals generated by Francesca Nunzi and Filippo De Angelis of Computational Laboratory for Hybrid/Organic Photovoltaics (CLHYO).

In order to better understand the electronic properties of the MSCs in solid-state DSSCs, the devices were further probed using transient photovoltage and photocurrent decay techniques.[27,30,37,38] Using these measurements it is possible to extract and compare both the transport and recombination rates of devices under comparable working conditions, as well as extract the density and distribution of conduction band tail states. The transport and recombination results are summarised in **Figure 4.11**. At comparable charge densities, the rate of electron transport in the MSC devices is up to two orders of magnitude faster than the sintered nanoparticle control with the charge collection lifetimes (obtained by fitting the transients to monoexponential decays) being as fast as 100 μs. This large increase in the electron transport rate could, in part, be attributed to the presence of fewer grain boundaries as a result of the increase in particle size. A similar effect has been observed in an experiment by Nakade *et al*., by varying the size of solid crystals, which depicts the influence of grain boundaries on the electron transport rate.[39] Interestingly, the conclusion of that study was that for optimal solar cell performance, a balance must be struck between the faster electron transport and decreased surface area that comes with the use of larger particles. Using MSCs of TiO_2 effectively solves this problem, since the domain size (particle size) can be increased independently of the pore size and hence the surface area of the resultant film.

Here, transport is compared at constant charge density. However, transport in mesoporous TiO_2 is considered to proceed via a multi-trapping mechanism; most electrons reside in localised tail, or sub band gap states, and only the small fraction of electrons in the conduction band are free to travel.[5,40-42] Hence, for a given charge density, a material with fewer sub band gap states will have a larger fractional occupancy of the conduction band, and as such exhibit faster average electron diffusion rates.[5]

Figure 4.11b shows the open circuit lifetime of these devices as a function of charge density. This measurement is used to probe the electron recombination rate (or lifetime) which is approximately equal to the rate of the voltage decay in the devices, when none of the charge perturbation is being collected. These results depict an increase in the recombination rate for MSC based devices with respect to the sintered nanoparticle controls. If recombination occurs predominantly through the conduction band, rather than through trapped electrons, this increase in the recombination rate may be as a result of a larger fractional occupancy of the conduction band states, and hence, faster recombination.[43] Remarkably, the large increase in the transport rate of this system compensates for this increase in the recombination rate, as is evidenced by the charge collection efficiency of the device being >90%.[44] Unfortunately, due to the extremely low currents, and general poor performance of the low temperature nanoparticle system, no reliable data was obtained for these devices.

In order to probe whether the differences in transport and recombination seen above are due solely to the extended crystallinity, or are largely dominated by the reduced density of sub band gap states, the differential capacitance of devices fabricated from both materials was determined. Figure 4.11c shows the open circuit voltage plotted against the natural logarithm of the differential capacitance, which is closely related to the sub band gap density of states (DOS).[45] From this, linear plots can be obtained, the gradient of which gives direct insight into the characteristic distribution of sub band gap trap states. The DOS of nanostructured metal oxides is described by the exponential distribution of **Equation 4.1**.[46]

$$g(E_{Fn}) = \frac{\alpha q N_L}{k_B T} \exp\left[\alpha(E_{Fn} - E_c)\Big/ k_B T\right] \quad (4.1)$$

where q is the electronic charge, k_B is the Boltzmann constant, T is the temperature, N_L is the total number of states below the conduction band, α is a parameter which describes the distribution of these states, E_{Fn} is the quasi Fermi level of the electrons, and E_C is the energy of the conduction band.

The capacitance-voltage plots show that the DOS for the MSCs is quite different from that of the nanoparticles. Using the experimental data and the fit to equation 4.1, the α parameters for both the nanoparticles and MSCs have been calculated, yielding values of 0.23 and 0.13 respectively. Typical α values for nanoparticulate TiO_2 lie within the range of 0.2-0.5,[46] in good agreement with the result obtained. A recent study by Nunzi et al. presented a computational investigation into the nature of trap states in completely stoichiometric, perfectly crystalline TiO_2 nanoparticles.[47] Using equation 4.1, the α parameter of this "perfect" TiO_2 was calculated to be 0.13, a value which is in exact agreement with the value obtained for the devices constricted from MSCs. The theoretical investigation revealed the presence of inherent trap states even in perfectly stoichiometric, crystalline TiO_2, due to the presence of under-coordinated Ti^{4+} surface atoms which lie at the intersections of the (101) crystal faces. The agreement between the α values for "perfect" TiO_2 nanocrystals and MSCs suggests that through this method of synthesis, all avoidable trap states have been eliminated in MSCs of TiO_2, leaving only the inherent trap sites due to under-coordinated Ti^{4+} atoms.

This decrease in the density of trap states within the MSCs provides a valid explanation for the lower charge densities found in the MSC films, and is consistent

with the faster electron transport exhibited by these devices, as well as the faster recombination, if recombination does indeed occur predominantly through the conduction band electrons and holes in the spiro-OMeTAD. This also explains the higher open-circuit voltages typically observed in MSC devices. However, clearly addressing the issue of the greatly increased recombination, and hence enabling a much larger build-up of charge in the MSC devices at open-circuit, should enable a significant further increase in open-circuit voltage.

4.7 Summary and Outlook

In conclusion, through the implementation of MSCs in DSSCs, I have demonstrated a simple route to the manufacture of low temperature processed DSSCs with reduced electronic disorder and enhanced charge transport properties. This study presents the first low temperature fabrication method by which the performances of dye-sensitized devices are comparable to the performances achieved using a conventional, high temperature sintering approach. Solid-state DSSCs assembled via the low temperature route yielded power conversion efficiencies of up to 3.7% under 1 sun illumination. It is quite clear that there is much scope to improve the dye sensitized solar cells by: i) Inhibiting recombination, thus allowing a much larger build-up of charge and hence open-circuit voltage, ii) maximising the surface area for dye adsorption and/or employing more strongly absorbing sensitizers to compete more favourably with parasitic absorption in the hole-transporter, iii) employing higher mobility HTMs to minimise the doping requirements, also with the aim of enabling better light absorption in the dye. Here, this method of low temperature processing not only opens the doorway to flexible, lightweight, solid state DSSCs, but should also enable the realisation of monolithic, multi-junction solid-state DSSCs, which may then allow for competitive efficiency to be achieved. Beyond PV, the low temperature

processed mesoporous single crystal films may also find application in energy storage and photo catalysis.

4.8 References

[1] Snaith, H. J. & Schmidt-Mende, L. Advances in Liquid-Electrolyte and Solid-State Dye-Sensitized Solar Cells. *Advanced Materials* **19**, 3187-3200, doi:10.1002/adma.200602903 (2007).

[2] Benkstein, K. D., Kopidakis, N., van de Lagemaat, J. & Frank, A. J. Influence of the Percolation Network Geometry on Electron Transport in Dye-Sensitized Titanium Dioxide Solar Cells. *The Journal of Physical Chemistry B* **107**, 7759-7767, doi:10.1021/jp022681l (2003).

[3] O'Regan, B. C. & Durrant, J. R. Kinetic and Energetic Paradigms for Dye-Sensitized Solar Cells: Moving from the Ideal to the Real. *Accounts of Chemical Research* **42**, 1799-1808, doi:10.1021/ar900145z (2009).

[4] Bisquert, J. Chemical Diffusion Coefficient of Electrons in Nanostructured Semiconductor Electrodes and Dye-Sensitized Solar Cells. *The Journal of Physical Chemistry B* **108**, 2323-2332, doi:10.1021/jp035397i (2004).

[5] Leijtens, T., Lim, J., Teuscher, J., Park, T. & Snaith, H. J. Charge Density Dependent Mobility of Organic Hole-Transporters and Mesoporous TiO2 Determined by Transient Mobility Spectroscopy: Implications to Dye-Sensitized and Organic Solar Cells. *Advanced Materials* **25**, 3227-3233, doi:10.1002/adma.201300947 (2013).

[6] Snaith, H. J. & Grätzel, M. Electron and Hole Transport through Mesoporous TiO2 Infiltrated with Spiro-MeOTAD. *Advanced Materials* **19**, 3643-3647, doi:10.1002/adma.200602085 (2007).

[7] O'Regan, B. & Gratzel, M. A low-cost, high-efficiency solar cell based on dye-sensitized colloidal TiO2 films. *Nature* **353**, 737-740 (1991).

[8] Mathew, S. *et al.* Dye-sensitized solar cells with 13% efficiency achieved through the molecular engineering of porphyrin sensitizers. *Nature chemistry* (2014).

[9] Lee, M. M., Teuscher, J., Miyasaka, T., Murakami, T. N. & Snaith, H. J. Efficient Hybrid Solar Cells Based on Meso-Superstructured Organometal Halide Perovskites. *Science* **338**, 643-647, doi:10.1126/science.1228604 (2012).

[10] Ball, J. M., Lee, M. M., Hey, A. & Snaith, H. Low-Temperature Processed Mesosuperstructured to Thin-Film Perovskite Solar Cells. *Energy & Environmental Science* (2013).

[11] Noh, J. H., Im, S. H., Heo, J. H., Mandal, T. N. & Seok, S. I. Chemical Management for Colorful, Efficient, and Stable Inorganic–Organic Hybrid Nanostructured Solar Cells. *Nano Letters* **13**, 1764-1769, doi:10.1021/nl400349b (2013).

[12] Etgar, L. *et al.* Mesoscopic CH3NH3PbI3/TiO2 Heterojunction Solar Cells. *Journal of the American Chemical Society* **134**, 17396-17399, doi:10.1021/ja307789s (2012).

[13] Liu, D. & Kelly, T. L. Perovskite solar cells with a planar heterojunction structure prepared using room-temperature solution processing techniques. *Nat Photon* **8**, 133-138, doi:10.1038/nphoton.2013.342

http://www.nature.com/nphoton/journal/v8/n2/abs/nphoton.2013.342.html#supplementary-information (2014).

[14] Wojciechowski, K., Saliba, M., Leijtens, T., Abate, A. & Snaith, H. J. Sub-150 [degree]C processed meso-superstructured perovskite solar cells with enhanced efficiency. *Energy & Environmental Science* **7**, 1142-1147, doi:10.1039/C3EE43707H (2014).

[15] Gao, J., Yu, G. & Heeger, A. J. Polymer p-i-n Junction Photovoltaic Cells. *Advanced Materials* **10**, 692-695, doi:10.1002/(SICI)1521-4095(199806)10:9<692::AID-ADMA692>3.0.CO;2-5 (1998).

[16] Ma, W., Yang, C., Gong, X., Lee, K. & Heeger, A. J. Thermally Stable, Efficient Polymer Solar Cells with Nanoscale Control of the Interpenetrating Network Morphology. *Advanced Functional Materials* **15**, 1617-1622, doi:10.1002/adfm.200500211 (2005).

[17] Jonathan J. M, H. & Richard H, F. in *Clean Electricity from Photovoltaics* Vol. Volume 1 *Series on Photoconversion of Solar Energy* 377-445 (PUBLISHED BY IMPERIAL COLLEGE PRESS AND DISTRIBUTED BY WORLD SCIENTIFIC PUBLISHING CO., 2001).

[18] Brabec, C., Scherf, U. & Dyakonov, V. *Organic photovoltaics: materials, device physics, and manufacturing technologies*. (Wiley. com, 2011).

[19] Halme, J., Saarinen, J. & Lund, P. Spray deposition and compression of TiO2 nanoparticle films for dye-sensitized solar cells on plastic substrates. *Solar Energy Materials and Solar Cells* **90**, 887-899, doi:http://dx.doi.org/10.1016/j.solmat.2005.05.013 (2006).

[20] Heng, L. *et al.* p–n-Junction-Based Flexible Dye-Sensitized Solar Cells. *Advanced Functional Materials* **20**, 266-271, doi:10.1002/adfm.200901671 (2010).

[21] Weerasinghe, H. C., Sirimanne, P. M., Franks, G. V., Simon, G. P. & Cheng, Y. B. Low temperature chemically sintered nano-crystalline TiO2 electrodes for flexible dye-sensitized solar cells. *Journal of Photochemistry and Photobiology A: Chemistry* **213**, 30-36, doi:http://dx.doi.org/10.1016/j.jphotochem.2010.04.016 (2010).

[22] Ito, S. *et al.* High-efficiency (7.2%) flexible dye-sensitized solar cells with Ti-metal substrate for nanocrystalline-TiO2 photoanode. *Chemical Communications* **0**, 4004-4006 (2006).

[23] Bessho, T., Zakeeruddin, S. M., Yeh, C.-Y., Diau, E. W.-G. & Grätzel, M. Highly Efficient Mesoscopic Dye-Sensitized Solar Cells Based on Donor–Acceptor-Substituted Porphyrins. *Angewandte Chemie International Edition* **49**, 6646-6649, doi:10.1002/anie.201002118 (2010).

[24] Campbell, W. M. *et al.* Highly Efficient Porphyrin Sensitizers for Dye-Sensitized Solar Cells. *The Journal of Physical Chemistry C* **111**, 11760-11762, doi:10.1021/jp0750598 (2007).

[25] Schmidt-Mende, L. *et al.* Zn-Porphyrin-Sensitized Nanocrystalline TiO2 Heterojunction Photovoltaic Cells. *ChemPhysChem* **6**, 1253-1258, doi:10.1002/cphc.200500147 (2005).

[26] Weickert, J., Dunbar, R. B., Hesse, H. C., Wiedemann, W. & Schmidt-Mende, L. Nanostructured Organic and Hybrid Solar Cells. *Advanced Materials* **23**, 1810-1828, doi:10.1002/adma.201003991 (2011).

[27] Docampo, P., Guldin, S., Steiner, U. & Snaith, H. J. Charge Transport Limitations in Self-Assembled TiO2 Photoanodes for Dye-Sensitized Solar Cells. *The Journal of Physical Chemistry Letters* **4**, 698-703, doi:10.1021/jz400084n (2013).

[28] Crossland, E. J. W. *et al.* Mesoporous TiO2 single crystals delivering enhanced mobility and optoelectronic device performance. *Nature* **495**, 215-219, doi:http://www.nature.com/nature/journal/v495/n7440/abs/nature11936.html#supplementary-information (2013).

[29] Schmidt-Mende, L. *et al.* Organic Dye for Highly Efficient Solid-State Dye-Sensitized Solar Cells. *Advanced Materials* **17**, 813-815, doi:10.1002/adma.200401410 (2005).

[30] Snaith, H. J. *et al.* Charge collection and pore filling in solid-state dye-sensitized solar cells. *Nanotechnology* **19**, doi:10.1088/0957-4484/19/42/424003 (2008).

[31] Melas-Kyriazi, J. *et al.* The Effect of Hole Transport Material Pore Filling on Photovoltaic Performance in Solid-State Dye-Sensitized Solar Cells. *Advanced Energy Materials* **1**, 407-414, doi:10.1002/aenm.201100046 (2011).

[32] Schmidt-Mende, L., Zakeeruddin, S. M. & Gratzel, M. Efficiency improvement in solid-state-dye-sensitized photovoltaics with an amphiphilic Ruthenium-dye. *Applied Physics Letters* **86**, 013504-013503 (2005).

[33] Schmidt-Mende, L. & Grätzel, M. TiO2 pore-filling and its effect on the efficiency of solid-state dye-sensitized solar cells. *Thin Solid Films* **500**, 296-301, doi:http://dx.doi.org/10.1016/j.tsf.2005.11.020 (2006).

[34] Moule, A. J. *et al.* Optical description of solid-state dye-sensitized solar cells. I. Measurement of layer optical properties. *Journal of Applied Physics* **106**, 073111-073119 (2009).

[35] Huang, D. M., Snaith, H. J., Gratzel, M., Meerholz, K. & Moule, A. J. Optical description of solid-state dye-sensitized solar cells. II. Device optical modeling with implications for improving efficiency. *Journal of Applied Physics*, **106**, 073112-073116 (2009).

[36] Margulis, G. Y., Hardin, B. E., Ding, I. K., Hoke, E. T. & McGehee, M. D. Parasitic Absorption and Internal Quantum Efficiency Measurements of Solid-State Dye Sensitized Solar Cells. *Advanced Energy Materials* **3**, 959-966, doi:10.1002/aenm.201300057 (2013).

[37] O'Regan, B. C. *et al.* Measuring Charge Transport from Transient Photovoltage Rise Times. A New Tool To Investigate Electron Transport in Nanoparticle Films. *The Journal of Physical Chemistry B* **110**, 17155-17160, doi:10.1021/jp062761f (2006).

[38] Docampo, P. *et al.* Triblock-Terpolymer-Directed Self-Assembly of Mesoporous TiO2: High-Performance Photoanodes for Solid-State Dye-Sensitized Solar Cells. *Advanced Energy Materials* **2**, 676-682, doi:10.1002/aenm.201100699 (2012).

[39] Nakade, S. *et al.* Influence of TiO2 Nanoparticle Size on Electron Diffusion and Recombination in Dye-Sensitized TiO2 Solar Cells. *The Journal of Physical Chemistry B* **107**, 8607-8611, doi:10.1021/jp034773w (2003).

[40] Peter, L. "Sticky Electrons" Transport and Interfacial Transfer of Electrons in the Dye-Sensitized Solar Cell. *Accounts of Chemical Research* **42**, 1839-1847, doi:10.1021/ar900143m (2009).

[41] Schlichthörl, G., Park, N. G. & Frank, A. J. Evaluation of the Charge-Collection Efficiency of Dye-Sensitized Nanocrystalline TiO2 Solar Cells. *The Journal of Physical Chemistry B* **103**, 782-791, doi:10.1021/jp9831177 (1999).

[42] Bisquert, J. Theory of the Impedance of Electron Diffusion and Recombination in a Thin Layer. *The Journal of Physical Chemistry B* **106**, 325-333, doi:10.1021/jp011941g (2001).

[43] Kopidakis, N., Benkstein, K. D., van de Lagemaat, J. & Frank, A. J. Transport-Limited Recombination of Photocarriers in Dye-Sensitized Nanocrystalline TiO2 Solar Cells. *The Journal of Physical Chemistry B* **107**, 11307-11315, doi:10.1021/jp0304475 (2003).

[44] Sivaram, V., Kirkpatrick, J. & Snaith, H. Critique of charge collection efficiencies calculated through small perturbation measurements of dye sensitized solar cells. *Journal of Applied Physics* **113**, 063709-063706 (2013).

[45] Docampo, P. *et al.* Control of Solid-State Dye-Sensitized Solar Cell Performance by Block-Copolymer-Directed TiO2 Synthesis. *Advanced Functional Materials* **20**, 1787-1796, doi:10.1002/adfm.200902089 (2010).

[46] Fabregat-Santiago, F., Garcia-Belmonte, G., Mora-Sero, I. & Bisquert, J. Characterization of nanostructured hybrid and organic solar cells by impedance spectroscopy. *Physical Chemistry Chemical Physics* **13**, 9083-9118, doi:10.1039/C0CP02249G (2011).

[47] Nunzi, F. *et al.* Inherent electronic trap states in TiO2 nanocrystals: effect of saturation and sintering. *Energy & Environmental Science* **6**, 1221-1229, doi:10.1039/C3EE24100A (2013).

Chapter 5

Alternative Absorber Materials: Sb_2S_3 Sensitized Solar Cells

5.1 Broad Context

As previously discussed in Chapter 2, one of the major limitations of solid-state dye sensitized solar cells (ss-DSSCs) is that its performance reaches an optimum only when a monolayer of dye is deposited.[1,2] As the optimised thickness of the ss-DSSC currently stands at between 1μm and 3 μm,[3,4] the natural inclination would be simply to make the mesoporous TiO_2 layer of the devices thicker. A thicker layer would then provide a greater surface area for dye adsorption and thus more light will be absorbed by the device, resulting in a boost in power conversion efficiencies. However, with hole transporting materials (HTMs) such as spiro-OMeTAD, the current gold standard for ss-DSSCs, this approach is unfeasible due to the parasitic absorption exhibited by this particular HTM.[5,6]

There are many different ways to tackle this problem; the most rudimentary of which is simply to use a sensitizer which absorbs more light, and can operate efficiently when more than a monolayer is deposited on the mesoporous layer. To this end, this chapter presents an investigation into the use of the inorganic semiconductor antimony

sulphide (Sb_2S_3) as an absorber material in the conventional sensitized solar cell (SSC) architecture.

5.2 Introduction

To date, ss-DSSCs have consistently fallen short of their potential to match or even surpass the power conversion efficiencies of their liquid electrolyte counterparts. This is largely due to the thickness limitations in the ss-DSSC, which arise as a result of the parasitic absorption of the most commonly used HTM, spiro-OMeTAD.[5,6] Of course, thinner TiO_2 films result in a reduced surface area for dye adsorption, and consequently a decrease in the absorbance of the films. As such, in order for solid-state SSCs to even begin to approach the power conversion efficiencies of liquid electrolyte based devices, this decrease in light absorption must be addressed. The simplest method of addressing this problem is to employ a more highly absorbing sensitizer which can operate efficiently when more than a monolayer is deposited on the mesoporous layer. To this end, many inorganic absorbers have been investigated for use in this type of sensitized structure.

Inorganic absorber materials are prime candidates for fulfilling the requirements listed above. These materials possess many attractive features such as having higher molar extinction coefficients than their organometallic or organic counterparts,[7] high intrinsic carrier mobilities,[8] and also present the opportunity to tune the band gap of the absorber by exploiting quantum size effects.[9,10] Indeed, for equivalent device configurations, a semiconductor sensitized solar cell (SSSC) can exhibit absorption which is five times greater than that of its organic counterpart[11] which has made light absorbing semiconductors prime candidates for incorporation into the solid state sensitized solar cell. As aforementioned, SSSCs can be subdivided into two major

classes, the extremely thin absorber (ETA) cell and the quantum dot sensitized solar cell (QDSSC). This chapter focuses on the ETA configuration, employing Sb_2S_3 as the light absorbing material.

For a number of years Sb_2S_3 has been considered to be one of the most promising absorber materials for incorporation into photovoltaic devices with the ETA architecture. With a band gap of between 1.7 eV- 1.8 eV resulting in broad absorption over the visible spectrum,[12] and a high absorption coefficient, $\alpha \geq 5 \times 10^4$ cm^{-1}, Sb_2S_3 seemed poised to deliver high efficiency low cost devices. As an added bonus, it is comprised of relatively non-toxic, cheap and abundant materials. Hence, Sb_2S_3 has been widely investigated in ss-SSSCs with various HTMs such as; CuSCN,[13-15] spiro-OMeTAD[16] and P3HT[17], yielding power conversion efficiencies of 3.1%, 3.37% and 5.13% respectively. The highest reported efficiency for this material however, has been obtained by using a blend of PCPDTBT and PCBM; which serves as both a hole transporter as well as a light absorber, and stands at 6.5 % under simulated full sunlight.[18]

Sb_2S_3 is typically deposited via chemical bath deposition (CBD)[17-19] however, it can also be deposited via other methods such as atomic layer deposition (ALD)[15] or even doctor blading.[20] In the archetypal device architecture, a thin amorphous layer of Sb_2S_3 is deposited onto mesoporous TiO_2 electrodes via CBD, and the substrate is then annealed under nitrogen atmosphere for 30 minutes in order convert the amorphous Sb_2S_3 to crystalline stibnite. One important consideration in this process is the degree of surface coverage imparted to the mesoporous oxide. A delicate balance must be struck between the thickness of the absorber layer and the extent of coverage of the oxide surface, as too thick an absorber layer tends to result in increased levels of internal recombination,[21] while too thin a layer can result in direct contact between the electron transporting and hole-transporting mediums, which will again result in an increase in

electron-hole recombination. One method of combating the latter is to incorporate a buffer layer, a very common practice in ETAs.[22]

When manufacturing SSSCs it is important to strike a balance between the thickness of the absorber layer and the size of the pores in the mesostructured electrodes. While having a thick absorbing layer will act to increase the absorption of light, it also inhibits the infiltration of the HTM into the pores of the electrode. This reduces the ability of the HTM to facilitate the regeneration of the absorber.[23] It follows then, that the most effective device architecture would consist of a mesostructured electrode with fairly large pores. This would allow sufficient exploitation of the high extinction coefficient and light harvesting ability of the semiconductor, whilst still allowing efficient infiltration of the HTM. Various mesostructures have been used with such materials. These include nanowires,[24,25] nanotubes[26,27] and inverse opals[28] to name a few.

Nanowires and nanorods are part of an interesting class of materials used in solar energy conversion. These materials are believed to be preferable to a sintered network of nanocrystals as they provide a naturally directed pathway for electron transport.[8] The disadvantage of such architectures is that they sacrifice a large internal surface area for faster electron transport. Recent studies of single crystal nanowires have yielded results which show that electron transport, in this type of device architecture, is two orders of magnitude faster than in mesoporous nanoparticulate layers of the same thickness. [29,30] Therefore, the concept of a single crystalline, wide band gap semiconductor with internal porosity, such as the mesoporous single crystals (MSCs) discussed in Chapter 4, is one which is very attractive for solar energy conversion. In particular, this type of mesostructure may prove to be ideal for inorganic absorbers as it combines a fairly open TiO_2 structure with fast electron transport.

In this chapter, MSCs are used as the photoanode in the fabrication of Sb_2S_3 sensitized solar cells, and the performance of MSC based devices is compared to that of commercially available TiO_2 paste (Dyesol 18 NR-T), as well as devices based on an insulating Al_2O_3 scaffold.

5.3 Device Fabrication

Before full devices were assembled, the optimum thickness of Sb_2S_3 was determined. In order to do this, microscope slides were coated with a 1 μm thick layer of TiO_2 which was then sintered to 500 ˚C. The TiO_2 coated slides were then placed into the Sb_2S_3 chemical bath as described in Chapter 3; and taken out at intervals of 1, 2 and 3 hours, and one was left overnight. After being taken out of the bath, the samples were annealed in nitrogen atmosphere at 300 ˚C for 30 minutes and the absorbance of the films was measured. These results are shown in **Figure 5.1**. The thickness of the film after a 3 hour deposition time gave optimal absorption, and as such, this deposition time was used in the fabrication of all Sb_2S_3 based solar cells presented here.

Having determined the optimal deposition time, photoanodes were fabricated using commercially available nanoparticle paste, MSCs, and an Al_2O_3 paste as an insulating scaffold. The MSCs used in this investigation had a domain size of 300 nm and a pore size of 50 nm, in order to facilitate deposition of the absorber as well as infiltration of the HTM. Fabricating a photovoltaic device by depositing an absorber material on an insulating scaffold is not without precedence. Lee *et al* have shown the operation of a hybrid organic-inorganic lead halide perovskite on a mesoporous alumina scaffold, achieving power conversion efficiencies of over 10 %.[31] This device configuration has been termed the mesosuperstructured solar cell (MSSC). The device results are presented in **Figure 5.2**.

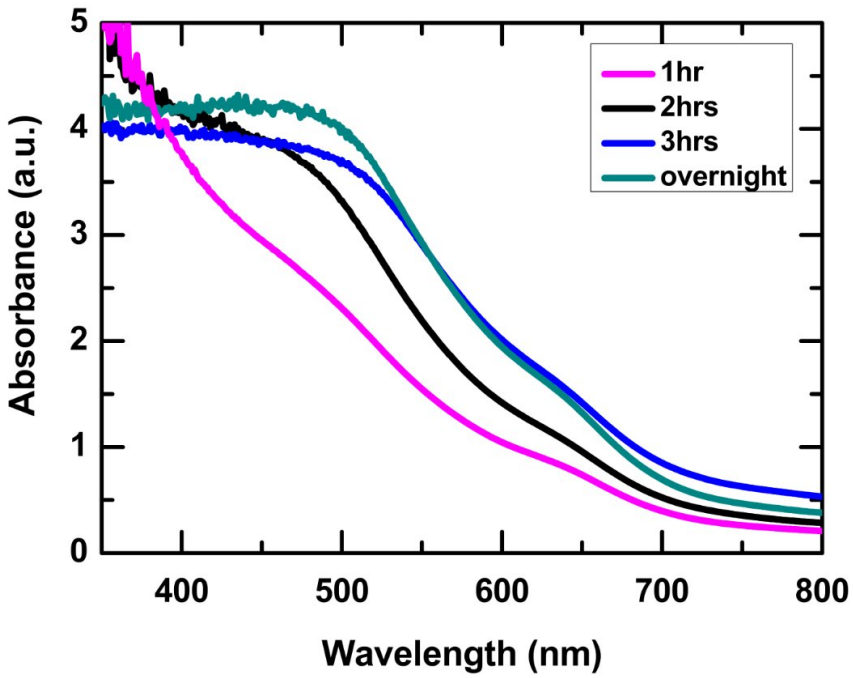

Figure 5.1: Absorbance vs. wavelength for different Sb_2S_3 deposition times.

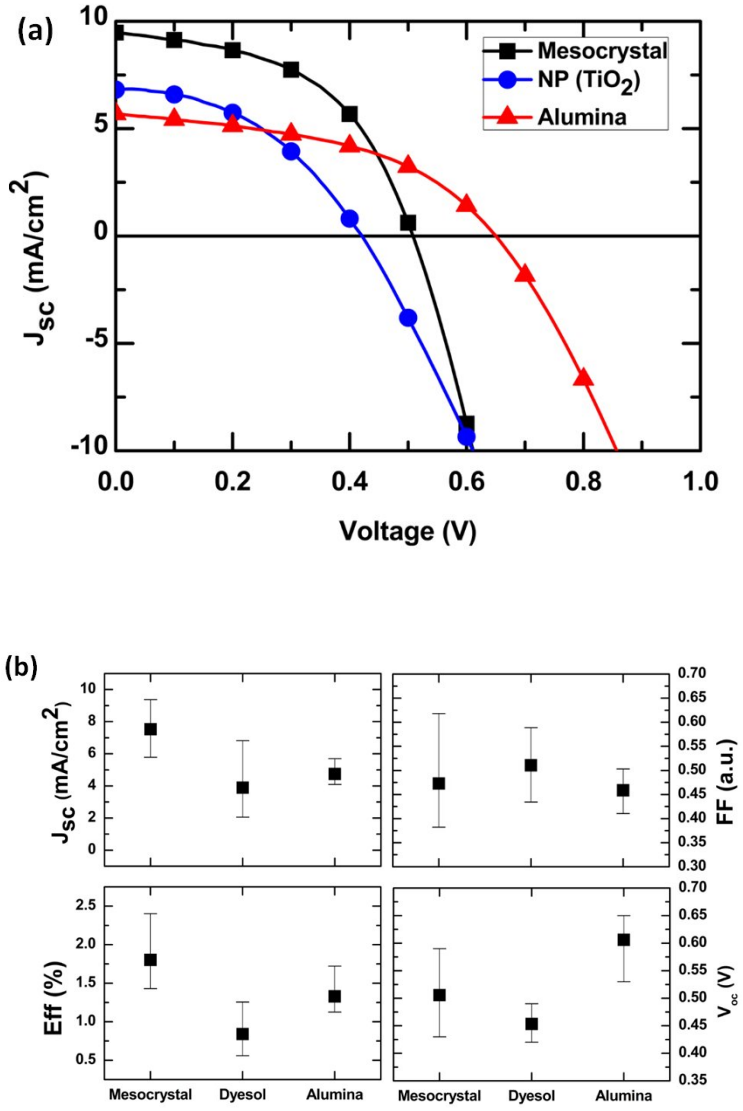

Figure 5.2: (a) Current-Voltage curves of the best performing Sb_2S_3 devices fabricated on mesoporous single crystals (mesocrystals), TiO_2 nanoparticles (Dyesol) and on an alumina scaffold. (b) Performance parameters of a batch of Sb_2S_3 devices.

	J_{sc} (mA/cm^2)	□ (%)	V_{oc} (V)	F.F. (a.u.)
Mesocrystal (MSC)	9.37	2.41	0.50	0.51
Nanoparticle	6.82	1.25	0.42	0.43
Alumina	5.69	1.72	0.65	0.42

Table 1: Performance parameters of the best performing devices of all configurations investigated.

From the device results presented above it can be seen that the MSC based devices outperform both regular nanoparticle based devices as well as alumina based devices. One of the reasons for this is quite likely the increased pore size of the MSCs. In addition to the 50 nm pore size of the MSCs (as opposed to 15-20 nm pores in both nanoparticle and alumina films), there arises a "dual porosity" in MSC films as a result of the imperfect packing of intrinsically porous particles. This dual porosity permits for the deposition of Sb_2S_3 without clogging the pores of the TiO_2 layer so that when the HTM is deposited it can adequately infiltrate the structure. The complete infiltration of the structure by the HTM lends to intimate contact between the two materials, the HTM and the Sb_2S_3, allowing more effective hole extraction. This causes a decrease in the recombination exhibited in the device,[23] evidenced by the increase in the average V_{OC} of MSC based devices as opposed to nanoparticle based devices.

Interestingly, Sb_2S_3 is not only operational in an MSSC architecture, but outperforms nanoparticle based devices. Since the size of the mesopores in both of these films is roughly the same, this increase in the power conversion efficiency cannot be attributed to a decrease in internal recombination in the absorber layer. However, there is on average, a 200 mV increase in the voltage of the MSSC devices as compared to the nanoparticle based ones.

As Al_2O_3 is an insulating material, the injection of electrons from Sb_2S_3 into its conduction band can be ruled out. This therefore suggests that electron transport is occurring through the Sb_2S_3 material itself, bypassing the roughly 200 mV voltage loss which would occur when electrons are injected into the conduction band of a mesoporous oxide such as TiO_2 for example. This process is illustrated in **Figure 5.3**. A similar device has recently been demonstrated by O'Mahony *et al* where the TiO_2 has been completely removed from the structure.[20] In this case, a porous Sb_2S_3 acts both as the light absorber as well as the charge transport medium. Unfortunately, while operational, the performance of the device is much poorer than the ones shown here, exhibiting a power conversion efficiency of 0.23 %. This could be due to poor porosity in the film, additionally, the alumina scaffold may play an important role in the crystallisation of the Sb_2S_3 upon heating.

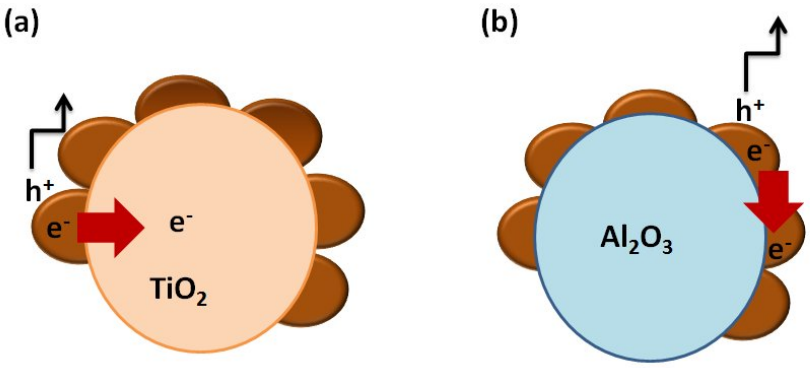

Figure 5.3: Electron transport mechanisms in (a) TiO_2 and (b) Al_2O_3. When the Sb_2S_3 is deposited on mesoporous TiO_2, electrons are injected into the conduction band of the TiO_2 and transported through the mesoporous layer to the bottom electrode, while holes are transported through the P3HT to the top electrode. Conversely, in the case of the Al_2O_3 scaffold, electrons cannot be injected into the conduction band of the alumina, and as such are transported through the Sb_2S_3 to the bottom electrode. Hole transport here occurs via the same mechanism.

It must be noted however, that even with the increased porosity of MSCs of titania, and the consistent voltage increase of the MSSC devices the performance of these Sb_2S_3 devices still fall short of expectations. A recent study by Dennler and co-workers suggests that the reason for this may be extremely high recombination rates within the absorber material itself.[14] They attribute the generally poor voltages of even the best performing Sb_2S_3 devices to a broad distribution of sub-band gap trap states within the material which act as recombination centres for photogenerated charges. This is perhaps a very real reason why Sb_2S_3 based devices are yet to achieve predicted power conversion efficiencies. If this material is to deliver high efficiency devices, passivation or elimination of these defect states must be explored.

5.4 Summary and Outlook

In conclusion, the work presented in this chapter has shown that the tunability of the pore size of mesoporous single crystals of TiO_2 allows them to be desirable photoanodes for semiconductor-sensitized solar cells. Using these crystals as the material for the photoanode has resulted in an average increase in the open circuit voltage from 0.4 V- 0.5V. This increase in voltage has been attributed to a decrease in recombination as increased porosity of the layer allows adequate infiltration of the hole transporting material, and thus efficient regeneration of the absorber material. Additionally, it has been proven that this material can also work in a meso-superstructured solar cell configuration where it both absorbs light and transports charge. This device architecture allows for a 200 mV increase in the open circuit voltage of the devices as it bypasses the voltage loss which occurs when electrons are injected from the conduction band of the absorber material into the conduction band of the TiO_2. However, these marginal improvements are not enough to give these devices the efficiency boost needed to be competitive. The presence of a large number of trap states in this material is likely hindering vast improvements in power conversion

efficiencies, and as such passivation of these trap states must be explored if Sb_2S_3 based devices are to reach their full potential.

5.5 References

[1] Yum, J.-H., Chen, P., Grätzel, M. & Nazeeruddin, M. K. Recent Developments in Solid-State Dye-Sensitized Solar Cells. *ChemSusChem* **1**, 699-707, doi:10.1002/cssc.200800084 (2008).

[2] Khazraji, A. C., Hotchandani, S., Das, S. & Kamat, P. V. Controlling Dye (Merocyanine-540) Aggregation on Nanostructured TiO2 Films. An Organized Assembly Approach for Enhancing the Efficiency of Photosensitization. *The Journal of Physical Chemistry B* **103**, 4693-4700, doi:10.1021/jp9903110 (1999).

[3] Snaith, H. J. & Schmidt-Mende, L. Advances in Liquid-Electrolyte and Solid-State Dye-Sensitized Solar Cells. *Advanced Materials* **19**, 3187-3200, doi:10.1002/adma.200602903 (2007).

[4] Snaith, H. J. *et al.* Charge collection and pore filling in solid-state dye-sensitized solar cells. *Nanotechnology* **19**, doi:10.1088/0957-4484/19/42/424003 (2008).

[5] Docampo, P. *et al.* Lessons Learned: From Dye-Sensitized Solar Cells to All-Solid-State Hybrid Devices. *Advanced Materials*, n/a-n/a, doi:10.1002/adma.201400486 (2014).

[6] Abate, A. *et al.* Lithium salts as "redox active" p-type dopants for organic semiconductors and their impact in solid-state dye-sensitized solar cells.

Physical Chemistry Chemical Physics **15**, 2572-2579, doi:10.1039/C2CP44397J (2013).

[7] Yu, W. W., Qu, L., Guo, W. & Peng, X. Experimental Determination of the Extinction Coefficient of CdTe, CdSe, and CdS Nanocrystals. *Chemistry of Materials* **15**, 2854-2860, doi:10.1021/cm034081k (2003).

[8] Huynh, W. U., Dittmer, J. J. & Alivisatos, A. P. Hybrid Nanorod-Polymer Solar Cells. *Science* **295**, 2425-2427, doi:10.1126/science.1069156 (2002).

[9] Vogel, R., Pohl, K. & Weller, H. Sensitization of highly porous, polycrystalline TiO2 electrodes by quantum sized CdS. *Chemical Physics Letters* **174**, 241-246, doi:http://dx.doi.org/10.1016/0009-2614(90)85339-E (1990).

[10] Alivisatos, A. P. Semiconductor Clusters, Nanocrystals, and Quantum Dots. *Science* **271**, 933-937, doi:10.1126/science.271.5251.933 (1996).

[11] Hodes, G. Comparison of Dye- and Semiconductor-Sensitized Porous Nanocrystalline Liquid Junction Solar Cells. *The Journal of Physical Chemistry C* **112**, 17778-17787, doi:10.1021/jp803310s (2008).

[12] Mane, R. S. & Lokhande, C. D. Thickness-dependent properties of chemically deposited Sb2S3 thin films. *Materials Chemistry and Physics* **82**, 347-354, doi:http://dx.doi.org/10.1016/S0254-0584(03)00271-2 (2003).

[13] Itzhaik, Y., Niitsoo, O., Page, M. & Hodes, G. Sb2S3-Sensitized Nanoporous TiO2 Solar Cells. *The Journal of Physical Chemistry C* **113**, 4254-4256, doi:10.1021/jp900302b (2009).

[14] Darga, A. *et al.* On Charge Carrier Recombination in Sb2S3 and Its Implication for the Performance of Solar Cells. *The Journal of Physical Chemistry C* **117**, 20525-20530, doi:10.1021/jp4072394 (2013).

[15] Wedemeyer, H. *et al.* Nanocrystalline solar cells with an antimony sulfide solid absorber by atomic layer deposition. *Energy & Environmental Science* **6**, 67-71, doi:10.1039/C2EE23205G (2013).

[16] Moon, S.-J. *et al.* Sb2S3-Based Mesoscopic Solar Cell using an Organic Hole Conductor. *The Journal of Physical Chemistry Letters* **1**, 1524-1527, doi:10.1021/jz100308q (2010).

[17] Chang, J. A. *et al.* High-Performance Nanostructured Inorganic−Organic Heterojunction Solar Cells. *Nano Letters* **10**, 2609-2612, doi:10.1021/nl101322h (2010).

[18] Chang, J. A. *et al.* Panchromatic Photon-Harvesting by Hole-Conducting Materials in Inorganic–Organic Heterojunction Sensitized-Solar Cell through the Formation of Nanostructured Electron Channels. *Nano Letters* **12**, 1863-1867, doi:10.1021/nl204224v (2012).

[19] Messina, S., Nair, M. T. S. & Nair, P. K. Antimony sulfide thin films in chemically deposited thin film photovoltaic cells. *Thin Solid Films* **515**, 5777-5782, doi:http://dx.doi.org/10.1016/j.tsf.2006.12.155 (2007).

[20] O'Mahony, F. T. F. *et al.* Low-Temperature Solution Processing of Mesoporous Metal–Sulfide Semiconductors as Light-Harvesting Photoanodes. *Angewandte Chemie International Edition* **52**, 12047-12051, doi:10.1002/anie.201305276 (2013).

[21] MoraJSeróI=fK=åK=*et al.* oÉÅçã Äáå~íáçå=áå=n ì ~åíì ã =a çí=pÉåëáíàòÉÇ=pçä~ê=` Éäæë K= *Accounts of Chemical Research* **42**I=NUQUJNURTI=ÇçáWMKSMONL~êVMMNPQÇ=HOMMVFK.

xOOz MoraJSeróI= fK= åK= C = _ áëèì ÉëíI= gK= _ êÉ~âíÜçì ÖÜè= áå= íÜÉ= a Éî Éäçéã Éåí= çÑ= pÉã áÅçåÇì Åíçê Jp Éåëáíà òÉÇ pçä~ê=` Éäæë K= *The Journal of Physical Chemistry Letters* **1**I=PMQSJPMRQI=ÇçáWMKSMONà òNMMUSPÄ=HOMNMFK.

xOPz GonzálezJPedro, V., Xu, X., MoraJSeróI=fK=åK=C = _ áëèì ÉëíI=gK=j çÇÉäáåÖ=e áÖÜJ b ÑÑáÅáÉåÅó=n ì ~åíì ã =a çí=pÉåëáíàòÉÇ=pçä~ê=` Éäæë K= *ACS Nano* **4**I=RTUPJRTVMI= ÇçáWMKSMONåå NMNRPQó=HOMNMFK.

xOQz i Ýí óJ` äÝã ÉåíI= K= qÉå~Jw~Éê~I=o K=o ó~åI=j K^ K=h ~íóI=^ K=C =e çÇÉëI=d K= ÇpÉJ pÉåëáíàòÉÇ=éJ` ì p` k Ik ~åçï áëÉ=åJwål =e ÉíÉêçàì åÅíáçåëK=*Advanced Materials* **17**I= NRNOJNRNRI=ÇçáWMKSMMOL~Çã ~HOMMQMNUQU=HOMMRFK.

xORz _ Éä~áÇãI=^ K.*et al.* fåÑäì ÉåÅÉ=çÑ=íÜÉ=äç Å~ä=~Äëçêâ Éê=ä~óÉê=íÜåÅåâåÉëë=çå=íÜÉ= éÉêÑçêã ~åÅÉ=çÑ=wål =å~åçêÇ=ëçä~ê=ÅÉäæë K=*physica status solidi (RRL) – Rapid Research Letters* **2**I=NTOJNTQI=ÇçáWMKSMMOLéëëêHOMMUMOMVO=HOMMUFK.

xOSz _ ~âÉëI=a K=o K=C h ~ã ~íI=mK=s K=mÜçíçëÉåëäáà~íáçå=çÑ=qál O=k ~åçëíêì Åì êÉë=ï áíÜ= ` Çp= n ì ~åíì ã = a çíëW m~ëíáÅì ä~íÉ= î Éêëì ë= q ì Äì ä~ê= pì éëçëí= ^ êÅÜãÉÅì êÉëK= *Advanced Functional Materials* **19**I= UMRJUNNI=ÇçáWMKSMMOL~ÇÑì HOMMUMNNTP= HOMMVFK.

xOTz h çåÖì ~å~åÇI=^ K=q î êÇóI=h K=q ~âÉÅÜãI=h K=h ì åçI=j K=C =h ~ã ~íI=mK=s K=n ì ~åíì ã = a çí=pçä~ê=` Éäæë K=q ì åáÖmÜçíçëÉëéçåëÉ=íÜêçì ÖÜ=páòÉ=~åÇ=pÜ~éÉ=` çåíêçä=çÑ= ` ÇpÉ~qál O=^ êÅÜãÉÅì êÉK=*Journal of the American Chemical Society* **130**I=QMMTJ QMNRI=ÇçáWMKSMONà~MTUOTMS=HOMMUFK.

xOUz a áÖ å~I=i K=gK=pÜÉåI=n K=h çÄ~ó~ëÜäI=gK=C =q çóçÇ~I=q K=e áÖÜ=ÉÑÑáÅáÉåÅó=çÑ= ÇpÉ= èì ~åíì ã JÇçíJëÉåëáíáòÉÇ=qáI xëì Ä=Oz=áåî ÉêëÉ=çé~ä=ëçä~ê=ÅÉäæëK=*Applied Physics Letters* **91**I=MOPNNSJMOPNNP=EOMMTFK

xOVz cÉåÖI=u K=wÜ I=h K=e ê~åâI=^ K=gK=d êáã ÉëI= K=^ K=C =j ~äæçì âI=q K=b K=o ~éáÇ= Ü~êÖÉ= qê~åëéçëí=áå=a óÉJpÉåëáíáòÉÇ=pçä~ê= Éäæë=j ~ÇÉ=Ñêçã =s ÉêíáÅ~äáó=^ äáÖåÉÇ=páåÖåÉJ ` êóëí~ä=o ì íáäÉ=qáI O=k ~åçï áêÉëK=*Angewandte Chemie International Edition* **51**I= OTOTJOTPM=ÇçáWMKNMOL~åáÉKOMNNMUMTS=EOMNOFK

xPMz qÉíêÉ~ì äíI=k K=C d ê~íòÉäI=j K=k çî Éä=å~åçëíêì Åì ëÉë=Ñçê=åÉñí=ÖÉåÉê~íçå=ÇóÉJ ëÉåëáíáòÉÇ= ëçä~ê= ÅÉäæëK= *Energy & Environmental Science* **5**I= URMSJURNSI= ÇçáWMKNMPVL Obb MPOQO_=EOMNOFK

xPNz i ÉÉI=j K=j K=qÉì ëÅÜÉêI=gK=j áó~ë~â~I=q K=j ì ê~â~ã áI=q K=k K=C =på~áÜI=e K=gK= bÑÑÅáÉåí=e óÄêáÇ=pçä~ê=` Éäæë=_~ëÉÇ=çå=j ÉëçJpì éÉêëíêì Åì êÉÇ=l êÖ~åçã Éí~ä= e ~äÇÉ=mÉêçî ëâáÉëK=*Science* **338**I=SQPJSQTI=ÇçáWMKNOSIëÅáÉåÅÉKNOOUSMQ=EOMNOFK

Chapter 6

Enhanced Photoluminescence and Device Performance via Lewis Base Passivation in Organic-Inorganic Lead Halide Perovskite Solar Cells

6.1 Broad Context

Following the philosophy of utilising absorber materials with higher optical absorption coefficients than traditional organic or organometallic dyes, I turn my attention to a family of hybrid materials known as perovskites. Photovoltaic devices based on organic-inorganic lead halide perovskites have recently taken the research community by storm, jumping from power conversion efficiencies of around 10 %[1,2] to a certified 17.9 %[3] in just over two years. One of the main reasons for this is the greatly enhanced currents that can be obtained utilising these perovskite materials. In this Chapter I will focus specifically on the mixed halide perovskite $CH_3NH_3PbI_{3-x}Cl_x$. This perovskite has a very strong, broad absorption spectrum, showing a sharp absorption onset at around 750 nm, and as such absorbs light over most of the visible spectrum.

With a band gap of 1.55 eV, this material has shown great promise as a photoactive material.

Another interesting property of this material is its ability to not only absorb most of the light in the visible spectrum, but also to transport charge.[1,4] While this fact has essentially made the use of mesoporous TiO_2 redundant, some of the best performing cells still make use of this TiO_2 layer.[5,6] Nevertheless, the ability of this material to transport charge has allowed the fabrication of highly efficient planar heterojunction solar cells which have achieved efficiencies of over 15 %.[7-9]

Recently, there have been a number of theoretical studies which suggest the presence of trap states in these perovskite materials.[10,11] It is therefore remarkable that in spite of this, these materials work so well in photovoltaic devices. It stands to reason however, that if these trap states were to be eliminated via passivation or other means, we could expect a corresponding increase in the power conversion efficiencies of these devices. In this chapter, I explore the effects of Lewis base passivation on perovskite films using photoluminescence spectroscopy, and by globally fitting to a theoretical model derive the density of trap states for passivated and unpassivated films. Finally, I show the effect of this generalised method of Lewis base passivation on the performance photovoltaic devices, as well as the stability of their output under actual operating conditions.

6.2 Introduction

As previously mentioned in Chapter 3, the term "perovskite" is applied to any member of the class of materials which have the crystal structure of calcium titanate ($CaTiO_3$) and the chemical formula ABO_3, where the A and B sites are occupied by cations. There are however, many ABO_3 compounds for which the ideal cubic structure is distorted to a lower symmetry. This is the case in the organic-inorganic metal halide perovskites; the A site is occupied by an organic cation and the B site by a divalent metal ion, while the X site is occupied by a halogen. With respect to photovoltaic energy conversion, the most well-known members of this family are the methylammonium trihalogen plumbates ($CH_3NH_3PbX_3$), where X can be either a single halogen, or a mixture of halogens. $CH_3NH_3PbI_3$ and $CH_3NH_3PbBr_3$ were first used by Miyasaka in 2009[12] as sensitizers in liquid electrolyte solar cells, achieving power conversion efficiencies of 3.5%, a method which was then later optimised by Im et al. achieving an efficiency of 6.5%. [13] However, the instability of this material in a polar, redox electrolyte catalysed the move to solid state hole transporting materials (HTMs) such as 2,2',7,7'-tetrakis(N,N-p-dimethoxy-phenylamino)-9-9'-spirobifluorene (spiro-OMeTAD).[1,2] Since 2012, research into perovskite solar cells has erupted, and the devices have evolved from a perovskite sensitised, nanostructured configuration utilising mesoporous TiO_2,[1,2,14,15] to the meso-superstructured solar cell (MSSC) configuration which makes use of an insulating material as a mesoporous scaffold, [1,16,17] to a simple planar heterojunction[8,18-20] all of which have reached reported efficiencies of over 15%. This material has also been shown to operate efficiently in the "inverted" cell architecture, achieving power conversion efficiencies of up to 15%.[15,21-25]

The perovskite crystal, like most other ionic materials, contains under-coordinated ions at its crystal surfaces and also at the grain boundaries between individual crystals.[26] There have been some theoretical studies upon the defect chemistry in these hybrid compounds.[10,11] Although defect sites can occur, for instance halide vacancies, the energy of these sites should be very close to the conduction band edge,[10,11] potentially justifying the already remarkable performance of perovskite solar cells. However, there remains much scope for further enhancement to attain the maximum performance levels.[11,27] The passivation of excess iodine ions on the surface of $CH_3NH_3PbI_{3-x}Cl_x$ crystals using the organic molecule iodopentafluorobenzene (IPFB) has recently been demonstrated.[28] An excess of charge building up at the crystal surface as a result of these under-coordinated ions, has an undesirable effect on the performance of solar cells, since it appears to result in an accumulation of photogenerated positive carriers within the hole-transporter phase at the heterojunction. This results in an increased level of recombination at this interface. It has been shown that passivating films of $CH_3NH_3PbI_{3-x}Cl_x$ with IPFB before the deposition of the HTM negates this effect, resulting in decreased recombination in these devices as compared to the unpassivated control devices. [28] However, it must be noted that this type of passivation seems not to have a direct influence upon the perovskite material itself.

From this previous study, it is now logical to ask the questions "What is the effect of under-coordinated lead ions in the crystal?" and "will directly passivating these defect states result in an improvement in material properties as well as device performance?" In an effort to answer these questions, I employ the organic Lewis bases thiophene and pyridine in an attempt to passivate the crystal surfaces of the mixed-halide lead-based perovskite $CH_3NH_3PbI_{3-x}Cl_x$ via coordinate bonding between the sulphur atom in thiophene or nitrogen atom in pyridine, and under-coordinated lead ions in the perovskite. When $CH_3NH_3PbI_{3-x}Cl_x$ films are annealed in air, one can expect the adsorption of oxygen and water on to the surface of the crystals, resulting in the

formation of lead oxide and hydroxide species,[29,30] thus in part negating the necessity for further passivation of under-coordinated Pb ions. However, it is unlikely that all, or the majority of these states would be passivated during the annealing process. Additionally, relying on atmospheric passivation by air and moisture is both uncontrolled and irreproducible, and as such, I sought to identify a controlled method of passivating defect states in this material, specifically when processed in an inert atmosphere.

In this chapter, I have investigated the feasibility and impact of Lewis base passivation of under-coordinated metals, by performing a spectroscopic, theoretical and device based study. I observe significantly inhibited non-radiative decay within the perovskite films, especially under low levels of photoexcitation. Planar heterojunction devices made utilising the passivating agents resulted in power conversion efficiencies of 15.3 % and 16.5 % for thiophene and pyridine passivated devices respectively, with average power conversion efficiencies increasing from 12 +/- 2 % to 14 +/- 1.5% and 15.5 +/- 1 % for the control, thiophene and pyridine passivated devices, respectively.

6.3 Photoluminescence Measurements

Annealing in selenium or sulphur atmosphere is a well-known passivation technique for thin film solar cells, such as copper indium gallium selenide (CIGS) and copper zinc tin sulphide (CZTS).[31-33] The sulphurisation step typically takes place after crystallisation, and serves to facilitate grain growth, as well as passivate surface states created during annealing due to sulphur losses.[33] In this case, the loss of sulphur during

the annealing process would cause unsaturated or under-coordinated metal ions, most frequently found on the surface and at the grain boundaries of crystals. It is very likely that a similar effect takes place upon annealing the perovskite.

During the annealing process, of $MAPbX_3$ perovskites, halides and methylammonium can be lost from the crystal resulting in under-coordinated Pb ions both on the crystal surface and at the grain boundaries. Recent modelling and experimental studies have shown that these under-coordinated Pb ions, and clusters in some cases, can act as electronic trap states within the perovskite material.[11,27] This under-coordination of the Pb ion results in the formation of a δ+ charge, which then creates favourable conditions for coordination, or bond formation with electron-rich molecules such as thiophene or other sufficiently weak Lewis bases. In the case of thiophene, and any such material which has a lone pair of electrons available for bonding, the electrostatic attraction between the δ+ charge on the metal and the lone pair on the sulphur atom of the thiophene, facilitates the formation of a coordinate or dative covalent bond, thus removing the excess charge and rendering the Pb atom charge neutral. This process is illustrated in **Figure 6.1** using thiophene as an example**.** **Figure 6.2** illustrates the chemical structures of the Lewis bases investigated in this study.

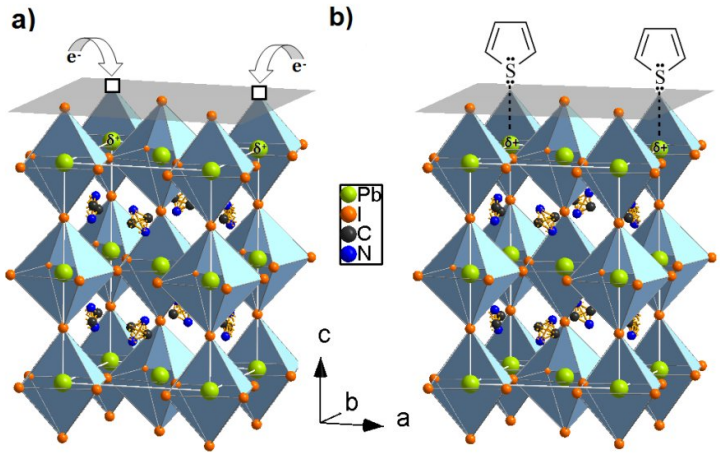

Figure 6.1: Illustration of Trap sites and the Passivation Mechanism. (a) The loss of iodine at the surface of the perovskite, leads to vacancy sites (hollow boxes) and a resulting net positive charge residing on the Pb ion (shown in green). Photogenerated electrons are then able to fall into this Coulomb trap site, thus neutralising the charge and rendering the crystal more stable. (b) Thiophene (or pyridine) molecules can donate electron density to the under-coordinated Pb atom and form a co-ordinate or dative covalent bond, effectively neutralising the excess positive charge in the crystal.

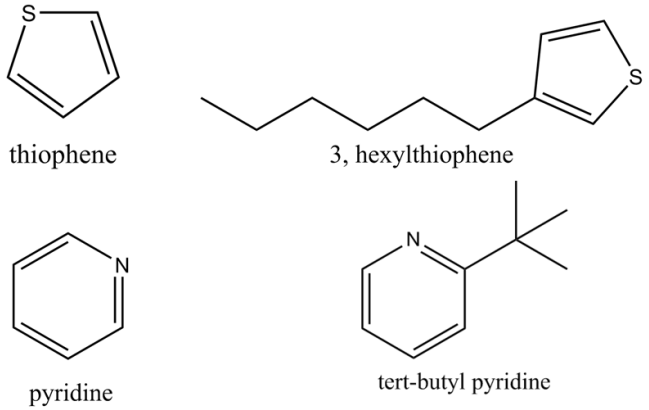

Figure 6.2: Chemical structure drawings of the Lewis bases investigated herein: thiophene, 3-hexylthiophene (3HTh), pyridine and tert-butyl pyridine (tBP).

Perovskite samples for photoluminescence spectroscopy were fabricated as outlined in Chapter 3, and the respective passivating agents were spin-coated on top of the crystal films after annealing. It is important to note that while the thiophene and the substituted thiophene were used as is, both pyridines had to be diluted to 10 vol. % in chlorobenzene before being spin-coated onto the perovskite films. This is due to the fact that pyridine is a far stronger Lewis base than thiophene with a higher polarity. As such, when these liquids are spin-coated onto the perosvkite undiluted, it results in immediate dissolution of the material. An initial investigation into the effect of these materials yielded an interesting result, in that while the thiophene and the pyridine both increased the photoluminescence lifetime of the material, both substituted molecules resulted in a quenching of the lifetime. This is perhaps indicative of the presence of some steric effect. Consequently, only the unsubstituted thiophene and pyridine molecules were further investigated. **Figure 6.3.** shows the photoluminescence lifetimes of films treated with IPFB, tBP and 3HTh as compared to an untreated film.

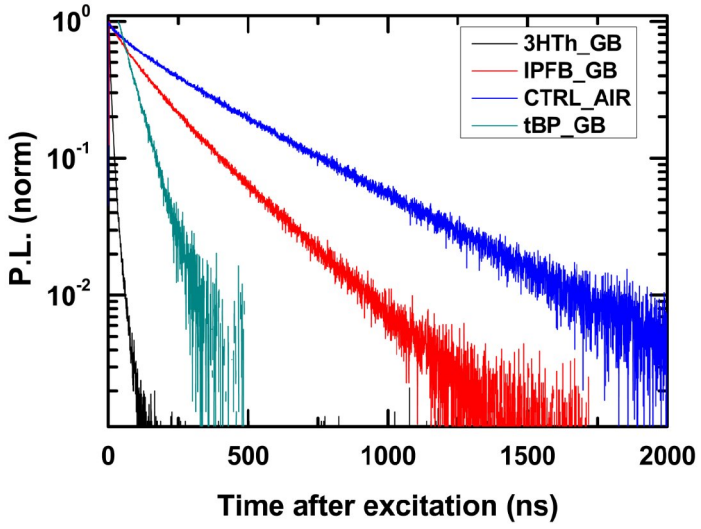

Figure 6.3: Initial photoluminescence (PL) lifetimes obtained for an untreated film (CTRL_AIR) as opposed to films treated with 3HTh, IPFB and tBP. All 3 of these surface treatments significantly decrease the PL lifetimes of the perovskite films.

Figure 6.4 shows the photoluminescence quantum efficiency (PLQE) of treated and untreated perovskite films which increases with excitation power. The rise in PLQE with fluence can be attributed to a filling of trap states, where the PLQE only reaches a peak value when the trap states responsible for non-radiative recombination are predominantly filled.[34,35] There is also an order-of-magnitude increase in the PL lifetime (Figure 6.4b) of the perovskite films, from 340.7 ± 1.1 ns to 2016.5 ± 5.3 ns when the surface is treated with pyridine, and to 2234.2 ± 4.2 ns when treated with thiophene, where the lifetimes are determined from monomolecular tail fits to the PL decays. Assuming the previously calculated diffusion coefficient of ~0.05 cm^2s^{-1}, [36] a lifetime of ~2000 ns corresponds to a diffusion length exceeding ~3 μm. For a given excitation power, there is an increased PLQE for the passivated films with respect to the control. The increased PLQE and PL lifetimes both indicate an overall reduction in the rate of non-radiative recombination within the material, and are evidence that some of the pathways to non-radiative recombination i.e., trap mediated recombination, have been substantially reduced.

The PLQE for perovskite samples treated with pyridine is also significantly higher at low excitation densities than for the samples treated with thiophene. If this rise in PLQE with excitation power is attributed to the filling of traps, this is then indicative of the fact that while both pyridine and thiophene act to passivate trap states on the surface of the perovskite material, pyridine seems to be more effective, reaching a "plateau" in PLQE at much lower excitation powers. One speculation as to the reason for this is that the pyridine may bind more strongly to the perovskite surface than the thiophene, thus more successfully reducing the degree of non-radiative recombination.

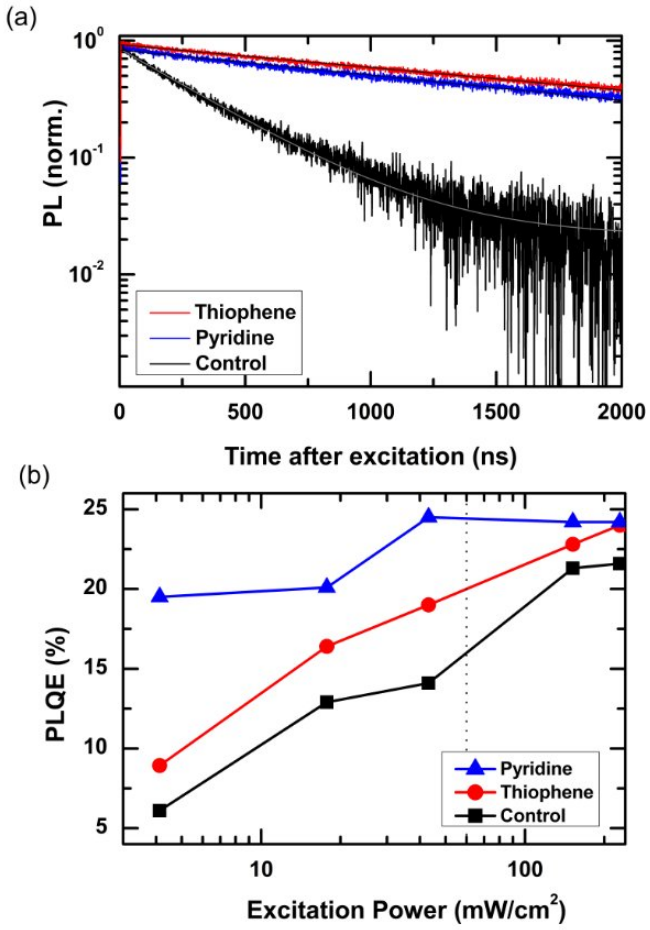

Figure 6.4: Photoluminescence characteristics of neat, thiophene and pyridine passivated $CH_3NH_3PbI_{3-x}Cl_x$ films. (a) Time-resolved photoluminescence of thiophene and pyridine passivated perovskite films as compared to unpassivated films following a 507-nm pulsed excitation (200kHz, 30nJ/cm^2/pulse). PL decays were acquired at the peak emission wavelength (780nm). Solid lines are fits to the data using mono-exponential tail fits. (b) Photoluminescence quantum efficiency (PLQE) of unpassivated films and films treated with thiophene and pyridine as a function of 532 CW laser excitation intensity. The dashed line shows the equivalent intensity to 1 sun illumination, approximately corresponding to the pulse excitation density in (a). PLQE measurements were taken by Elizabeth Parrott of the Department of Physics, University of Oxford.

The results have been globally fitted to a model describing photoluminescence in the perovskites and the trap density of the untreated film has been found to be 3.5 x 10^{16} cm^{-3}. For the thiophene passivated film however, this trap density is decreased threefold yielding a trap density of 1.0 x 10^{16} cm^{-3}, while for the pyridine passivated film, the extracted trap density is decreased by an order of magnitude, resulting in a trap density of 0.2 x 10^{16} cm^{-3}. These results are shown in **Figure 6.5**. This is hence consistent with both the thiophene and pyridine treatments effectively passivating electronic trap sites in the organo lead halide perovskites.

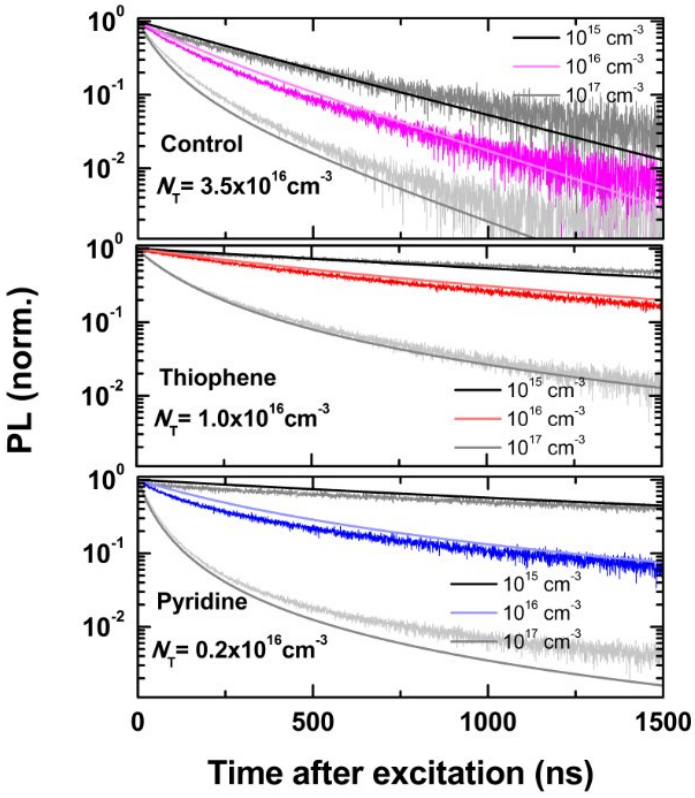

Figure 6.5: Photoluminescence Characteristics of Bare and Thiophene or Pyridine Passivated Films. Time-resolved PL measurements of control, thiophene and pyridine samples with 507-nm pulsed (200kHz) excitation at a range of pulse fluences corresponding to the quoted photoexcitation densities. Solid lines are fits to the data using the model described by

Stranks et al.,[35] allowing extraction of the quoted trap densities N_T. PL measurements taken by Dr. Samuel D. Stranks and Elizabeth Parrott of the Department of Physics, University of Oxford, and model fits for this data were done by Dr. Victor M. Burlakov of the Department of Mathematics, University of Oxford.

6.4 Device Performance

Having shown spectroscopic data which is consistent with thiophene or pyridine molecules passivating non-radiative decay sites in the perovskite absorber, here I present solution processed planar heterojunction solar cells, fabricated according to literature.[16,18,19] The mixed halide perovskite precursor solution (40 wt% in DMF) was spin-coated onto fluorine doped tin oxide (FTO) substrates coated with a compact layer of TiO_2 and annealed under inert atmosphere. Full experimental detail is given in Chapter 3. The passivating agent was then spin-coated onto the fully crystallised perovskite coated substrates before the deposition of the HTM. The devices were completed with Au cathodes. The solar cell parameters of the best performing devices are shown in **Table 6.1**, while the respective current-voltage characteristics are given in **Figure 6.6**.

	J_{sc} (mA/cm^2)	V_{oc} (V)	η (%)	FF (a.u.)	η_{MPP} (%)	J_{MPP} (mA/cm^2)	η_{MPP}/η
Control	20.7	0.95	13.1	0.68	8.3	11.8	0.63
Thiophene	21.3	1.02	15.3	0.68	14.1	20.8	0.92
Pyridine	24.1	1.05	16.5	0.72	15.5	21.3	0.94

Table 6.1: Performance parameters of best control and passivated devices. Device performance parameters for the champion devices (treated and untreated), along with the

stabilised efficiency (η_{MPP}) and current values (J_{MPP}), as well as the ratio of the stabilised efficiency to the efficiency of the best scan.

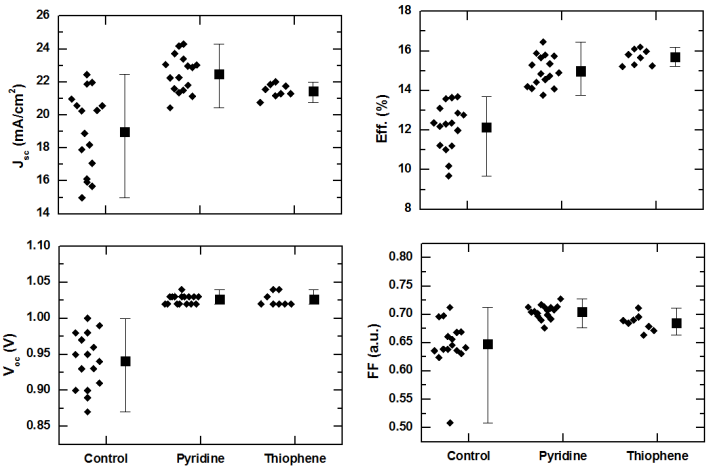

Figure 6.6: Performance parameters of a batch of planar heterojunction solar cells. Solar cell performance parameters extracted from JV curves measured under AM1.5 simulated sun light of 100mWcm-2 equivalent irradiance of a batch of devices. We see that the thiophene and pyridine treated devices consistently outperform the untreated devices in every performance parameter. Notably, the treated devices have consistently higher currents and voltages than are observed in the untreated devices and a much narrower spread in values.

It can be clearly seen from the device statistics (**Figure 6.6**) that utilising both thiophene and pyridine as surface passivating agents dramatically improves the reproducibility of the devices. The average performance of both thiophene and pyridine treated devices consistently outperform the untreated control devices. Of the treated devices, pyridine passivated devices consistently achieve even higher photocurrents and fill factors than those treated with thiophene. Utilising the surface treatments on planar heterojunction solar cells, there is an increase in the maximum power conversion efficiency from 13.1% to 15.3% with thiophene passivation and to 16.5 % with pyridine

passivation. These results represent the highest reported efficiencies for planar heterojunction perovskite solar cells fabricated using a single step solution deposition method.

It is frequently observed that perovskite solar cells in the conventional sensitised or meso-superstructured configuration exhibit hysteresis in the current-voltage curves, however little is known about the source of this phenomena.[37,38] It has recently been shown that though hysteresis is present in these devices, it is possible to achieve both stabilised current and efficiency from the MSSC which is close to that of the best scan. Interestingly, in the case of the planar heterojunction devices, the stabilised power output is typically around half of what can be achieved via a fast scan.[38] **Figures 6.7b**, **c** and **d**, show the stabilised power output of the best devices from this study, by holding them at their maximum power point voltage under simulated AM 1.5 illumination and measuring the photocurrent and efficiency for 2 minutes.

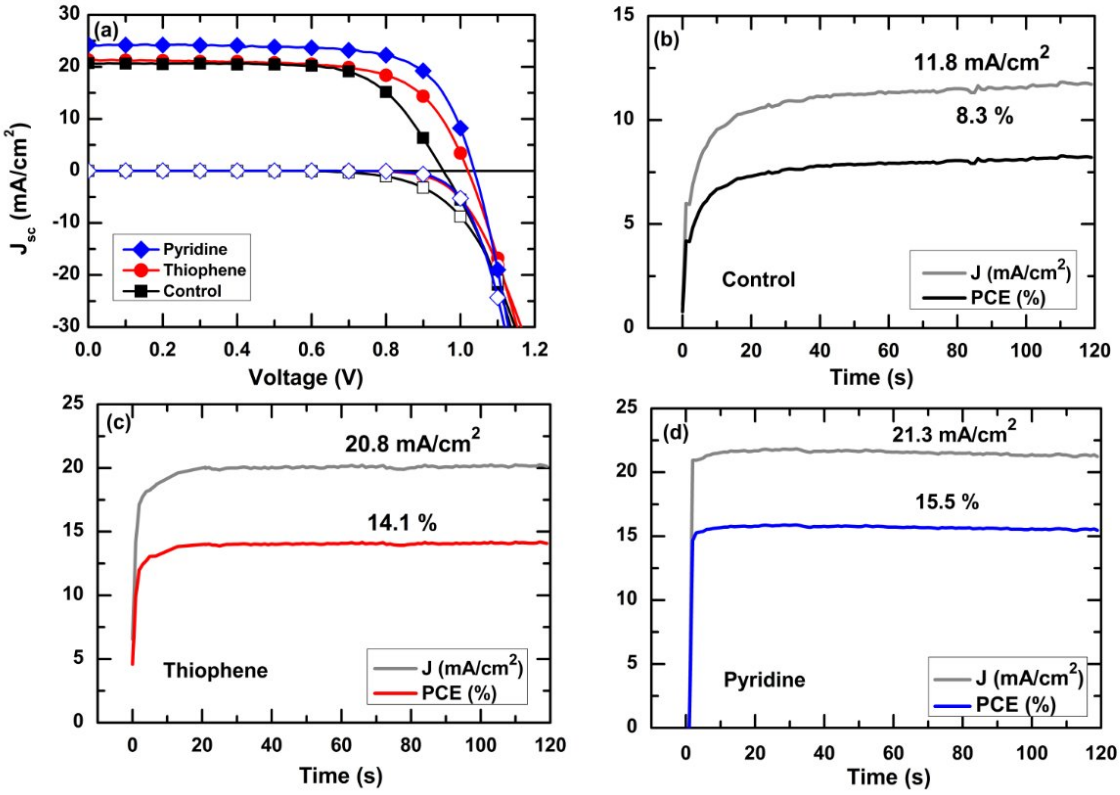

Figure 6.6: Current-Voltage Characteristics. (a) Current-voltage (JV) characteristics for the best control (black squares), thiophene (red circles) and pyridine (blue diamonds) passivated devices. The power conversion efficiency of the control device is 13.1% and the passivated devices are 15.3% (thiophene) and 16.5% (pyridine) under full sun illumination. Dark JV curves are illustrates with hollow symbols. (b) Stabilised efficiency of control, (c) thiophene and (d) pyridine passivated devices, measured by holding the device at its maximum power point for 120 seconds.

Encouragingly, the stabilised power output is much improved in the case of the pyridine and thiophene treated devices with respect to the control, resulting in a stabilised power conversion efficiency which closely approaches that of the fast scan. For the untreated device, the fast scan produces an efficiency of 13.1 % which then stabilised at 8.3%, whereas for the thiophene passivated device, the fast scan produces an efficiency of 15.3 % which stabilises at 14.1 % and for the pyridine treated device

16.5 % which has a stabilised output at 15.5 %. If the photocurrent rise time is defined to be the time taken to reach 95 % of the maximum stabilised power output, the rise time reduces from 40 s, to 12 s for the control and thiophene devices respectively and even less time for the pyridine treated device. This is consistent with an increased ability to rapidly fill all the defect sites in the passivated films, since the density of non-radiative recombination sites is reduced.

6.5 Summary and Outlook

In conclusion, by utilising Lewis base surface treatments on $CH_3NH_3PbI_{3-x}Cl_x$ perovskite films, I have demonstrated a controlled method of defect passivation via coordinate bonding. These surface treatments appear to have the effect of reducing the density of electronic trap sites within the material, which I have postulated to be due to the presence of under-coordinated metal atoms in the perovskite crystal. By using thiophene and pyridine passivation a quantitative and systematic decrease of defect states has been shown, as opposed to the random and irreproducible nature of atmospheric passivation by oxygen and/or small amounts of moisture. I have proposed a mechanism for this type of electrical passivation in the form of co-ordinate or dative covalent bonding from electron-rich molecules, and have shown a decrease in the rate of non-radiative recombination in perovskite films. This study also confirms the finding of recent theoretical and experimental papers, which suggest via modelling and EPR measurements that there are iodine vacancies in the perovskite lattice which result in the presence of under-coordinated Pb atoms.[11,14,27]

By passivating these defect states which can act as electron traps within the material, there is not only a resultant increase in the efficiency of planar heterojunction solar cells from 13% to 15.3% and 16.5 % using thiophene and pyridine treatments respectively, but even more significantly a massive improvement in the stabilised power output for this solar cell architecture. While this method of passivation is expected to be generally applicable to all types of organic-inorganic perovskite based photovoltaics, further insight must be gained into the nature of all possible trap states within these materials, and effort placed into passivation of most or all of these defect states, before maximum performance is to be achieved.

Further work will also involve the investigation of the variation in trap density produced by different methods of depositing this material. It may well be that the density of trap states present in perovskite materials produced by methods which do not require annealing such as; sequential deposition,[5] sequential spin-coating,[25] and vapour deposition[7,24] have a significantly decreased percentage of under-coordinated Pb atoms, and therefore require less passivation in order to achieve high performance and consistent operation under maximum power point conditions. Beyond use in solar cells, this passivation technique is likely to prove useful for many other perovskite based optoelectronic applications such as lasers and LEDs.

6.6 References

[1] Lee, M. M., Teuscher, J., Miyasaka, T., Murakami, T. N. & Snaith, H. J. Efficient Hybrid Solar Cells Based on Meso-Superstructured Organometal Halide Perovskites. *Science* **338**, 643-647, doi:10.1126/science.1228604 (2012).

[2] Kim, H.-S. *et al.* Lead Iodide Perovskite Sensitized All-Solid-State Submicron Thin Film Mesoscopic Solar Cell with Efficiency Exceeding 9%. *Sci. Rep.* **2**, doi:http://www.nature.com/srep/2012/120821/srep00591/abs/srep00591.html#supplementary-information (2012).

[3] (NREL), N. R. E. L. *NREL*, <www.nrel.gov/ncpv/images/efficiency_chart.jpg> (2014).

[4] Bi, D. *et al.* Using two-step deposition technique to prepare perovskite (CH3NH3PbI3) for thin film solar cells based on ZrO2 and TiO2 mesostructures. *RSC Advances*, doi:10.1039/C3RA43228A (2013).

[5] Burschka, J. *et al.* Sequential deposition as a route to high-performance perovskite-sensitized solar cells. *Nature* **499**, 316-319, doi:10.1038/nature12340 http://www.nature.com/nature/journal/v499/n7458/abs/nature12340.html#supplementary-information (2013).

[6] Noh, J. H., Im, S. H., Heo, J. H., Mandal, T. N. & Seok, S. I. Chemical Management for Colorful, Efficient, and Stable Inorganic–Organic Hybrid Nanostructured Solar Cells. *Nano Letters* **13**, 1764-1769, doi:10.1021/nl400349b (2013).

[7] Liu, M., Johnston, M. B. & Snaith, H. J. Efficient planar heterojunction perovskite solar cells by vapour deposition. *Nature* **501**, 395-398, doi:10.1038/nature12509 (2013).

[8] Liu, D. & Kelly, T. L. Perovskite solar cells with a planar heterojunction structure prepared using room-temperature solution processing techniques. *Nat Photon* **8**, 133-138, doi:10.1038/nphoton.2013.342 http://www.nature.com/nphoton/journal/v8/n2/abs/nphoton.2013.342.html#supplementary-information (2014).

[9] Eperon, G. E., Burlakov, V. M., Docampo, P., Goriely, A. & Snaith, H. J. Morphological Control for High Performance, Solution-Processed Planar Heterojunction Perovskite Solar Cells. *Advanced Functional Materials* **24**, 151-157, doi:10.1002/adfm.201302090 (2014).

[10] Kim, J., Lee, S.-H., Lee, J. H. & Hong, K.-H. The Role of Intrinsic Defects in Methylammonium Lead Iodide Perovskite. *The Journal of Physical Chemistry Letters* **5**, 1312-1317, doi:10.1021/jz500370k (2014).

[11] Yin, W.-J., Shi, T. & Yan, Y. Unusual defect physics in CH3NH3PbI3 perovskite solar cell absorber. *Applied Physics Letters* **104**, -, doi:doi:http://dx.doi.org/10.1063/1.4864778 (2014).

[12] Kojima, A., Teshima, K., Shirai, Y. & Miyasaka, T. Organometal Halide Perovskites as Visible-Light Sensitizers for Photovoltaic Cells. *Journal of the American Chemical Society* **131**, 6050-6051, doi:10.1021/ja809598r (2009).

[13] Im, J.-H., Lee, C.-R., Lee, J.-W., Park, S.-W. & Park, N.-G. 6.5% efficient perovskite quantum-dot-sensitized solar cell. *Nanoscale* **3**, 4088-4093, doi:10.1039/C1NR10867K (2011).

[14] Chang, J. A. *et al.* Panchromatic Photon-Harvesting by Hole-Conducting Materials in Inorganic–Organic Heterojunction Sensitized-Solar Cell through the Formation of Nanostructured Electron Channels. *Nano Letters* **12**, 1863-1867, doi:10.1021/nl204224v (2012).

[15] You, J. *et al.* Low-Temperature Solution-Processed Perovskite Solar Cells with High Efficiency and Flexibility. *ACS Nano* **8**, 1674-1680, doi:10.1021/nn406020d (2014).

[16] Ball, J. M., Lee, M. M., Hey, A. & Snaith, H. Low-Temperature Processed Mesosuperstructured to Thin-Film Perovskite Solar Cells. *Energy & Environmental Science* (2013).

[17] Bi, D. *et al.* Using a two-step deposition technique to prepare perovskite (CH3NH3PbI3) for thin film solar cells based on ZrO2 and TiO2 mesostructures. *RSC Advances*, doi:10.1039/C3RA43228A (2013).

[18] Eperon, G. E., Burlakov, V. M., Docampo, P., Goriely, A. & Snaith, H. J. Morphological Control for High Performance, Solution-Processed Planar Heterojunction Perovskite Solar Cells. *Advanced Functional Materials*, n/a-n/a, doi:10.1002/adfm.201302090 (2013).

[19] Eperon, G. E. *et al.* Formamidinium lead trihalide: a broadly tunable perovskite for efficient planar heterojunction solar cells. *Energy & Environmental Science* **7**, 982-988, doi:10.1039/C3EE43822H (2014).

[20] Liu, M., Johnston, M. B. & Snaith, H. J. Efficient planar heterojunction perovskite solar cells by vapour deposition. *Nature* **advance online publication**, doi:10.1038/nature12509 (2013).

[21] Docampo, P., Ball, J. M., Darwich, M., Eperon, G. E. & Snaith, H. J. Efficient organometal trihalide perovskite planar-heterojunction solar cells on flexible polymer substrates. *Nat Commun* **4**, doi:10.1038/ncomms3761 (2013).

[22] Jeng, J.-Y. *et al.* CH3NH3PbI3 Perovskite/Fullerene Planar-Heterojunction Hybrid Solar Cells. *Advanced Materials* **25**, 3727-3732, doi:10.1002/adma.201301327 (2013).

[23] Wang, Q., Dong, Q., Xiao, Z., Yuan, Y. & Huang, J. Large Fill-Factor Bilayer Iodine Perovskite Solar Cells Fabricated by Low-Temperature Solution-Process. *Energy & Environmental Science*, doi:10.1039/C4EE00233D (2014).

[24] Malinkiewicz, O. *et al.* Perovskite solar cells employing organic charge-transport layers. *Nat Photon* **8**, 128-132, doi:10.1038/nphoton.2013.341 http://www.nature.com/nphoton/journal/v8/n2/abs/nphoton.2013.341.html#supplementary-information (2014).

[25] Xiao, Z. *et al.* Efficient, high yield perovskite photovoltaic devices grown by interdiffusion of solution-processed precursor stacking layers. *Energy & Environmental Science*, doi:10.1039/C4EE01138D (2014).

[26] Skromme, B. J., Sandroff, C. J., Yablonovitch, E. & Gmitter, T. Effects of passivating ionic films on the photoluminescence properties of GaAs. *Applied*

Physics Letters **51**, 2022-2024, doi:doi:http://dx.doi.org/10.1063/1.98280 (1987).

[27] Shkrob, I. A. & Marin, T. W. Charge Trapping in Photovoltaically Active Perovskites and Related Halogenoplumbate Compounds. *The Journal of Physical Chemistry Letters* **5**, 1066-1071, doi:10.1021/jz5004022 (2014).

[28] Abate, A. *et al.* Supramolecular Halogen Bond Passivation of Organic–Inorganic Halide Perovskite Solar Cells. *Nano Letters*, doi:10.1021/nl500627x (2014).

[29] Itzhaik, Y., Niitsoo, O., Page, M. & Hodes, G. Sb2S3-Sensitized Nanoporous TiO2 Solar Cells. *The Journal of Physical Chemistry C* **113**, 4254-4256, doi:10.1021/jp900302b (2009).

[30] Roe, A. L. *et al.* In situ x-ray absorption study of lead ion surface complexes at the goethite-water interface. *Langmuir* **7**, 367-373, doi:10.1021/la00050a029 (1991).

[31] Mitzi, D. B., Gunawan, O., Todorov, T. K., Wang, K. & Guha, S. The path towards a high-performance solution-processed kesterite solar cell. *Solar Energy Materials and Solar Cells* **95**, 1421-1436, doi:http://dx.doi.org/10.1016/j.solmat.2010.11.028 (2011).

[32] Hlaing Oo, W. M. *et al.* Grain Size and Texture of Cu2ZnSnS4 Thin Films Synthesized by Cosputtering Binary Sulfides and Annealing: Effects of Processing Conditions and Sodium. *Journal of Elec Materi* **40**, 2214-2221, doi:10.1007/s11664-011-1729-3 (2011).

[33] Khalkar, A., Lim, K.-S., Yu, S.-M., Patole, S. P. & Yoo, J.-B. Effect of Growth Parameters and Annealing Atmosphere on the Properties of Cu2ZnSnS4 Thin Films Deposited by Cosputtering. *International Journal of Photoenergy* **2013**, 7, doi:10.1155/2013/690165 (2013).

[34] Deschler, F. *et al.* High Photoluminescence Efficiency and Optically Pumped Lasing in Solution-Processed Mixed Halide Perovskite Semiconductors. *The Journal of Physical Chemistry Letters* **5**, 1421-1426, doi:10.1021/jz5005285 (2014).

[35] Stranks, S. D., Burlakov, V. M., Leijtens, T., Ball, J. M., Goriely, A., Snaith, H. J (2014). *Photoluminescence from Organometal Halide Perovskites: Excitons, Free Charge and Mid-Gap Electronic States.* Submitted work (2014).

[36] Stranks, S. D. *et al.* Electron-Hole Diffusion Lengths Exceeding 1 Micrometer in an Organometal Trihalide Perovskite Absorber. *Science* **342**, 341-344, doi:10.1126/science.1243982 (2013).

[37] Dualeh, A. *et al.* Impedance Spectroscopic Analysis of Lead Iodide Perovskite-Sensitized Solid-State Solar Cells. *ACS Nano* **8**, 362-373, doi:10.1021/nn404323g (2013).

[38] Snaith, H. J. *et al.* Anomalous Hysteresis in Perovskite Solar Cells. *The Journal of Physical Chemistry Letters*, 1511-1515, doi:10.1021/jz500113x (2014).

Chapter 6: Enhanced Photoluminescence and Device Performance via Lewis Base Passivation in Organic-Inorganic Lead Halide Perovskite Solar Cells

Chapter 7

Lead-Free Organic-Inorganic Tin Halide Perovskites for Photovoltaic Applications

The results reported in this chapter have been published in:

(1) Noel, N. K.; Stranks, S. D.; Abate, A., Wehrenfennig, C.; Guarnera, S.; Haghighirad, A.; Sadhanala, A.; Eperon, G. E.; Pathak, S. K.; Johnston, M. B.; Petrozza, A.; Herz, L.; Snaith, H. J. Lead-Free Organic-Inorganic Tin Halide Perovskites for Photovoltaic Applications. Energy Environ. Sci., 2014, Accepted Manuscript, doi: 10.1039/C4EE01076K.

7.1 Broad Context

In the previous chapter organic-inorganic lead halide perovskites were introduced as viable competitors for crystalline silicon with respect to power conversion efficiency. The current solar industry is dominated by crystalline silicon, which converts sun light to electrical energy at around 25 % efficiency (laboratory scale devices) while lead-based perovskite solar cells currently stand at over 17 %.[1] The cost

of silicon PV has dropped considerably over the last 5 years, and is rapidly approaching the cost of generating electricity from fossil fuels. However, PV will only emerge as the primary power source if the cost can be lowered further to become cheaper than generating electricity from coal.

Organic-inorganic crystalline perovskite materials have in the last two years proliferated the PV research community and solar cells based on these materials promise to reach the same efficiencies as crystalline silicon, but at a fraction of the cost. However, the presence of lead in the semiconductor has raised questions as to whether toxicology issues will become problematic for widespread deployment of this technology in the future. The most likely substitute is tin, which like lead, is also a group 14 metal. While organic-inorganic tin halide perovskites have shown good semiconducting behaviour, the instability of tin in its 2+ oxidation state has thus far proved to be an overwhelming challenge. In this chapter, I report the first completely lead-free, $CH_3NH_3SnI_3$ perovskite solar cell processed on a mesoporous TiO_2 scaffold, reaching efficiencies of over 6% under 1 sun illumination. Remarkably, these devices can achieve open circuit voltages over 0.88 V from an absorber material which has a 1.23 eV band gap.

In this chapter, I present the operation of the first efficient prototype of an entirely lead-free perovskite solar cell, illustrating that impressive photovoltaic operation is not necessarily unique to lead-based devices, and perhaps beckoning even higher efficiencies for non-toxic, abundant low cost solar cells.

7.2 Introduction

For many years there has been a concerted effort to find a cheaper alternative to silicon solar cells. Over the past two years, perovskite-based solar cells have been developed and have rapidly passed the efficiencies of many emerging and commercial photovoltaics, such as dye-sensitised,[2] organic and amorphous silicon solar cells.[3] As shown in Chapter 7, lead-based perovskite solar cells are promising alternatives to silicon, having both cheap and abundant starting materials and being able to be manufactured by simple solution processing,[4-6] or scalable vapour phase deposition.[7,8]

However, one major concern with this material is the toxicity of lead, and as such, a key scientific challenge is to replace the lead ion in the perovskite crystal with a less toxic metal, but there is only one other report of successfully replacing the lead ion, whilst retaining respectable photovoltaic performance.[9] The most viable replacements for lead in the perovskite material are Sn and Ge, also members of the group 14 metals. However, it is well known that the stability of the 2+ oxidation state decreases when moving up the group 14 elements, thus the major problem with the use of these metals is their chemical instability in the required oxidation state. Sn-based perovskites in particular, have shown excellent mobilities in transistors,[10] but can also be intentionally or unintentionally doped to become metallic.[11,12] It has been demonstrated that when the Sn^{2+} ion is oxidised to Sn^{4+}, the Sn^{4+} acts as a p-type dopant within the material in a process referred to as "self-doping".[11]

To the best of my knowledge, there exists no previous report of a completely lead-free, Sn-based perovskite solar cell. A recent study by Ogimi *et al.* reported a mixed metal, Sn-Pb perovskite which allowed tunability of bandgap of the perovskite absorber by varying the Sn:Pb ratio, indicating that Sn could be a good choice of metal ion, especially for lower band gap solar cells.[13] However, the same study reported that the neat methylammonium tin triiodide ($CH_3NH_3SnI_3$) perovskite does not exhibit

significant photovoltaic properties, and that a minimum content of Pb is needed to stabilize Sn in its 2+ oxidation state.

This chapter presents the material and solar cell characterisation of photovoltaic devices employing the completely lead-free perovskite, $CH_3NH_3SnI_3$, as the photoactive material. Encapsulation of this material under inert atmosphere has allowed the characterisation of the films and enabled the probing of their performance in solar cells. I have obtained devices which yield power conversion efficiencies of greater than 6% under simulated full sunlight. Additionally the THz mobility and charge-carrier lifetime has been derived. These results indicate that with reduction of the hole-doping density and further optimisation, this material should prove to be a viable, completely non-toxic alternative to Pb-based perovskite solar cells, with the potential to deliver even higher efficiencies. Importantly, this demonstrates that Pb-based materials are not unique in delivering efficient perovskite solar cells.

7.3 X-Ray Diffraction Measurements

A ground powder sample for XRD measurements was prepared by grinding equimolar quantities of methylammonium iodide (MAI) and SnI_2 (anhydrous, Sigma Aldrich) in inert atmosphere. Upon grinding, the black $CH_3NH_3SnI_3$ was formed. This powder was then sealed under nitrogen, between two pieces of Kapton polyimide film. The powder XRD measurement was then done maintaining the nitrogen atmosphere of the sample. The diffractogram and crystal structure of the material is shown in **Figure 7.1**. The diffraction pattern obtained is in good agreement with simulated and literature data, and corresponds to the tetragonal conformation of the perovskite structure.[14] The structure is identical to that of the more widely used $CH_3NH_3PbX_3$ perovskite,[5,15] showing that in this case, changing the central metal atom

has not affected the overall crystal structure of the material. The lattice parameters derived from the X-Ray diffractogram were a = 8.7912 Å and c = 4.4770 Å.

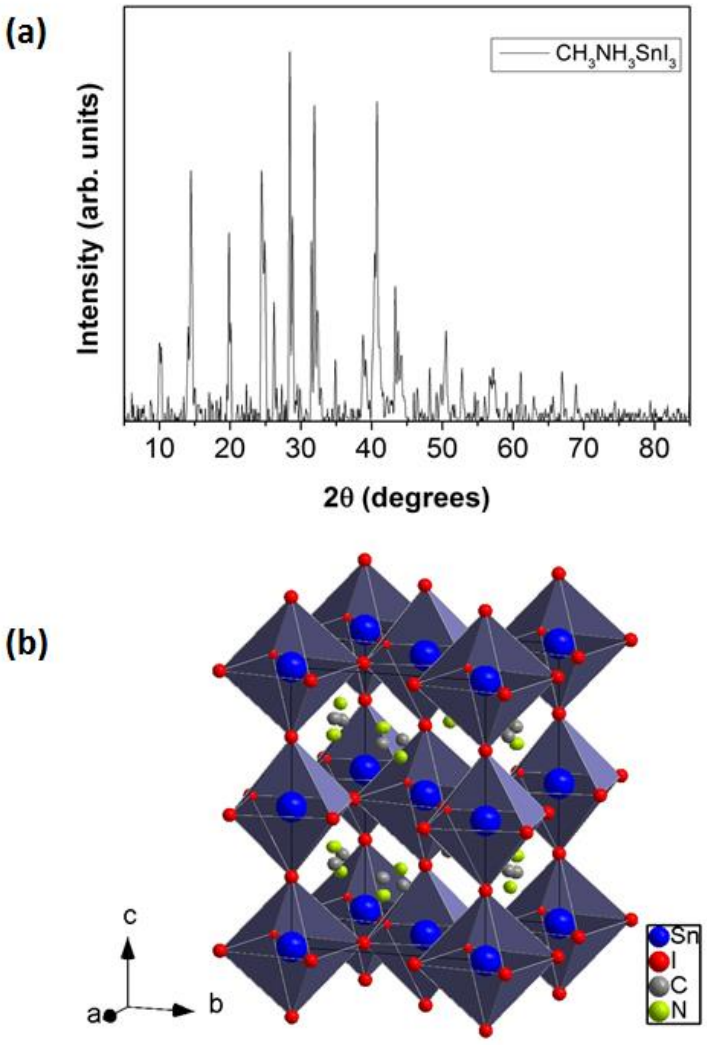

Figure 7.1: (a) XRD pattern derived from a ground powder sample of $CH_3NH_3SnI_3$. (b) Simulated crystal structure of $CH_3NH_3SnI_3$ obtained from the diffraction pattern given in (a) showing the tetragonal conformation of the perovskite lattice. This measurement was taken by Dr. Amir Abbas Haghighirad of the Department of Physics, University of Oxford.

A precursor solution of $CH_3NH_3SnI_3$ was then prepared under inert atmosphere as previously outlined in Chapter 3 and spin coated on a glass substrate which was coated with 80 nm of mesoporous Al_2O_3. Upon spin coating in the nitrogen filled glovebox, the perovskite formed a black crystalline film without any further heating required. However, when this film was removed from the glovebox and placed under ambient conditions, there was almost an immediate decolouration of the film which became white with a slight brown hue. XRD was then performed on this film and the diffractogram which was obtained is shown in **Figure 7.2**. The pattern obtained was found to correspond to that of MAI with some impurity peaks present. The lattice parameters which were derived were such that a = b =11.2246 Å and c = 8.9362 Å.

It is likely that due to the inherent instability of the Sn^{2+} ion, when exposed to oxygen and/or moisture this species is oxidised to its more stable analogue, Sn^{4+}. As such, when the $CH_3NH_3SnI_3$ perovskite is brought out into ambient conditions, this oxidation of the Sn^{2+} will likely cause the degradation of the structure leaving MAI and possibly oxides or hydroxides of the Sn (IV) species. Interestingly, no oxides of Sn are observed in the XRD pattern of the degraded sample. This may be due to the formation of amorphous species with a very small domain size which would not be clearly seen through this method of analysis. As a result of the instability of this material, all subsequent measurements were carried out on samples which were either sealed, or investigated under vacuum.

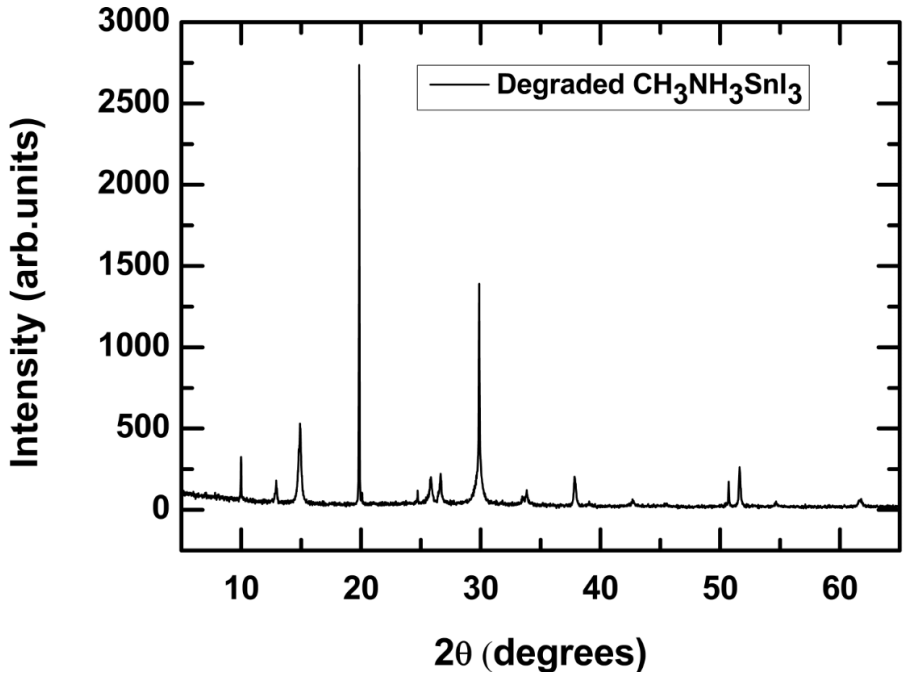

Figure 7.2: XRD pattern of a degraded thin film sample of $CH_3NH_3SnI_3$. The peaks of this diffractogram correspond to the crystal structure of methylammonium iodide with some impurities. The lattice parameters are given by a = b =11.2246 Å and c = 8.9362 Å. This measurement was taken by Giles E. Eperon of the Department of Physics, University of Oxford.

7.4 Optical Characterization

Optical characterisation of this material was done on thin films prepared by spin coating the $CH_3NH_3SnI_3$ precursor solution onto the desired substrate under inert atmosphere. In the case of the substrates for photoluminescence (PL) and absorption spectroscopy, the substrates used were Al_2O_3 coated (80 nm) glass. After the formation of the $CH_3NH_3SnI_3$, the samples were encapsulated under nitrogen atmosphere using a glass slide with a meltable polymer and an epoxy resin in order to prevent degradation of the samples under ambient conditions. For the photothermal deflection spectroscopy (PDS) studies the precursor solution was directly spin coated onto quartz substrates and

thereafter immersed in an inert liquid in order to do the measurement. This prevented the samples from any degradation.

The optical characterization of the material is shown in **Figure 7.3**. The optical absorption characteristics of the material shows a broad absorption edge at approximately 1000 nm and a broad photoluminescence peak at 980 nm. In comparison, the lead perovskite, $CH_3NH_3PbI_{3-x}Cl_x$, shows a sharper absorption edge at 770 nm, and a narrower emission spectrum which has been recently shown to be homogeneously broadened.[16] The steady-state absorption spectra were acquired with a Perkin-Elmer Lambda 1050 UV/Vis/NIR spectrophotometer using an integrating sphere to account for reflection and scattering. It must be noted however that the films were located on the front and back of the integrating sphere for the transmission and reflection measurements and severe scattering out of the sides of the sealed substrates escapes the integrating sphere, and will hence erroneously appear as an absorption signal. As such, correctly estimating the band gap of the material from the absorption spectrum is quite difficult. In order to provide a good estimation of the band gap of the $CH_3NH_3SnI_3$ perovskite, photo-thermal deflection spectroscopy (PDS) was employed.[17] Figure 7.3b shows the absorption profile extracted from the PDS measurements. The Tauc plot shown in the inset shows a sharp band edge at 1.23 eV.

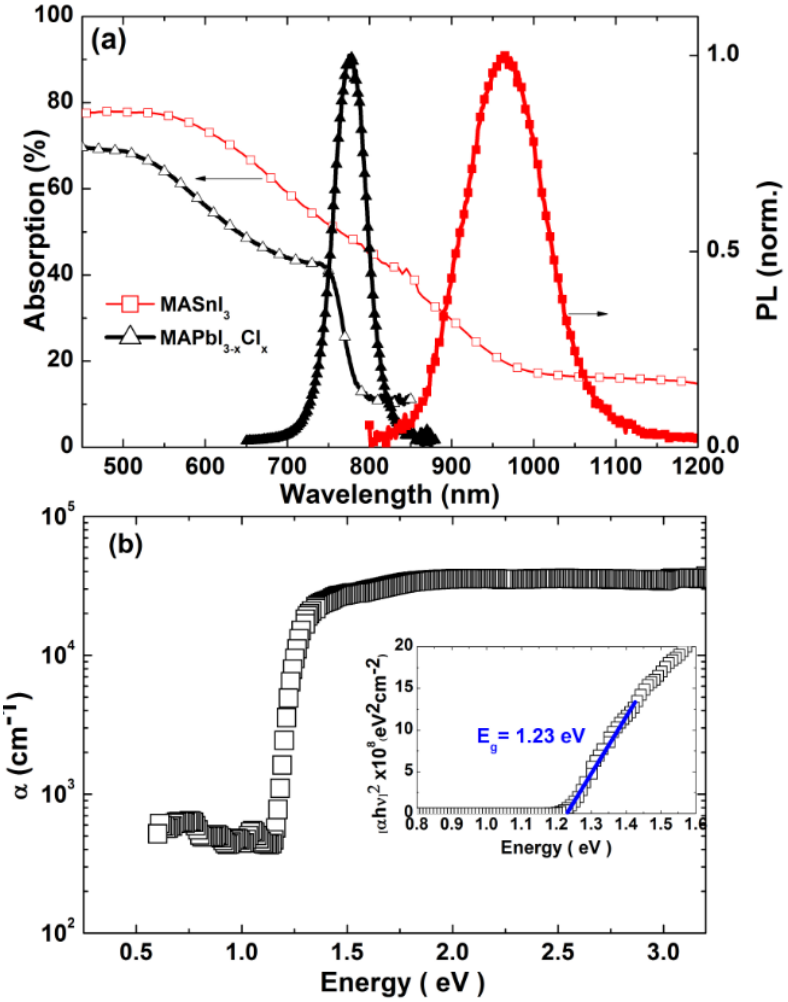

Figure 7.3: (a) Normalized steady state photoluminescence (PL) with photoexcitation at 500 nm, and absorption taken with reflectance and transmission employing an integrating sphere of the tin-based and lead-based perovskites $CH_3NH_3SnI_3$ and $CH_3NH_3PbI_{3-x}Cl_x$ respectively. (b) The absorption profile of $CH_3NH_3SnI_3$ as determined through photo-thermal deflection spectroscopy (PDS), with the band gap of the material determined using the Tauc plot (shown in inset).[18] It must be noted that since there may be strong exciton absorption at the band edge, the Tauc plot determined band gap can only be considered as an estimate. PL measurements were taken in collaboration with Dr. Samuel D. Stranks of the Department of Physics, University of Oxford. Absorption measurements were taken by Simone Guarnera of the Italian Institute of Technology. PDS measurements were taken by Aditya Sadhanala of the Department of Physics, University of Cambridge.

7.5 Terahertz Spectroscopy

To probe the photophysical properties of $CH_3NH_3SnI_3$ in more detail time resolved optical pump THz probe spectroscopy was performed. This provides a contactless probe for the conductivity of the material at picosecond time-resolution. A single-cycle THz pulse is incident on the sample at a well-defined time-delay, after being photoexcited by a 40 fs laser pulse at 550 nm. By recording the photoinduced change of the transmitted THz amplitude, the transient conductivity of the thin-film sample can be reconstructed, and by knowing the photoexcitation density from the visible pulse, the effective charge carrier mobility can be extracted.[19] The derivation of the photoconductivity and the charge carrier mobility are described below.

The sheet photoconductivity ΔS of a thin film between two media of refractive indices n_A and n_B, under the condition that the thickness of the film is much smaller than the THz wavelength, may be expressed as in **Equation 7.1**.[20,21]

$$\Delta S = -\epsilon_0 c\,(n_A + n_B)\left(\frac{\Delta T}{T}\right) \tag{7.1}$$

where $\Delta T = T_{\text{illuminated}} - T$ is the photoinduced change in terahertz electric field. Here, T and $T_{\text{illuminated}}$ are the transmitted terahertz electric fields of the sample in the dark and after photoexcitation respectively. In this experiment the sample film is surrounded by vacuum from one side, hence $n_A = 1$ and in contact with the z-cut quartz substrate with THz-refractive index $n_B = 2.13$ from the other side. In order to derive the charge-carrier mobility μ from the photoinduced sheet conductivity, the number of photo-excited charge carriers N needs to be determined. This can be done by using **Equation 7.2**.

$$N = \varphi \frac{E\lambda}{hc}\left(1 - R_{pump}\right)\left(1 - T_{pump}\right) \tag{7.2}$$

Here, E is the energy contained in an optical excitation pulse of wavelength λ, R_{pump} is the reflectivity of the sample at normal incidence of the excitation beam, T_{pump} the (small) fraction of light transmitted through the sample and φ is the ratio of free charge carriers created per photons absorbed, commonly referred to as the photon-to-charge branching ratio, which is technically undetermined in the experiment and related to factors such as the exciton binding energy in the material. In this case however, it can be argued that there is some evidence making it appear likely that φ is not substantially lower than unity. This will be discussed later on.

The charge carrier mobility μ is given by:

$$\mu = \frac{\Delta S A_{eff}}{Ne} \tag{7.3}$$

where A_{eff} is the effective area of the overlap of optical pump and THz probe pulse taking into account the Gaussian beam profiles, and e is the elementary charge. With φ unknown, the quantity which can be directly derived from the experiment is the effective mobility $\tilde{\mu} = \varphi\mu$ where

$$\varphi\mu = -\epsilon_0(n_A + n_B)\frac{A_{eff}hc}{Ee\lambda\left(1-R_{pump}\right)\left(1-T_{pump}\right)}\left(\frac{\Delta T}{T}\right) \tag{7.4}$$

Because $0 \leq \varphi \leq 1$, the effective mobility represents a lower limit which becomes identical to the actual mobility for full photon-to-free-carrier conversion. The determined charge carrier mobility arises from the contributions of both electrons and holes, which cannot be separated. Therefore the extracted mobility value is the sum of electron and hole mobilities.

To allow accurate determination of $\varphi\mu$ excitation conditions were kept in the linear regime. Upon evaluation of the dependence of the initial amplitude of the THz response on excitation fluence it was found that nonlinear processes such as two-photon absorption do not have significant effect in the range of fluences used in this study ($\leq 110\ \mu J\ cm^{-2}$). **Figure 7.4** shows the transient photoinduced THz response of $CH_3NH_3SnI_3$ over a range of excitation fluences between 11 $\mu J\ cm^{-2}$ and 108 $\mu J\ cm^{-2}$. It must be noted that the corresponding THz spectra are consistent with a conductivity of free carriers in the presence of localization effects, such as those arising from backscattering at crystallite boundaries.[22]

Previous Hall measurements on $CH_3NH_3SnI_3$ have revealed about eight times higher mobilities, μ, for electrons than for holes; therefore it is expected that the transient THz response due to photoexcited carriers is dominated by free electrons.[14] The effective free carrier mobility has been extracted, such that $\varphi\mu = 1.6\ cm^2\ V^{-1}\ s^{-1}$, where φ is the photon-to-free-charge conversion ratio, the precise value of which, as mentioned previously is unknown. It must be noted, however, that the likelihood of immediate generation of excitons as opposed to free carriers is small due to the high non-resonant excitation about 0.6 eV above the band gap energy, such that φ is likely to be close to unity.

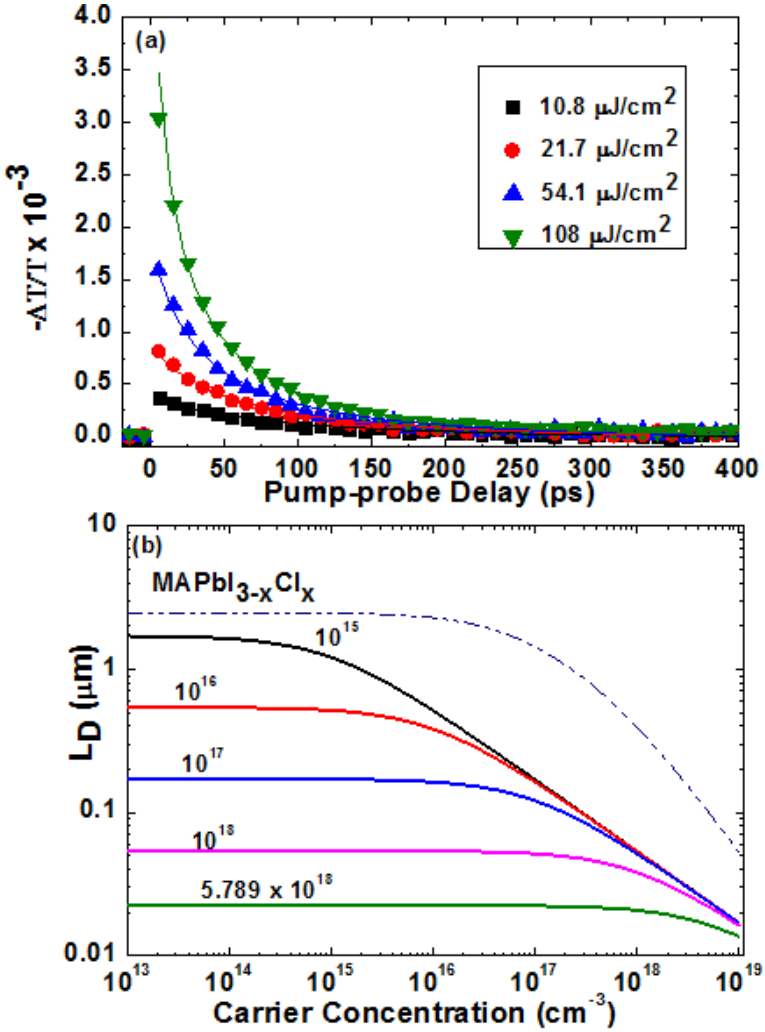

Figure 7.4: (a) Transient terahertz photoconductivity of $CH_3NH_3SnI_3$ on 80 nm thick TiO_2 for a range of excitation fluences. Symbols represent experimental data while solid lines are fits to the data using the model described in the text. (b) Diffusion length (L_D) against the carrier concentration, n, for different hole doping levels as predicted from the model described in the text based on the rate constants extracted from fits to the data shown in (a) and neglecting trap-induced charge recombination. A decrease in the background level of doped holes corresponds to an increase in the diffusion length of the $CH_3NH_3SnI_3$ perovskite. The dash-dotted line displays the diffusion length of the related, as prepared lead-based perovskite $CH_3NH_3PbI_{3-x}Cl_x$ on mesoporous Al_2O_3 (from Ref.[19]) for comparison. This experiment was conducted by Christian Wehrenfennig and the analysis of the data was carried out by Christian Wehrenfennig, Prof. Laura Herz and Dr. Michael B. Johnston of the Department of Physics, University of Oxford.

Earlier conductivity studies on bulk $CH_3NH_3SnI_3$ show strong levels of p-type self-doping due to the presence of Sn^{4+} impurities, on the order of 10^{16} – 10^{18} cm^{-3}.[11,23,24] From the THz measurements taken here, a much faster monomolecular recombination rate is seen than that which was observed with the Pb-based $CH_3NH_3PbI_{3-x}Cl_x$ perovskite. Therefore, assuming that the decay of the photoexcited electron population is predominantly governed by direct recombination with photoexcited and doped holes, the following rate equation can be obtained which can be fitted simultaneously to the fluence-dependent THz conductivity transients (solid lines shown in Figure 7.4).

$$\frac{dn}{dt} = -\gamma n(p + p_0) = -\gamma np - \gamma np_0 \qquad (7.5)$$

Here, γ is the electron-hole recombination rate constant. Note that, since (after thermalization) photoinduced and doped holes are indistinguishable, the corresponding population is described in terms of the sum of the initial hole density before photoexcitation p_0 and the dynamic contribution p(t). In this definition p_0 is equal to the doped hole density in the absence of illumination and p(0) the initial photoexcited hole density (before any recombination events). It must be noted that the first term on the RHS of **Equation 7.5** represents bimolecular recombination between photogenerated carriers, while the second term describes a monomolecular recombination between photogenerated electrons with the fixed concentration, p_0, of dopant holes. From this a value of $\varphi\gamma = 1.4\times10^{-9}$ cm^3 s^{-1} can be extracted for the electron-hole bimolecular recombination rate constant, and a monomolecular decay constant of $\gamma p_0 = 8.08\times10^9$ s^{-1}; and from this a hole-doping density of $\varphi^{-1}p_0 = 5.8\times10^{18}$ cm^3 can be derived. Notably the value for p_o is at the higher end of that reported in previous studies, consistent with a significant extent of self-doping.[24]

The decay dynamics of the photoexcited electron density $n(t)$ can be modelled in terms of recombination with photoexcited and doped holes ($p(t) + p_0$). Here, the influence of monomolecular contributions from trap-mediated processes as well as third- or higher order processes is neglected. The former assumption can to some extent be justified from the comparison to the related lead halide materials, where trap-induced effects have been found to occur on timescales more than two orders of magnitude longer than those studies in our THz experiments.[16,25,26] This results in the rate equation given in Equation 7.5.

As this model only allows decay via e-h-recombination events, n and p have to follow the same time-evolution. Furthermore, as $n(0) = p(0)$, it follows that $n(t) = p(t)$ and therefore Eq. 7.5 becomes:

$$\frac{dn}{dt} = -\gamma n^2 - \gamma p_0 n = -k_2 n^2 - k_1 n \tag{7.6}$$

with $k_2 \overset{\text{def}}{=} \gamma$ and $k_1 \overset{\text{def}}{=} \gamma p_0$. The experimentally observed quantity is the photoinduced THz transmission change $x(t) \overset{\text{def}}{=} (\Delta T/T)(t)$, which is linearly related to the free carrier density (see Eqs. 7.1 and 7.3):

$$n(t) = \varphi C x(t) \tag{7.7}$$

Here $C = \tilde{n}_0/x(0)$ is the proportionality factor between the immediate THz response $x(0)$ and the absorbed photon density

$$\widetilde{n_0} = \frac{E\lambda\alpha(\lambda)}{hcA_{eff}}\left(1 - R_{pump}\right) \tag{7.8}$$

which can be calculated from the pump beam parameters and the absorption coefficient of the sample α at the excitation wavelength λ.

Substituting Eq.7.7 into Eq.7.5, the following solution can be obtained:

$$\frac{dx}{dt} = -C\varphi k_2 x^2 - k_1 x = -A_2 x^2 - A_1 x \quad (7.9)$$

with $A_2 = C\varphi k_2 = C\varphi\gamma$ and $A_1 = k_1 = \gamma p_0$. Solutions to these equations are fit simultaneously to all acquired THz transients of a fluence-dependent set (i.e. there is only one globally optimized value for each of the two rate constants A_1 and A_2, which is applied to all fluences). As the photon-to-free-carrier conversion ratio φ is unknown, strictly speaking, only the values $\varphi\gamma = A_2/C$ and $\varphi^{-1}p_0 = CA_1/A_2$ can be determined from these fits. These equal the actual decay rate constant γ and hole-doping density p_0 in the case where the material exhibits full photon-to-free-charge conversion. To account for the spatially varying charge density profile, the fit routine takes into account the exponential charge density profile created by the pump beam by dividing the sample into 50 equally thick slabs and computing the decay function for all of these individually.

With the knowledge of the charge-carrier mobility and the recombination rates, a charge-diffusion length under realistic device operating conditions can now be derived using the following equations:

$$L(n) = \sqrt{\frac{D}{R(n)}} = \sqrt{\frac{\mu k_B T}{eR(n)}} \quad (7.10)$$

with the *D* being the diffusion coefficient, *T* the temperature, *e* the electronic charge, and the R(n) the total carrier recombination rate, which is given by:

$$R(n) = -\frac{1}{n}\frac{dn}{dt} = \varphi\gamma(n/\phi) + \gamma p_0 \quad (7.11)$$

Solving these equations with the mobility and recombination rates obtained above, a charge diffusion length of 30 nm is obtained for the $CH_3NH_3SnI_3$ system. This value

falls substantially short of the diffusion length of over 1 micron reported for $CH_3NH_3PbI_{3-x}Cl_x$,[19,25] suggesting that the Sn-based material, as prepared here, is unlikely to function well as a solar cell absorber in a planar heterojunction architecture, and should hence require a distributed heterojunction.

With the knowledge of the effective mobility, the bimolecular recombination rate constant and an estimate of the background concentration of doped holes, the change in diffusion length with the background concentration of doped holes can be estimated. Figure 7.4 shows a graph of simulated diffusion length against photoexcited carrier concentration for five different doped hole concentrations. For comparison a plot of the actual diffusion length of the as prepared Pb analogue ($CH_3NH_3PbI_{3-x}Cl_x$) is added. This plot shows that if the background doping level in the $CH_3NH_3SnI_3$ perovskite were to be decreased to the order of $10^{15}cm^{-3}$, then the diffusion length could increase beyond a micron in length and approach that of the very efficient Pb-based perovskite system. This result is a direct consequence of the low bi-molecular recombination rate observed for the material, which is similarly low compared to the value previously determined for the Pb-based counterpart.

Despite the slightly lower THz carrier mobility, this rate is still short of the prediction of the Langevin model by a factor $5\times10^4 \times \epsilon^{-1}$, with ϵ being the relative permittivity of the material. The observations discussed here clearly identify the reduction of self-doping as a promising strategy to enhance the carrier lifetime and hence, improve prospects for efficient photovoltaic device operation.

7.6 Scanning Electron Microscopy

Unlike the Pb-based perovskite which requires heating to crystallise, the Sn perovskites crystallise at room temperature. This is actually an impediment to uniform film formation, as has previously been observed for $MAPbBr_3$ which also crystallises directly upon spin-coating.[27,28] Directly upon spin coating, the $CH_3NH_3SnI_3$ film crystallises, and in the case of a thin mesoporous TiO_2 layer, large crystalline platelets can form on top of the surface in addition to the material which penetrates the pores. These crystalline platelets are apparent in the scanning electron microscopy (SEM) images shown in **Figure 7.5a.** This image displays a collection of large, 3-5 μm, randomly oriented crystals in the case of the $CH_3NH_3SnI_3$ perovskite films, whereas both planar heterojunction and meso-superstructured $CH_3NH_3PbI_{3-x}Cl_x$ perovskite films have been shown to be much smoother with a greater degree of surface coverage (see Fig.7.5b).[29,30] Previously, The $MAPbI_{3-x}Cl_x$ films also exhibited non-uniform coverage, and sporadic formation of islands on top of the mesoporous oxide films.[31] However, with controlled crystallisation it has been possible to considerably improve the film formation.[18,31,32] Conversely, in the case of a thicker mesoporous layer (400 nm) as is shown in Fig.7.5c, there is no visible capping layer of perovskite suggesting that all the crystallites are contained within the mesopores of the TiO_2. A cross section of a complete device (which will be discussed later) is shown in **Figure 7.5d**. This device is fabricated with 400nm thick mesoporous TiO_2 and in the cross section shown there does not appear to be a capping crystal. The dark region within the hole transporting material (HTM) phase is likely to be a shadowing effect rather than a perovskite capping layer.

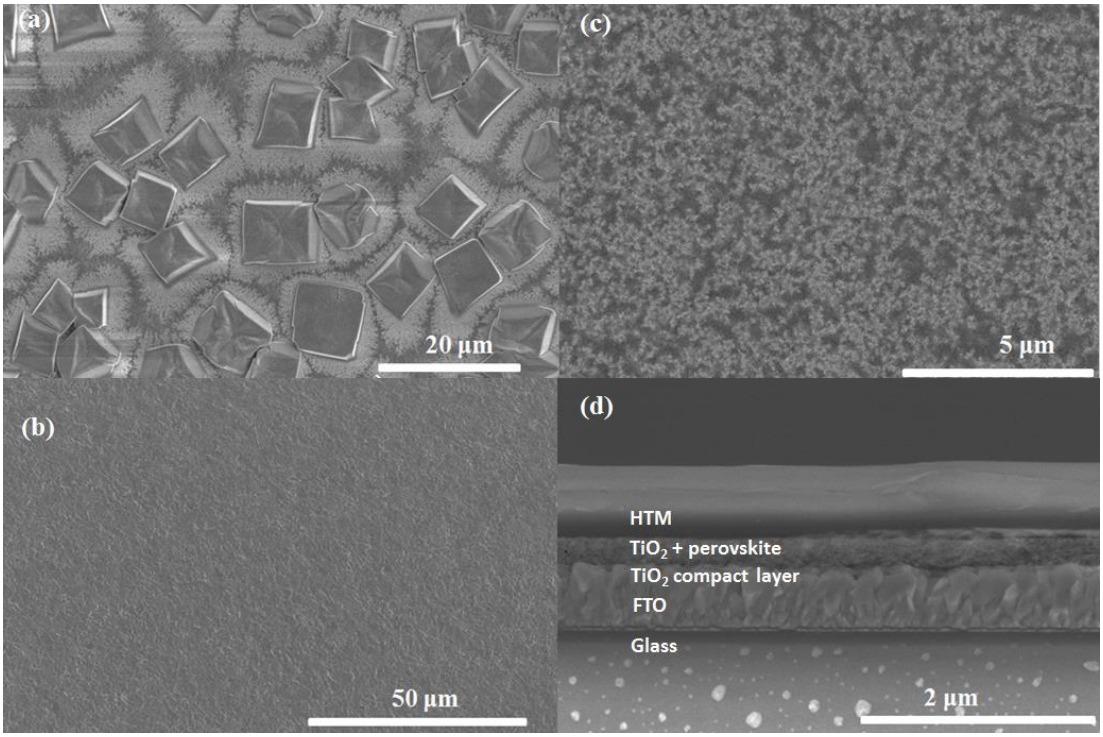

Figure 7.5: (a) Top view of a film of $CH_3NH_3SnI_3$ spin-coated onto mesoporous TiO_2 (80nm thickness). (b) Top view of a film of $CH_3NH_3SnI_3$ spin-coated onto mesoporous TiO_2 (400 nm thickness). (c) Top view of a spin-coated film of $CH_3NH_3PbI_{3-x}Cl_x$ on mesoporous TiO_2 (400 nm thickness). (d) Cross-sectional view of a complete device active layer composed of FTO glass/compact TiO_2 (50nm) /mesoporous TiO_2 infiltrated with $CH_3NH_3SnI_3$ (400nm)/Spiro-OMeTAD (600nm).

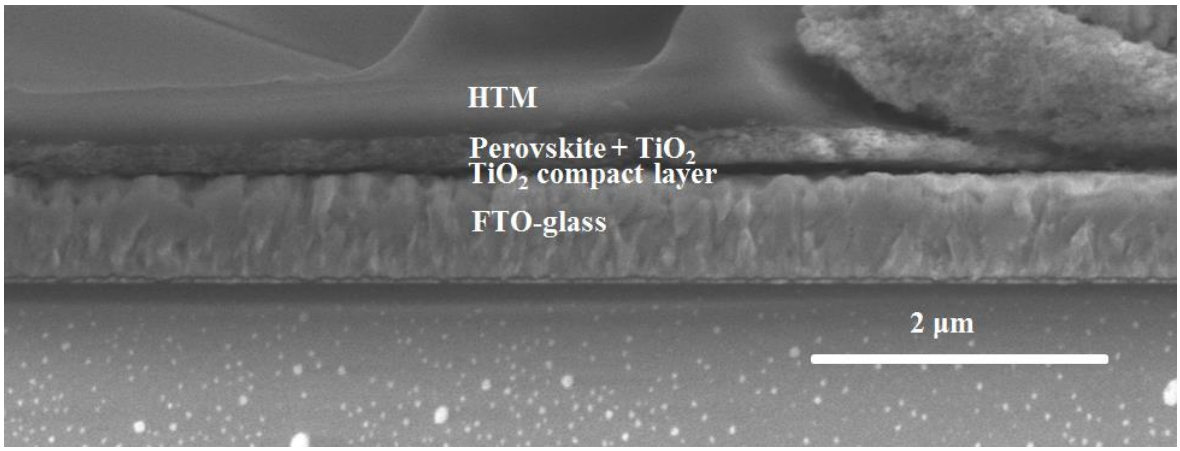

Figure 7.6: Cross-sectional SEM image of a TiO_2-based $CH_3NH_3SnI_3$ device.

The cross-sectional SEM image shown in **Figure 7.6** illustrates more clearly that there is no capping layer of perovskite formed by $CH_3NH_3SnI_3$ in this device configuration. In a device with a 400 nm thick mesoporous TiO_2, the perovskite material is contained solely within the pores of the TiO_2. The delamination of the TiO_2 layer occurs as a result of fracturing the device. The formation of a capping layer in such a device is undesirable as a result of the short diffusion length of the material, which will cause recombination to occur on a faster timescale than charge extraction. Top view images of both 80 nm thick and 400 nm thick TiO_2 films infiltrated with $CH_3NH_3SnI_3$ are shown in **Figure 7.7**. These images very accurately illustrate the loss of the capping layer with increased film thickness.

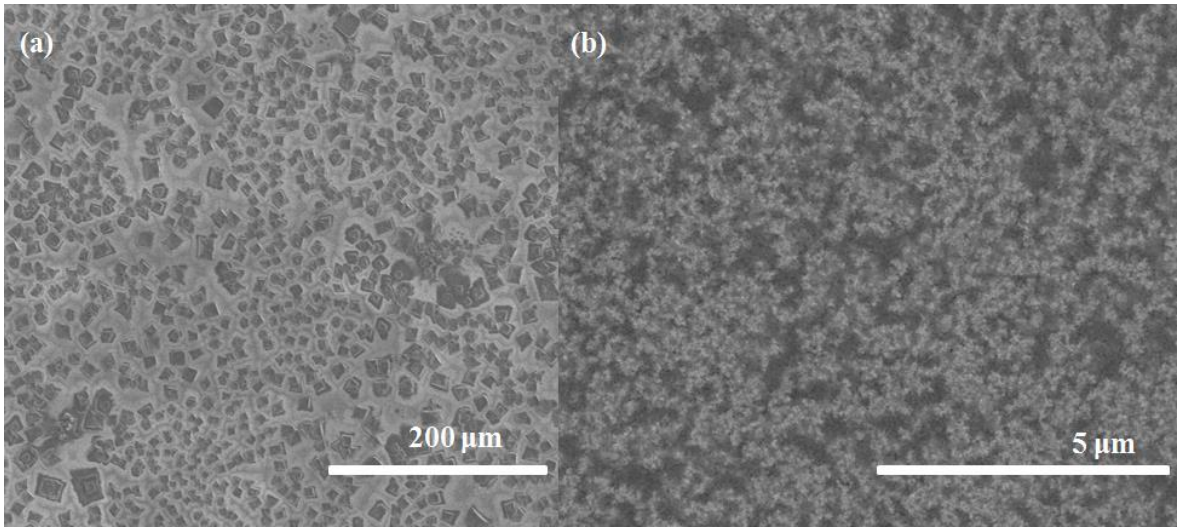

Figure 7.7: Top view SEM image of (a) A capping layer of disperse $CH_3NH_3SnI_3$ crystal formed on an 80 nm thick film of TiO_2. (b) $CH_3NH_3SnI_3$ coated on a 400 nm thick film of TiO_2 such that all of the crystallites have formed within the pores of the TiO_2 and no capping layer is present.

7.7 Device Performance

With the knowledge of the short diffusion length, perovskite-sensitised solar cells (PSSCs) were fabricated. The assembly of these devices is given in detail in Chapter 3, and were composed of FTO coated glass/ compact TiO_2/ mesoporous TiO_2 (400nm) coated with the $CH_3NH_3SnI_3$/Spiro-OMeTAD/Au. The entire device was assembled in a nitrogen-filled glovebox after which the devices were transferred to the evaporator located within the glovebox, hence avoiding exposure to air. Encapsulation was subsequently performed under the same conditions using a hot melt polymer laminate with a glass coverslip, and epoxy resin to seal around the edges. This was done so that the device was exposed to negligible levels of oxygen or moisture during fabrication. The sealed cells were then removed from the glove box and immediately measured in air. Control devices using the Pb-based perovskite as an absorber were also fabricated in the glovebox and tested in the same manner, but without encapsulation. Device performance parameters from a batch of cells, along with the current-voltage characteristics of the best devices, are presented in **Figure 7.8**. The performance parameters of the best devices are presented in **Table 7.1**.

There is a broad spread in the performance of the $CH_3NH_3SnI_3$ solar cells. Here, I show that the best performing Sn-based device reaches a power efficiency of 6.4% under 1-sun illumination. Quite remarkably, for an absorber with a bandgap of 1.23 eV, the open circuit voltages reach values as high 0.88 V in the most efficient device. The fundamental energy loss in a photovoltaic system can be taken as the difference between the bandgap and the open-circuit voltage obtained.[33] For crystalline silicon solar cells, which currently dominate the market, this loss is approximately 0.35 eV, while for GaAs, our closest example of a perfectly ordered crystalline material, the loss is in the range of 0.27 eV.[3,34,35] Here, the loss we estimate is only 0.35 eV in the best performing cells, which matches that of c-Si.[36]

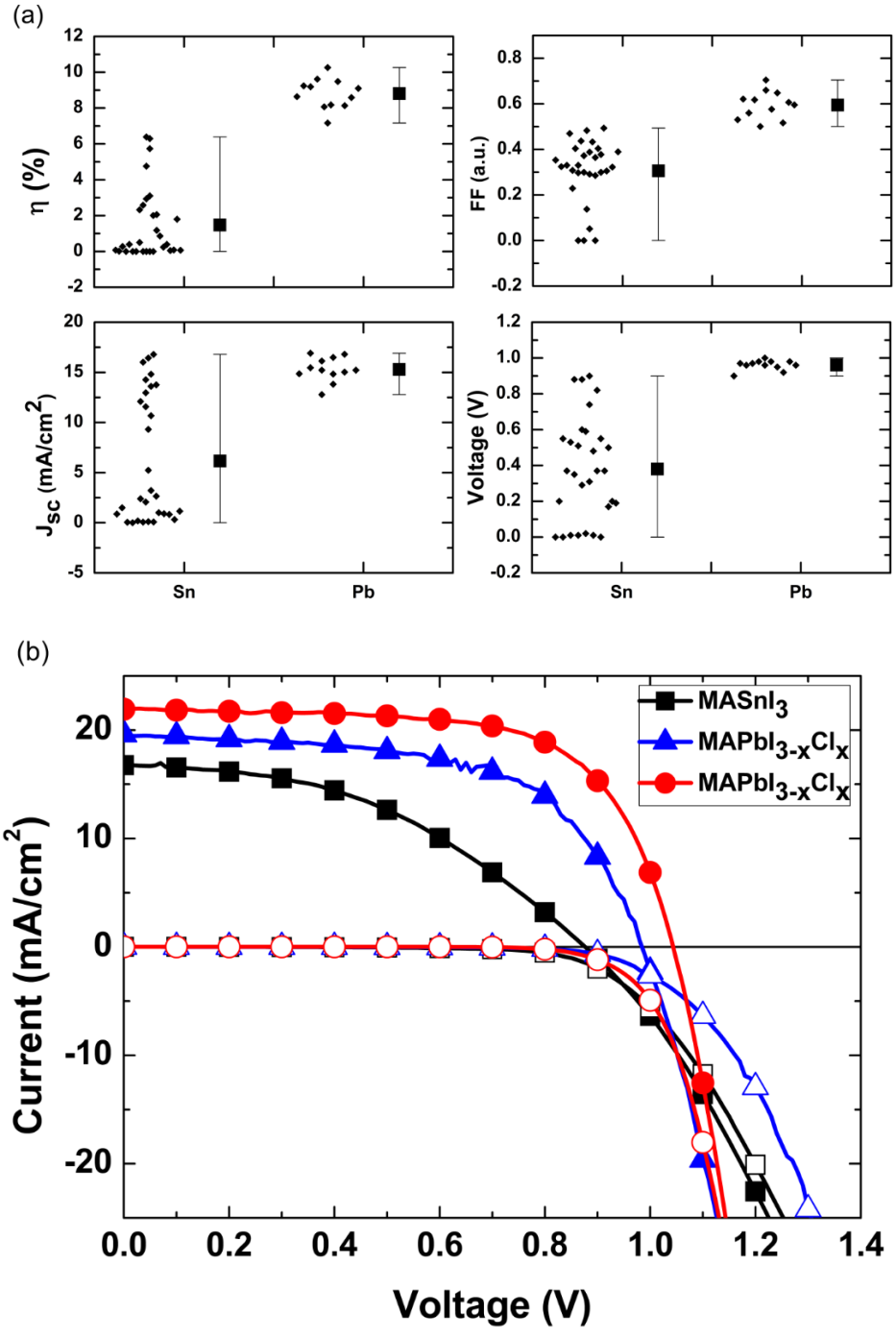

Figure 7.8: (a) The solar cell performance parameters extracted from measuring current-voltage curves under AM1.5 simulated sun light of 100 mWcm^{-2} for TiO_2-based perovskite sensitized solar cells employing $CH_3NH_3SnI_3$ (Sn) and $CH_3NH_3PbI_{3-x}Cl_x$ (Pb)

absorbers. (b) Current-voltages curves of the best Sn-based and Pb-based devices for the batch of devices shown in (a). Light JV curves are denoted with solid symbols and the dark IV curves with hollow symbols. The Pb-based perovskite is shown both on TiO_2 (blue curve) and Al_2O_3 (red curve). It is important to note that the Sn-based devices were fabricated, metal electrodes evaporated and devices sealed in a nitrogen filled glove box prior to exposing to air.

	J_{sc} (mA/cm^2)	η (%)	V_{oc} (V)	F.F. (a.u.)
$MASnI_3$	16.8	6.4	0.88	0.42
$MAPbI_{3-x}Cl_x$ (Al_2O_3)	21.9	15.0	1.04	0.66
$MAPbI_{3-x}Cl_x$ (TiO_2)	19.6	11.5	0.98	0.60

Table 7.1: Performance parameters of the best performing Sn-based device, as well as the best performing Pb-based perovskite sensitized (TiO_2) and mesosuperstructured (Al_2O_3) devices.

Observing such high open-circuit voltages in these solar cells is unexpected considering the relatively short lifetime and hence diffusion length, as well as the use of mesoporous TiO_2, which has previously resulted in lower open-circuit voltages in $CH_3NH_3PbI_{3-x}Cl_x$ solar cells.[5,37] However, if the low diffusion length is a consequence of the fast recombination to doped carriers as inferred, then this will not necessarily impede the open-circuit voltage. The inferred high p-doping density (10^{18}cm^{-3}) is much higher than the photo-induced charge density under full sun light (<10^{15} cm^{-3} for the Pb-based perovskite).[25,38] This implies that under open-circuit conditions where no holes can be swept out of the device, the quasi Fermi level for holes will be very close to the valence band edge. Provided that electrons can transfer quickly and efficiently to the TiO_2, in principle the quasi Fermi level for electrons may be set by the Fermi level in the TiO_2. The additional surprise is that the mesoporous TiO_2 would also

have to become comparably doped to enable the quasi Fermi level for electrons to be close to the conduction band, which is required to sustain such a high open-circuit voltage under illumination.

Figure 7.9 shows a zoom-in of the dark current-voltage curves, and it can be seen that the dark current for the best device only exhibits marginally more leakage at low bias (0 to 0.6V) than the Pb based perovskite solar cells. It must be noted here that while the leakage current of the $CH_3NH_3SnI_3$ based device is larger than the leakage current of its Pb counterpart, they are not greatly dissimilar. It is possible that in the best performing devices such as this, the background density of holes due to self-doping is lower than the hole density in other devices which show poorer performance. The uncontrolled nature of this self-doping mechanism can therefore be used to account for the large spread in the V_{oc} of a given batch, as the doping density will presumably vary from device to device.

However, for the poorer performing cells the dark current leakage is significant, as is shown in **Figure 7.10**, and is largely responsible for the wide spread in open-circuit voltage. It is likely that there is a range of doping densities within the as prepared and tested devices which could account for this variable dark current leakage. Evidently, this does require further investigation. While one would expect higher short-circuit currents from a low band gap system such as this, a major factor which would inhibit both the J_{sc} and the FF is the short electron diffusion length. This is quite possibly due to excessive self-doping, but with appropriate control of this phenomenon, coupled with improved control of the thin film processing, these early solar cell results are very promising. The graphs shown in Fig.7.10 present the JV characteristics for devices with a range of power conversion efficiencies from 0.1% to 4%. In the case of the worst performing devices, I propose that the self-doping problem is so severe that it causes the short-

circuiting of the device. The results presented in Figures 7.9 and 7.10 suggest that a decrease in the doping density, and thus the leakage current of the device, corresponds to an increase in the performance of the devices. This presents strong motivation for the control of this doping mechanism, as it promises to greatly increase the efficiency of these devices.

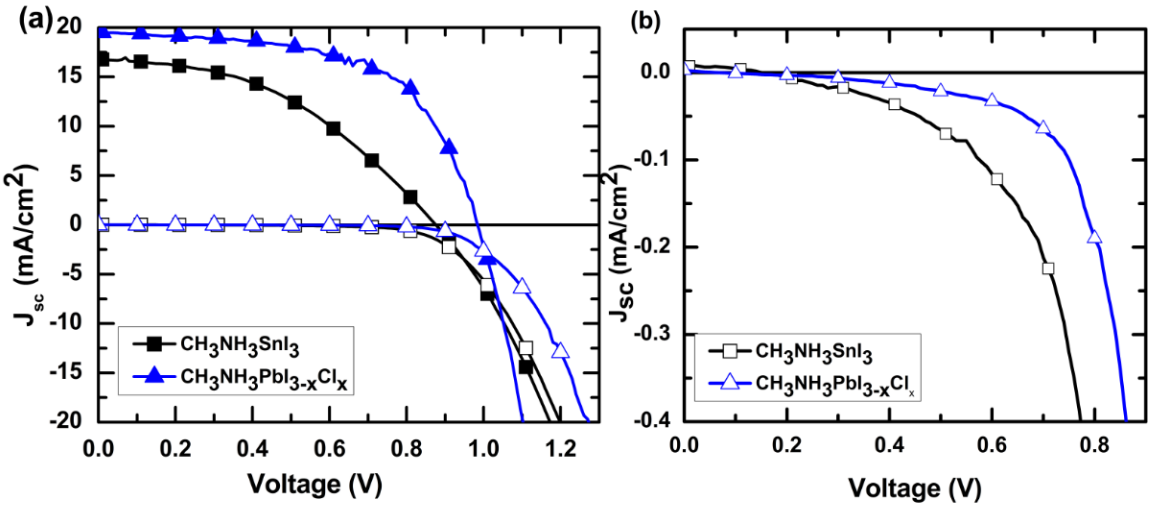

Figure 7.9: (a) The current density-voltage (JV) characteristics of the best performing TiO_2 based $CH_3NH_3SnI_3$ (black) and $CH_3NH_3PbI_{3-x}Cl_x$ (blue) devices. The dark JV curves are represented by the hollow symbols. (b) A zoom in on the current scale for the dark JV curves for both devices, with $CH_3NH_3PbI_{3-x}Cl_x$ shown in blue and $CH_3NH_3SnI_3$ in black.

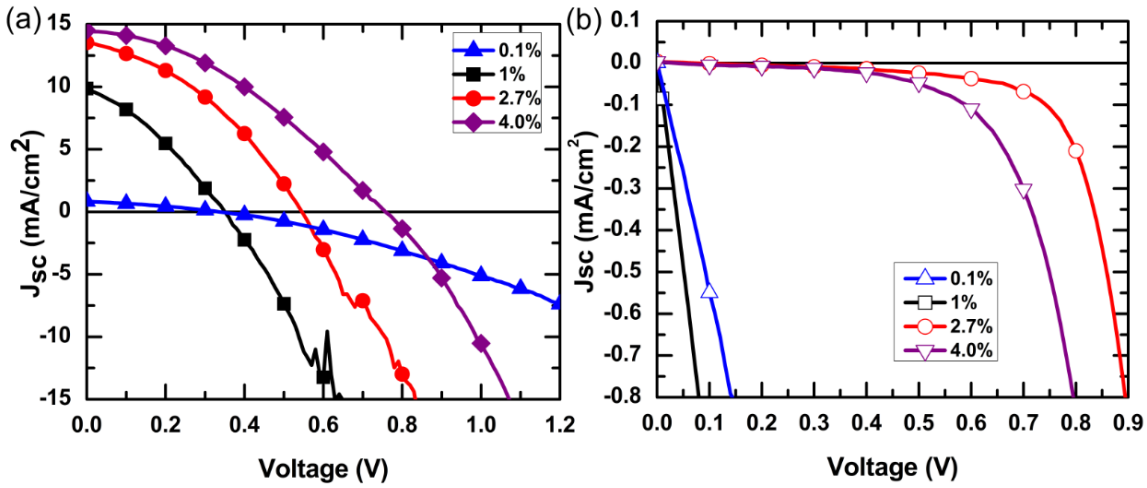

Figure 7.10: (a) Current-voltage (JV) characteristics of $CH_3NH_3SnI_3$ devices of a spread power conversion efficiencies (PCE) under illumination. The PCEs of the devices are as follows: 0.1% (blue triangles), 1% (black squares), 2.7 % (red circles), 4.0% (purple diamonds). (b) Corresponding dark JV characteristics for the devices shown in (a), represented by hollow symbols.

It must be highlighted however, that even with encapsulation the devices still quickly degrade when tested under ambient conditions. Within minutes of measuring, a deeply coloured device can become completely transparent. This is indicative of either the current device sealing protocol failing to prevent oxygen/ moisture from causing device degradation or a fundamental instability of the material. In the devices, metal electrodes are employed to extract the current, with current configuration used in the lab, it is not possible to completely seal beneath the electrodes. Hence, oxygen and moisture could ingress the film through the active layer beneath the electrodes. In order to determine if complete sealing would inhibit the rapid degradation, $CH_3NH_3SnI_3$ films were processed on large glass substrates all the material was scraped away from the edge of the glass slides. They were then completely sealed with the hot-melt polymer film, a glass cover slide and edge sealed with epoxy resin. These films were subject to a continuous light soaking over a 4-month period. After 4 months the films were still visibly coloured and there was no significant drop in their absorbance

indicating that with appropriate current extraction and sealing protocol, predominant stabilisation should be possible. **Figure 7.11** shows a photograph of the film used for light soaking, as well as some solar cells which have degraded after testing.

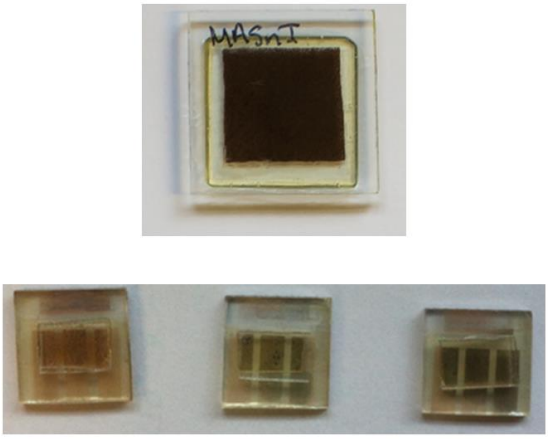

Figure 7.11: A film of $MASnI_3$ which was completely encapsulated and underwent light soaking for a period of 4 months without undergoing any discolouration as compared to TiO_2 based $MASnI_3$ lab-scale devices which have discoloured after 10-20 minutes of exposure to ambient conditions.

7.8 Summary and Outlook

In conclusion, the results presented in this chapter have provided the first demonstration of an efficient, completely lead-free perovskite solar cell using the Sn-based perovskite, $CH_3NH_3SnI_3$ as the absorber layer. This shows that good photovoltaic performance and unexpectedly high open-circuit voltage is not strictly limited to lead-based perovskites. These devices yielded efficiencies of more than 6%, however the stability of $CH_3NH_3SnI_3$ remains a challenge. The voltage losses in the material appear to be remarkably low,

suggesting that when its full potential is exploited, the efficiencies could very well approach those of c-Si and GaAs. The mobility of the as prepared films has been determined to be approximately 1.6 $cm^2\ V^{-1}\ s^{-1}$ and the diffusion length to be approximately 30 nm as compared to over a micron in the Pb-based perovskites, $CH_3NH_3PbX_3$.[19,25,26]

However, the diffusion length is limited by recombination with what we postulate to be self-doped carriers, and if the background concentration of holes were to be decreased, then the diffusion length could approach 1 micron, opening the possibility for planar heterojunction devices. The pivotal issue is now the stabilisation of the material such that the oxidation of the Sn within the crystal is supressed, thus reducing the doping levels of the material and enabling long term stable operation. By achieving a solution to this, we may see the performance of Sn perovskites surpassing those of the state-of-the-art Pb-based perovskites over the next few years, with a distinct toxicology advantage.

7.9 References

[1] (NREL), N. R. E. L. *NREL*, <www.nrel.gov/ncpv/images/efficiency_chart.jpg> (2014).

[2] Yella, A. *et al.* Porphyrin-Sensitized Solar Cells with Cobalt (II/III)–Based Redox Electrolyte Exceed 12 Percent Efficiency. *Science* **334**, 629-634, doi:10.1126/science.1209688 (2011).

[3] Green, M. A., Emery, K., Hishikawa, Y., Warta, W. & Dunlop, E. D. Solar cell efficiency tables (version 43). *Progress in Photovoltaics: Research and Applications* **22**, 1-9, doi:10.1002/pip.2452 (2014).

[4] Chang, J. A. *et al.* Panchromatic Photon-Harvesting by Hole-Conducting Materials in Inorganic–Organic Heterojunction Sensitized-Solar Cell through the Formation of Nanostructured Electron Channels. *Nano Letters* **12**, 1863-1867, doi:10.1021/nl204224v (2012).

[5] Lee, M. M., Teuscher, J., Miyasaka, T., Murakami, T. N. & Snaith, H. J. Efficient Hybrid Solar Cells Based on Meso-Superstructured Organometal Halide Perovskites. *Science* **338**, 643-647, doi:10.1126/science.1228604 (2012).

[6] Burschka, J. *et al.* Sequential deposition as a route to high-performance perovskite-sensitized solar cells. *Nature* **499**, 316-319, doi:10.1038/nature12340 http://www.nature.com/nature/journal/v499/n7458/abs/nature12340.html#supplementary-information (2013).

[7] Liu, M., Johnston, M. B. & Snaith, H. J. Efficient planar heterojunction perovskite solar cells by vapour deposition. *Nature* **501**, 395-398, doi:10.1038/nature12509 (2013).

[8] Malinkiewicz, O. *et al.* Perovskite solar cells employing organic charge-transport layers. *Nat Photon* **8**, 128-132, doi:10.1038/nphoton.2013.341 http://www.nature.com/nphoton/journal/v8/n2/abs/nphoton.2013.341.html#supplementary-information (2014).

[9] Hao, F., Stoumpos, C. C., Cao, D. H., Chang, R. P. H. & Kanatzidis, M. G. Lead-free solid-state organic-inorganic halide perovskite solar cells. *Nat Photon* **8**, 489-494, doi:10.1038/nphoton.2014.82

http://www.nature.com/nphoton/journal/v8/n6/abs/nphoton.2014.82.html#supplementary-information (2014).

[10] Kagan, C. R., Mitzi, D. B. & Dimitrakopoulos, C. D. Organic-Inorganic Hybrid Materials as Semiconducting Channels in Thin-Film Field-Effect Transistors. *Science* **286**, 945-947, doi:10.1126/science.286.5441.945 (1999).

[11] Takahashi, Y. *et al.* Charge-transport in tin-iodide perovskite CH3NH3SnI3: origin of high conductivity. *Dalton Transactions* **40**, 5563-5568, doi:10.1039/C0DT01601B (2011).

[12] Mitzi, D. B., Feild, C. A., Schlesinger, Z. & Laibowitz, R. B. Transport, Optical, and Magnetic Properties of the Conducting Halide Perovskite CH3NH3SnI3. *Journal of Solid State Chemistry* **114**, 159-163, doi:http://dx.doi.org/10.1006/jssc.1995.1023 (1995).

[13] Ogomi, Y. *et al.* CH3NH3SnxPb(1–x)I3 Perovskite Solar Cells Covering up to 1060 nm. *The Journal of Physical Chemistry Letters*, 1004-1011, doi:10.1021/jz5002117 (2014).

[14] Stoumpos, C. C., Malliakas, C. D. & Kanatzidis, M. G. Semiconducting Tin and Lead Iodide Perovskites with Organic Cations: Phase Transitions, High Mobilities, and Near-Infrared Photoluminescent Properties. *Inorganic Chemistry* **52**, 9019-9038, doi:10.1021/ic401215x (2013).

[15] Ball, J. M., Lee, M. M., Hey, A. & Snaith, H. Low-Temperature Processed Mesosuperstructured to Thin-Film Perovskite Solar Cells. *Energy & Environmental Science* (2013).

[16] Wehrenfennig, C., Liu, M., Snaith, H. J., Johnston, M. B. & Herz, L. M. Homogeneous Emission Line Broadening in the Organo Lead Halide Perovskite

CH3NH3PbI3–xClx. *The Journal of Physical Chemistry Letters*, 1300-1306, doi:10.1021/jz500434p (2014).

[17] De Wolf, S. *et al.* Organometallic Halide Perovskites: Sharp Optical Absorption Edge and Its Relation to Photovoltaic Performance. *The Journal of Physical Chemistry Letters* **5**, 1035-1039, doi:10.1021/jz500279b (2014).

[18] Eperon, G. E. *et al.* Formamidinium lead trihalide: a broadly tunable perovskite for efficient planar heterojunction solar cells. *Energy & Environmental Science* **7**, 982-988, doi:10.1039/C3EE43822H (2014).

[19] Wehrenfennig, C., Eperon, G. E., Johnston, M. B., Snaith, H. J. & Herz, L. M. High Charge Carrier Mobilities and Lifetimes in Organolead Trihalide Perovskites. *Advanced Materials* **26**, 1584-1589, doi:10.1002/adma.201305172 (2014).

[20] Nienhuys, H.-K. & Sundström, V. Intrinsic complications in the analysis of optical-pump, terahertz probe experiments. *Physical Review B* **71**, 235110 (2005).

[21] Ulbricht, R., Hendry, E., Shan, J., Heinz, T. F. & Bonn, M. Carrier dynamics in semiconductors studied with time-resolved terahertz spectroscopy. *Reviews of Modern Physics* **83**, 543-586 (2011).

[22] Němec, H., Kužel, P. & Sundström, V. Far-Infrared Response of Free Charge Carriers Localized in Semiconductor Nanoparticles. *Phys. Rev. B* **79**, 115309 (2009).

[23] Mitzi, D. B., Feild, C. A., Schlesinger, Z. & Laibowitz, R. B. Transport, Optical, and Magnetic Properties of the Conducting Halide Perovskite {CH3NH3SnI3}. *J. Solid State Chem.* **114**, 159-163 (1995).

[24] Takahashi, Y., Hasegawa, H., Takahashi, Y. & Inabe, T. Hall mobility in tin iodide perovskite CH3NH3SnI3: Evidence for a doped semiconductor *J. Solid State Chem.* **205**, 39-43 (2013).

[25] Stranks, S. D. *et al.* Electron-Hole Diffusion Lengths Exceeding 1 Micrometer in an Organometal Trihalide Perovskite Absorber. *Science* **342**, 341-344, doi:10.1126/science.1243982 (2013).

[26] Xing, G. *et al.* Long-Range Balanced Electron- and Hole-Transport Lengths in Organic-Inorganic CH3NH3PbI3. *Science* **342**, 344-347, doi:10.1126/science.1243167 (2013).

[27] Edri, E., Kirmayer, S., Cahen, D. & Hodes, G. High Open-Circuit Voltage Solar Cells Based on Organic–Inorganic Lead Bromide Perovskite. *The Journal of Physical Chemistry Letters* **4**, 897-902, doi:10.1021/jz400348q (2013).

[28] Kojima, A., Teshima, K., Shirai, Y. & Miyasaka, T. Organometal Halide Perovskites as Visible-Light Sensitizers for Photovoltaic Cells. *Journal of the American Chemical Society* **131**, 6050-6051, doi:10.1021/ja809598r (2009).

[29] Tan, K. W. *et al.* Thermally Induced Structural Evolution and Performance of Mesoporous Block Copolymer-Directed Alumina Perovskite Solar Cells. *ACS Nano* (2014).

[30] Saliba, M. *et al.* The Influence of Thermal Processing Protocol upon the Crystallization and Photovoltaic Performance of Organic-Inorganic Lead Trihalide Perovskites. *The Journal of Physical Chemistry C* (2014).

[31] Eperon, G. E., Burlakov, V. M., Docampo, P., Goriely, A. & Snaith, H. J. Morphological Control for High Performance, Solution-Processed Planar

Heterojunction Perovskite Solar Cells. *Advanced Functional Materials* **24**, 151-157, doi:10.1002/adfm.201302090 (2014).

[32] Conings, B. *et al.* Perovskite-Based Hybrid Solar Cells Exceeding 10% Efficiency with High Reproducibility Using a Thin Film Sandwich Approach. *Advanced Materials* **26**, 2041-2046, doi:10.1002/adma.201304803 (2014).

[33] Snaith, H. J. Estimating the Maximum Attainable Efficiency in Dye-Sensitized Solar Cells. *Advanced Functional Materials* **20**, 13-19, doi:10.1002/adfm.200901476 (2010).

[34] Nayak, P. K., Bisquert, J. & Cahen, D. Assessing Possibilities and Limits for Solar Cells. *Advanced Materials* **23**, 2870-2876, doi:10.1002/adma.201100877 (2011).

[35] Nayak, P. K. & Cahen, D. Updated Assessment of Possibilities and Limits for Solar Cells. *Advanced Materials* **26**, 1622-1628, doi:10.1002/adma.201304620 (2014).

[36] Shockley, W. & Queisser, H. J. Detailed Balance Limit of Efficiency of p-n Junction Solar Cells. *Journal of Applied Physics* **32**, 510-519, doi:doi:http://dx.doi.org/10.1063/1.1736034 (1961).

[37] Leijtens, T., Lauber, B., Eperon, G. E., Stranks, S. D. & Snaith, H. J. The Importance of Perovskite Pore Filling in Organometal Mixed Halide Sensitized TiO2-Based Solar Cells. *The Journal of Physical Chemistry Letters* **5**, 1096-1102, doi:10.1021/jz500209g (2014).

[38] D'Innocenzo, V. *et al.* Excitons versus free charges in organo-lead tri-halide perovskites. *Nat Commun* **5**, doi:10.1038/ncomms4586 (2014).

Chapter 8

Conclusions and Outlook

8.1 Salient Points of the Thesis

This thesis has been focused on furthering the development of solution processable, solid state hybrid solar cells, with special emphasis on the sensitized solar cell (ss-SSC) configuration. The optimised thickness of the solid state dye sensitized solar cell is between 2 μm – 3 μm,[1,2] an issue which has long been thought to be limiting the power conversion efficiencies which can be achieved using this device configuration. In this respect, two main avenues to circumventing the thickness limitations of the dye sensitized solar cell have been explored; the first with respect to improving the charge transport through the TiO_2 photoanode, and the second, by using more strongly absorbing sensitizers.

Chapter 4 of this thesis dealt with improving the architecture of the mesoporous TiO_2 photoanode in ss-DSSCs. It has been experimentally proven that charge transport in ss-DSSCs is limited by electron transport through mesoporous TiO_2,[3,4] making improving electron transport through TiO_2 an important consideration in the fabrication of these devices. To this end, this chapter presented the development of mesoporous single crystals (MSCs) of TiO_2, an architecture which combines the high surface area of the conventional sintered nanoparticle film, with the superior electronic properties of single crystalline anatase. Investigation of the electronic properties of these MSCs yielded conductivities which were two orders of magnitude higher than those obtained

for nanoparticle films, and greatly improved electron mobilities at similar charge carrier densities.

Having shown that this material has superior electronic properties, it was integrated into a photovoltaic device where it was found that the structural coherence and long range electronic connectivity of the material obviated the need for high temperature sintering. This lead to the development of the first completely low temperature processed (≤ 150 ˚C) ss-DSSC with power conversion efficiencies rivalling their high temperature processed counterparts. Additionally, even with low temperature processing, films of this material show transport rates which are two orders of magnitude faster than high temperature sintered nanoparticle films. This is a very encouraging prospect for the fabrication of devices with a thicker (> 3 μm) TiO_2 electrode. Of course, the issue of the parasitic absorption of spiro-OMeTAD must also be addressed when considering going towards thicker ss-DSSCs. In this case an alternative hole transporting material (HTM) which has a lesser degree of parasitic absorption should be used. One potential molecule is AS44, a spiro-like molecule which exhibits reduced parasitic absorption when doped, along with comparable power conversion efficiencies.[5] This route is currently being explored.

One of the additional selling points of MSCs of TiO_2 is that the pore size of the material can be tuned by appropriate selection of the silica beads used in the synthesis. This provides a large advantage for semiconductor sensitized solar cells (SSSCs) such as Sb_2S_3 sensitized devices. The control of pore size in this architecture is quite important as it must be sufficiently large to allow deposition of the desired amount of absorber, as well as allow complete infiltration by the hole transporting material, which in this case is P3HT. Chapter 5 presents the application of MSCs to Sb_2S_3 sensitized solar cells, as well as the integration of Sb_2S_3 into a mesosuperstructured solar cell (MSSC) architecture. The Sb_2S_3 devices based on the MSC photoanode generally exhibited higher voltages and short circuit currents which can be attributed to a

reduction in the degree of recombination in the device. This is expected with an increase in the pore size of the material as if the P3HT is allowed to completely infiltrate the device the absorber is more efficiently regenerated.

A reduction in the degree of recombination exhibited by these devices could also be as a result of the increased electron transport rate which has been observed in these MSC-based solar cells. Interestingly, Sb_2S_3 devices also work in the MSSC configuration, where they are deposited on a mesoporous alumina scaffold. This is not without precedence as the hybrid organic-inorganic lead trihalide perovskites have been shown to work efficiently in this configuration.[6-8] This suggests that Sb_2S_3 MSSCs operate in a similar fashion, where electrons are transported through the absorber material to the electrode as opposed to the sensitized configuration where there is electron injection into the conduction band of the TiO_2. This mechanism also provides an explanation for the higher voltages obtained in this configuration, which is approximately equal to the voltage loss expected when electrons are injected into the conduction band of TiO_2 (~200 mV).[6]

Following the philosophy of using more highly absorbing sensitizers to increase the power conversion efficiencies of hybrid solar cells, Chapters 6 and 7 focus on a family of hybrid organic-inorganic perovskites which promise to revolutionise the solar industry. Chapter 6 deals specifically with the recently established lead-based, mixed halide perovskite material, $CH_3NH_3PbI_{3-x}Cl_x$. Hybrid solar cells based on this material have, in only two years of development, achieved impressive certified conversion efficiencies of over 17 %.[9] Recent theoretical and experimental studies have pointed to the presence of trap states in this material, and one specific type of trap site has been attributed to the presence of under-coordinated Pb atoms within the perovskite crystal.[10,11] This chapter presents the passivation of the perovskite absorber by using Lewis base surface treatments; proposing a mechanism for this method of passivation, which involves the formation of a coordinate bond between the lone pair of the Lewis

bases (specifically thiophene or pyridine) and the under-coordinated Pb atom. Through this method of passivation, there is a reduction of the non-radiative recombination which occurs within the film, as investigated using photoluminescence (PL) decay lifetimes and quantum efficiency measurements. Additionally, by globally fitting the PL decay to a mathematical model which describes photoluminescence of these perovskite materials,[12] the trap density of treated and untreated films was extracted, showing a decrease in the trap density for the treated films, of an order of magnitude for pyridine treated films, and a 3x decrease for thiophene treated films. This also corresponds to improved device performance, and perhaps even more strikingly, a massive improvement in the stabilised power output for planar heterojunction solar cells, which has recently been shown to typically be half of the efficiency of the scanned efficiency.[13] This represents a general method of passivation which can be used in perovskite based optoelectronic devices. The increase in PLQE observed, especially at low fluences, can also prove to be quite beneficial to laser and LED applications.

While the lead-based perovskites discussed in Chapter 6 have great promise, the presence of lead in the material may prove to be a barrier to commercialization. To this end, Chapter 7 presents the development of the first operational lead-free organic-inorganic trihalide perovskite sensitized solar cell. In this chapter the tin-based perosvkite, $CH_3NH_3SnI_3$ is used as the absorber material in a TiO_2 based perovskite-sensitized device configuration. A study of the optical properties of this material has shown it to have a band gap of 1.23 eV, and a strong emission peak at 950 nm. By using terahertz spectroscopy the diffusion length of the material was shown to be 30 nm which is much shorter than the 1 μm diffusion length which has been determined in the case of its lead-based counterpart.[14] This has been attributed to a "self-doping" mechanism[15,16] in which Sn^{2+} is oxidised to Sn^{4+} under ambient conditions, increasing the background hole density in the material. Through modelling it has been shown that if this "self-doping" were to be controlled such that the background hole density is decreased, the diffusion length of the material would then increase such that it would be comparable to that of the lead-based perovskite. In such a case, one could expect the

$CH_3NH_3SnI_3$ perovskite to operate efficiently not only in a distributed heterojunction structure, but also in the planar heterojunction architecture. The power conversion efficiency of solar cells utilising this Sn-based perovskite material currently stands at 6.4 %. A similar study by Kanatzidis *et al* has shown devices with efficiencies of 5.73 %. The major challenge facing the implementation and widespread use of this material is the inherent instability of Sn^{2+} under ambient conditions. One method of combating this instability is by using various surface treatments which slow the oxidation of Sn^{2+} to Sn^{4+}. A more promising avenue however is to synthesize a perovskite material with Sn in its 4+ oxidation state. This pathway is currently being explored and a number of these materials have been synthesised. The synthetic route as well as the initial characterisation of these materials is presented in Appendix I.

In conclusion, this thesis has explored various methods of increasing the efficiency of ss-SSCs; firstly with regard to the improvement of the TiO_2 electrode architecture and secondly with respect to using more highly absorbing sensitizers. With the development of lead-based perovskite based solar cells, it seems that the need for a mesostructured photoanode has been severely decreased, however, with the recent development of tin-based perovskites, the MSCs presented in this work may find a new niche. The importance of surface passivation of semiconductor materials has also been shown, as this presents a route to improving the power conversion efficiencies of these devices; but more importantly, vastly improves the stabilized power output of these devices which gives a more realistic picture of what can be expected from these devices under operating conditions. Lastly, a route to efficient, much less toxic, tin-based perovskite solar cells has been elucidated. While this material is still in the infant stages of development and faces major challenges in terms of material stability, it may yet prove to be the non-toxic, abundant solution to widespread exploitation of photovoltaic technologies.

8.2 References

[1] Docampo, P. *et al.* Lessons Learned: From Dye-Sensitized Solar Cells to All-Solid-State Hybrid Devices. *Advanced Materials*, n/a-n/a, doi:10.1002/adma.201400486 (2014).

[2] Snaith, H. J. & Schmidt-Mende, L. Advances in Liquid-Electrolyte and Solid-State Dye-Sensitized Solar Cells. *Advanced Materials* **19**, 3187-3200, doi:10.1002/adma.200602903 (2007).

[3] Leijtens, T., Lim, J., Teuscher, J., Park, T. & Snaith, H. J. Charge Density Dependent Mobility of Organic Hole-Transporters and Mesoporous TiO2 Determined by Transient Mobility Spectroscopy: Implications to Dye-Sensitized and Organic Solar Cells. *Advanced Materials* **25**, 3227-3233, doi:10.1002/adma.201300947 (2013).

[4] Snaith, H. J. & Grätzel, M. Electron and Hole Transport through Mesoporous TiO2 Infiltrated with Spiro-MeOTAD. *Advanced Materials* **19**, 3643-3647, doi:10.1002/adma.200602085 (2007).

[5] Leijtens, T. *et al.* Hole Transport Materials with Low Glass Transition Temperatures and High Solubility for Application in Solid-State Dye-Sensitized Solar Cells. *ACS Nano* **6**, 1455-1462, doi:10.1021/nn204296b (2012).

[6] Lee, M. M., Teuscher, J., Miyasaka, T., Murakami, T. N. & Snaith, H. J. Efficient Hybrid Solar Cells Based on Meso-Superstructured Organometal Halide Perovskites. *Science* **338**, 643-647, doi:10.1126/science.1228604 (2012).

[7] Ball, J. M., Lee, M. M., Hey, A. & Snaith, H. Low-Temperature Processed Mesosuperstructured to Thin-Film Perovskite Solar Cells. *Energy & Environmental Science* (2013).

[8] Bi, D. *et al.* Using two-step deposition technique to prepare perovskite (CH3NH3PbI3) for thin film solar cells based on ZrO2 and TiO2 mesostructures. *RSC Advances*, doi:10.1039/C3RA43228A (2013).

[9] (NREL), N. R. E. L. *NREL*, <www.nrel.gov/ncpv/images/efficiency_chart.jpg> (2014).

[10] Yin, W.-J., Shi, T. & Yan, Y. Unusual defect physics in CH3NH3PbI3 perovskite solar cell absorber. *Applied Physics Letters* **104**, -, doi:doi:http://dx.doi.org/10.1063/1.4864778 (2014).

[11] Shkrob, I. A. & Marin, T. W. Charge Trapping in Photovoltaically Active Perovskites and Related Halogenoplumbate Compounds. *The Journal of Physical Chemistry Letters* **5**, 1066-1071, doi:10.1021/jz5004022 (2014).

[12] Stranks, S. D., Burlakov, V. M., Leijtens, T., Ball, J. M., Goriely, A., Snaith, H. J (2014). *Photoluminescence from Organometal Halide Perovskites: Excitons, Free Charge and Mid-Gap Electronic States*. Sumbitted to Physical Review Letters (2014).

[13] Snaith, H. J. *et al.* Anomalous Hysteresis in Perovskite Solar Cells. *The Journal of Physical Chemistry Letters* **5**, 1511-1515, doi:10.1021/jz500113x (2014).

[14] Stranks, S. D. *et al.* Electron-Hole Diffusion Lengths Exceeding 1 Micrometer in an Organometal Trihalide Perovskite Absorber. *Science* **342**, 341-344, doi:10.1126/science.1243982 (2013).

[15] Mitzi, D. B., Feild, C. A., Schlesinger, Z. & Laibowitz, R. B. Transport, Optical, and Magnetic Properties of the Conducting Halide Perovskite CH3NH3SnI3. *Journal of Solid State Chemistry* **114**, 159-163, doi:http://dx.doi.org/10.1006/jssc.1995.1023 (1995).

[16] Takahashi, Y., Hasegawa, H., Takahashi, Y. & Inabe, T. Hall mobility in tin iodide perovskite CH3NH3SnI3: Evidence for a doped semiconductor *J. Solid State Chem.* **205**, 39-43 (2013).

Appendix I

Ongoing Work on New Hybrid Compounds: Hexahalogenated Stannates

1. Solution-based Synthesis of Cs_2SnI_6

SnI_4 was dissolved in a 3:1 volume ratio of EtOH: HI such that a 1M solution was obtained. The dissolution was carried out in a 3-neck flask under argon flow. The solution was heated to 80˚C with stirring and a 2M aqueous solution of CsI was injected into the flask. Black precipitates formed instantaneously upon injection of the CsI. The solution was left to stand for a further 24 hours under mild reflux to facilitate growth of the crystals in the mother liquor. The crystals were harvested by filtration and were heated to 250˚C in order to purify the compound by driving off excess iodine. Cs_2SnBr_6 (yellow powder) was also fabricated via this method utilising $SnBr_4$ as the source of Sn^{4+}.

2. Solution-based Synthesis of $(CH_3NH_3)_2SnI_6$

SnI_4 was dissolved in a 3:1 volume ratio of EtOH: HI such that a 1M solution was obtained. The dissolution was carried out in a 3-neck flask under argon flow. The

solution was heated to 80˚C with stirring and a 2M aqueous solution of CH_3NH_3I was injected into the flask. The solution was left to stand for a further 24 hours under mild reflux to facilitate growth of the black crystals in the mother liquor. The crystals were harvested by filtration and were heated to 100˚C in order to purify the compound by driving off excess iodine. $(CH_3NH_3)_2SnBr_6$ was also fabricated via this method utilising $SnBr_4$ as the source of Sn^{4+}.

3. X-ray Diffraction Patterns

Cs_2SnI_6 & Cs_2SnBr_6

Both compounds crystallize in cubic structure with space group F d $\bar{3}$ m (no. 227, origin choice 2). For all PXRD experiments Cu$K_{\alpha 1}$ X-ray beam was used.

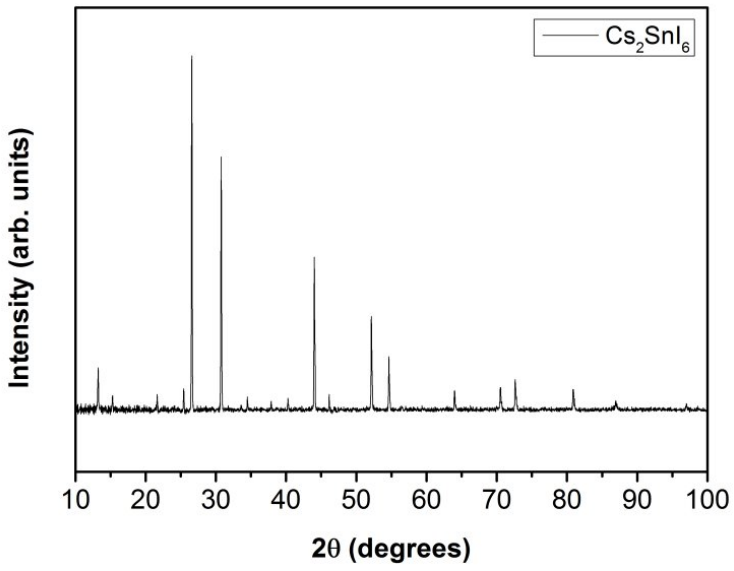

Figure 1: PXRD pattern of Cs_2SnI_6 taken at room temperature (RT).

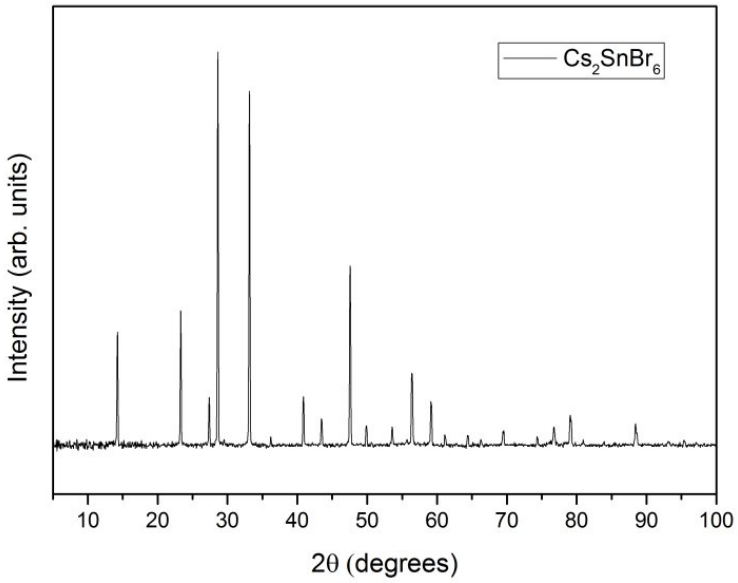

Figure 2: PXRD pattern of Cs_2SnBr_6 taken at RT.

Crystallographic parameters for Cs_2SnI_6 and Cs_2SnBr_6 are listed in Table 1 & 2.

Table 1: Crystallographic data for Cs_2SnI_6

Chemical formula	Cs_2SnI_6
Crystal System	Cubic
Space group	F d -3 m
Cell Parameter a (Å)	11.6313(2)
Z	4
D_c (gcm^{-3})	4.837
R_{exp}	0.02765
R_{wp}	0.03706
R_p	0.02967
X^2	1.80

Table 2: Crystallographic data for Cs_2SnBr_6

Chemical formula	Cs_2SnBr_6
Crystal System	Cubic
Space group	F d -3 m
Cell Parameter a (Å)	10.8414(2)
Z	4
D_c (gcm^{-3})	4.503
R_{exp}	0.01752
R_{wp}	0.02690
R_p	0.02062
X^2	2.36

MA_2SnI_6 & MA_2SnBr_6

These compounds crystallize in a tetragonal crystal structure.

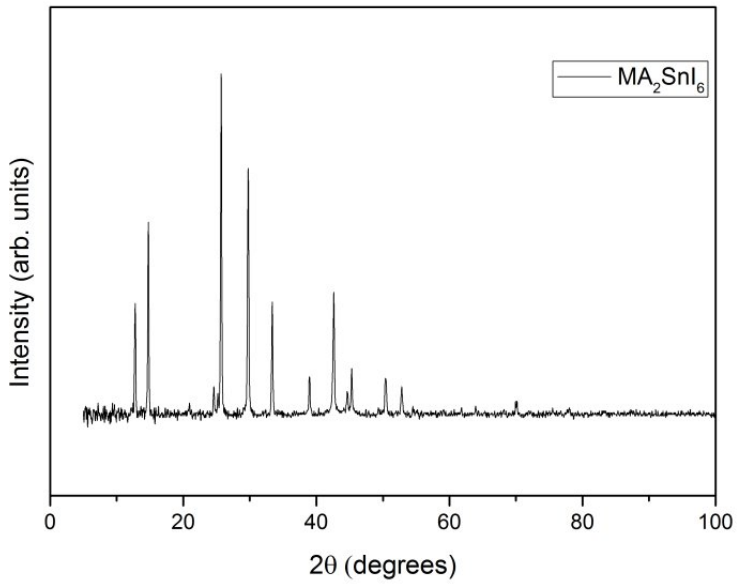

Figure 3: PXRD pattern of MA_2SnI_6 taken at RT.

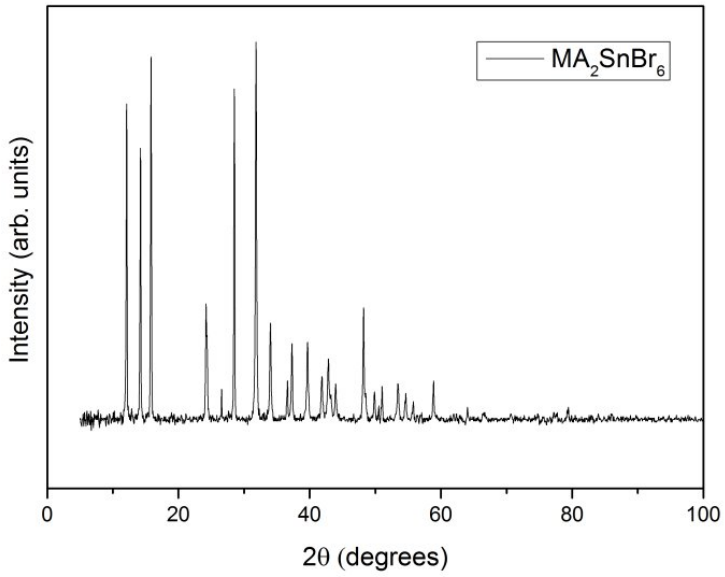

Figure 4: PXRD pattern of MA_2SnBr_6 taken at RT.

Table 2: Crystallographic data for MA_2SnI_6, MA_2SnBr_6 & FA_2SnI_6

Chemical formula	MA_2SnI_6	MA_2SnBr_6
Crystal System	tetragonal	tetragonal
Cell Parameter a (Å)	5.995	6.254
Cell Parameter c (Å)	6.924	7.278

Appendix II

Publications and Conferences

1. Publications

1) Crossland, E. J. W.; Noel, N.; Sivaram, V.; Leijtens, T.; Alexander-Webber, J.; Snaith, H. J. Mesoporous TiO_2 single crystals delivering enhanced mobility and optoelectronic device performance. Nature 2013, 495, (7440), 215-219.

2) Sivaram, V.; Crossland, E. J. W.; Leijtens, T.; Noel, N.K.; Alexander-Webber, J.; Docampo, P.; Snaith, H. J. Observation of Annealing-Induced Doping in TiO_2 Mesoporous Single Crystals for Use in Solid State Dye Sensitized Solar Cells. The Journal of Physical Chemistry C 2014, 118 (4), 1821-1827.

3) Snaith, H. J.; Abate, A.; Ball, J. M.; Eperon, G. E.; Leijtens, T.; Noel, N.K.; Stranks, S. D.; Wang, J. T.W.; Wojciechowski, K.; Zhang, W. Anomalous Hysteresis in Perovskite Solar Cells. The Journal of Physical Chemistry Letters 2014 5 (9), 1511-1515.

4) Docampo, P.; Guldin, S.; Leijtens, T.; Noel, N. K.; Steiner, U.; Snaith, H. J. Lessons Learned: From Dye-Sensitized Solar Cells to All-Solid-State Hybrid Devices. Advanced Materials 2014, 26 (24), 4013-4030.

5) Noel, N. K.; Stranks, S. D.; Abate, A.; Wehrenfennig, C.; Guarnera, S.; Haghighirad, A.; Sadhanala, A.; Eperon, G. E.; Pathak, S. K.; Johnston, M. B.; Petrozza, A.; Herz, L.; Snaith, H. J. Lead-Free Organic-Inorganic Tin Halide Perovskites for Photovoltaic Applications. Energy Environ. Sci., 2014, Accepted Manuscript, doi: 10.1039/C4EE01076K.

6) Noel, N. K.; Abate, A.; Stranks, S. D.; Parrott, E.; Burlakov, V; Goriely, A.; Snaith, H.J. Enhanced Photoluminescence and Device Performance via Lewis Base Passivation in Organic-Inorganic Lead Halide Perovskite Solar Cells. ACS Nano, 2014, Accepted Manuscript, DOI: 10.1021/nn5036476.

7) Noel, N. K.; Crossland, E.J.W.; Leijtens, T.; Nunzi, F.; Sivaram, V.; De Angelis, F.; Snaith, H.J. Mesoporous Single Crystals: A Facile Route to Reduced Electronic Disorder and Efficient, Low Temperature Processed Dye-Sensitized Solar Cells. (Submitted to Advanced Energy Materials) 2014.

8) Cheng, C.; Lee, M. M.; Noel, N. K.; Hughes, G. M.; Ball, J. M.; Assender, H. E.; Snaith, H. J.; Watt, A. A. R. Polystyrene Templated Porous Titania Wells for Quantum Dot Heterojunction Solar Cells. ACS Appl. Mater. Interfaces, *Just Accepted Manuscript,* DOI: 10.1021/am503558q

2. Conferences

- SSSC 2013 in Granada, Spain: Poster Presentation- "Mesoporous Single Crystals: A Facile Route to Efficient Low Temperature Devices" Nakita K. Noel, Edward J.W. Crossland , Tomas Leijtens, Varun Sivaram, Henry J. Snaith.

- PVSAT 9 in Wales, United Kingdom: Talk- "Mesoporous Single Crystals: A Facile Route to Efficient Low Temperature Devices" Nakita K. Noel, Edward J.W. Crossland , Tomas Leijtens, Varun Sivaram, Henry J. Snaith

- SSSC 2014 in Oxford, United Kingdom: Talk- "Lead-Free Organic-Inorganic Tin Halide Perovskites for Photovoltaic Applications" Nakita K. Noel, Samuel D. Stranks, Antonio Abate, Christian Wehrenfennig, Aditya Sadhanala, Laura M. Herz, Michael B. Johnston, Henry J. Snaith

Mesoporous Single Crystals: A Facile Route to Efficient Low Temperature Devices

Nakita K. Noel*, Edward J.W. Crossland , Tomas Leijtens, Varun Sivaram, Henry J. Snaith†
†*E-mail: nakita.noel@physics.ox.ac.uk; h.snaith1@physics.ox.ac.uk
Clarendon Laboratory, Department of Physics, University of Oxford, Parks Road, Oxford, OX1 3PU

Abstract

Low temperature processing of sensitized solar cells (SSC) opens the door to flexible, lightweight devices, as well as multilayer, multijunction devices. In addition to this, low temperature processing will also significantly reduce manufacturing costs. However, the current state of the art SSCs need to be thermally sintered to approximately 500˚C, in order to create a semiconductor layer with both a high surface area, and effective electronic contact. By replacing the conventionally used nanoparticles, with single crystals of TiO_2, we demonstrate a completely low temperature processed (≤150˚C), solid state dye-sensitised solar cell (DSSC) with a power conversion efficiency of 3.6% under 1 sun illumination. These mesoporous single crystals also exhibit enhanced transport properties which is indicative of effective electronic contact without high temperature sintering. As proof of the generality of this concept, perovskite sensitised solar cells ($CH_3NH_3PbCl_xI_{3-x}$) have also been fabricated by this method, yielding efficiencies of up to 9.15%.

Introduction

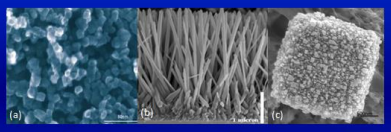

Figure 1: Scanning Electron Microscope (SEM) Images of **(a)** A film of TiO_2 nanoparticles **(b)** A film of TiO_2 nanowires **(c)** A mesoporous single crystal of TiO_2

- When incorporated into photovoltaics, TiO_2 nanowires have been found to exhibit faster electron transport than its nanoparticle counterpart,[1] but also suffer from a decreased surface area over which a sensitizer can be adsorbed.
- Mesoporous Single Crystals (MSCs) combine the high surface area of a nanoparticle film, with the long range connectivity and faster electron transport of nanowires.

Current-Voltage Characteristics

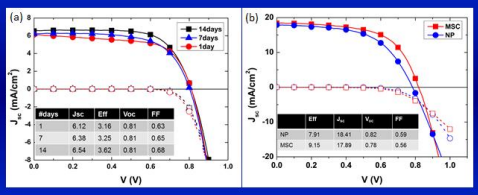

#days	Jsc	Eff	Voc	FF
1	6.12	3.16	0.81	0.63
7	6.38	3.25	0.81	0.65
14	6.54	3.62	0.81	0.68

	Eff	J_{sc}	V_{oc}	FF
NP	7.91	18.41	0.82	0.59
MSC	9.15	17.89	0.78	0.66

Figure 4: Current-Voltage Characteristics of **(a)** A low temperature dye-sensitised solar cell from initial testing to 14 days of aging in ambient conditions, yielding a final power conversion efficiency (PCE) of 3.62%. This improvement in performance has previously been observed in high temperature processed DSSCs **(b)** A low temperature processed perovskite-sensitized solar cell achieving a 9.15% PCE vs. a high temperature processed nanoparticle control device.

Synthesis of Mesoporous Single Crystals of TiO_2

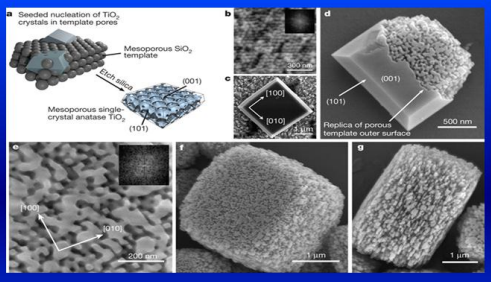

Figure 2: **(a)** Schematic of the synthesis of MSCs. SEM images of **(b)** Pristine silica template, **(c)** Non-porous single crystal, **(d)** Partially porous single crystal, **(e)** Close-up of the pore structure shown in **(d)**, **(e)**&**(f)** Completely porous single crystals.[2]

Density of States, and Transient Photocurrent and Photovoltage Decay

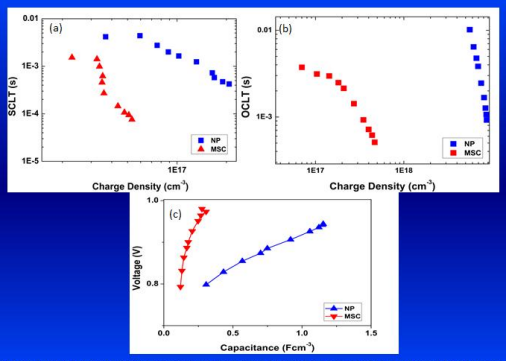

Figure 5: **(a)** Short circuit lifetime (transport lifetime) vs. short circuit charge density for a low temperature processed MSC devices vs. a high temperature nanoparticle control. The MSC device shows an electron transport rate which is 2 orders of magnitude high than the control device. **(b)** Open circuit lifetime (recombination lifetime) vs. open circuit charge density for a low temperature processed MSC devices vs. a nanoparticle control. **(c)** Graph depicting the density of states (DOS) of the MSCs vs. typical nanoparticles. The steeper DOS suggests the presence of fewer sub-band gap states, and this agrees with the faster transport observed in these devices.

Device Architecture

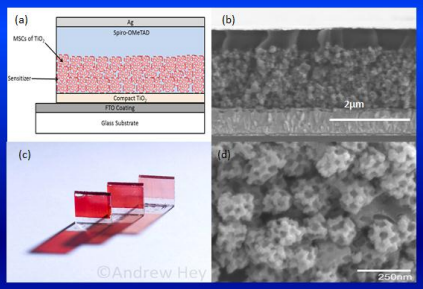

Figure 3: (a)Schematic showing the architecture of a typical solar cell fabricated during this study. (b) Cross-Sectional SEM image of a low temperature processed solar cell, fabricated using MSCs (c) Picture of low temperature processed dye-sensitised solar cells (DSSCs), using MSCs as the photoanode of the device (d) Close up SEM image of 150 nm MSCs

Conclusions

- An all low temperature processed DSSC device has been fabricated using MSCs of TiO_2, resulting in a record breaking 3.62% power conversion efficiency under 1 sun illumination.
- These MSC devices show electron transport which is 2 orders of magnitude faster than in the corresponding high temperature sintered, nanoparticle films
- Using the mixed halide perovskite ($CH_3NH_3PbCl_xI_{3-x}$) as a sensitizer , this low temperature system has achieved a power conversion efficiency of 9.15% under 1 sun illumination.

References

1. Pommer, E.E.; Boercker, J. E.; Aydil, E.S. Appl. Phys. Lett. 2007, 91, 123116
2. Crossland, E. J. W.; Noel, N.; Sivaram, V.; Leijtens, T.; Alexander-Webber, J. A.; Snaith, H. J. *Nature* **2013,** 495, (7440), 215-219

Acknowledgements: This work was funded by the European Community's Seventh Framework Programme (FP7/2007-2013) under grant agreement number 246124 of the SANS project, the European Research Council (HYPER project number 279881 and the Engineering and Physical Sciences Research Council. N.Noel thanks the Government of the Republic of Trinidad and Tobago for financial support.

Figure 1: SSSC 2013 Poster